Lukas Brunnader

Investigation of the Dynamic Behavior of Hydro Generators in Fault Cases,

Focusing the Soleplates and Concrete Reaction Forces

Diploma thesis to gain the Austrian academic degree of a

Diplom – Ingenieur

Graz University of Technology

Faculty of Mechanical Engineering and Economic Science

Adviser: Dipl.-Ing. Dr. techn. Andreas Marn

Institute for Thermal Turbomachinery and Machine Dynamics

Directorate: Univ.-Prof. Dipl.-Ing. Dr. techn. Franz Heitmeir

STATUTORY DECLARATION

I declare that I have authored this thesis independently, that I have not used other than the declared sources / resources, and that I have explicitly marked all material which has been quoted either literally or by content from the used sources.

....

date Lukas Brunnader

Preface

This diploma thesis was made in close collaboration with Andritz Hydro Ltd., Peterborough, Canada. Hereby, I want to thank Andritz Hydro for sponsoring this diploma thesis. A very special thanks goes to my advisor Wayne Martin, who guided and supported me throughout this project with his expertise. Sincere thanks goes also to the whole team of Andritz Hydro, which received me very well and provided professional advice at all times.

For the assistance on the part of Graz University of Technology, Institute for Thermal Turbomachinery and Machine Dynamics, I want to thank Dipl.-Ing. Dr. techn. Andreas Marn for his patient and comprehensive support.

My biggest thanks appertains to my parents, Anton and Elfriede, who established my education and were here to assist me in every possible way all the time, and to my long term girlfriend Katharina, who patiently stood by my side all these years.

Thank you.

Lukas Brunnader

Symbols

Symbol	Unit	Description
F	N	Force
T	Nm	Torque
P	W	Power
R	VA	Rating
η_{PF}	--	Power factor
ω	$\frac{1}{s}$	Angular frequency
$\omega_{0,1,2,...}$	$\frac{1}{s}$	Angular Eigen frequency
Ω	$\frac{1}{s}$	Angular excitation frequency
f	$\frac{1}{s}$	Frequency
$f_{0,1,2,...}$	$\frac{1}{s}$	Eigen frequency
f_G	$\frac{1}{s}$	Grid frequency
n	$\frac{1}{\min}$	Rounds per minute
p	--	Number of poles
t	s	Time
t_{end}	s	Time at the end of a transient calculation
T	s	Periodic time
l	m	Length, distance between objects
h	m	Height
m	kg	Mass
Θ, J	$kg \cdot m^2$	Mass moment of inertia

I_P	m^4	Polar area moment of inertia
$\ddot{x}$	$\frac{m}{s^2}$	Acceleration in x-direction
$\dot{x}$	$\frac{m}{s}$	Velocity in x-direction
x	m	Distance in x-direction
$\ddot{\varphi}$	$\frac{1}{s^2}$	Angular acceleration
$\dot{\varphi}$	$\frac{1}{s}$	Angular velocity
φ	--	Rotation / Angular location
u	m	Displacement
$\bar{u}$	m	Mean displacement
p	$\frac{N}{m^2}$	Pressure
η	--	Reaction force factor
s	m	Distance
d_C	m	Tangential gap between core and key bar
λ	--	Eigen value
b	$\frac{N \cdot s}{m}$	Viscose damping coefficient
D	--	Damping ratio
δ	$\frac{1}{s}$	Decreasing constant
n	--	Amount
n_{SP}	--	Amount of soleplates
n_{SPN}	--	Amount of nodes per soleplate
A	m^2	Area
A_{teeth}	m^2	Teeth cross section area

A_{yoke}	m^2	Yoke cross section area
D / R	m	Outer diameter / radius
d / r	m	Inner diameter / radius
d_{CT} / r_{CT}		Inner core diameter / radius, including radial teeth length
ρ	$\frac{kg}{m^3}$	Density
ρ_{eq}	$\frac{kg}{m^3}$	Equivalent core density
E	$\frac{N}{m^2}$	Young's modulus
G	$\frac{N}{m^2}$	Shear modulus
ν	--	Poison ratio
σ	$\frac{N}{m^2}$	Tensile stress
τ	$\frac{N}{m^2}$	Shear stress
c	$\frac{N}{m}$	Stiffness, spring stiffness
c_φ, c_T	Nm	Torque spring stiffness
R_a	--	Armature resistance
R_f	--	Field resistance
R_{kd}	--	d-axis amortisseur resistance
R_{kq}	--	q-axis amortisseur resistance
X_{ad}	--	d-axis magnetizing reactance
X_{aq}	--	q-axis magnetizing reactance
X_1	--	Armature leakage reactance
X_f	--	Field leakage reactance

X_{kd}	--	d-axis amortisseur leakage reactance
X_{kq}	--	q-axis amortisseur leakage reactance
x_d	--	d-axis synchronous reactance (saturated)
x_q	--	q-axis synchronous reactance
$x_d^{'}$	--	d-axis transient reactance (saturated)
$x_d^{''}$	--	d-axis sub transient reactance (saturated)
$x_{qi}^{''}$	--	q-axis sub transient reactance
x_2	--	Negative sequence reactance
T_a	s	Armature time constant
$T_{d0}^{'}$	s	d-axis open circuit transient time constant
$T_{d0}^{''}$	s	d-axis open circuit sub transient time constant
$T_{q0}^{''}$	s	q-axis open circuit sub transient time constant
$T_d^{'}$	s	d-axis transient time constant
$T_d^{''}$	s	d-axis sub transient time constant
$T_q^{''}$	s	q-axis sub transient time constant
T_{a3}	s	Armature short circuit time constant for 3-phase symmetrical fault
$T_{d(l-l)}^{'}$	s	d-axis transient time constant for line-line fault
$T_{d(l-l)}^{''}$	s	d-axis sub transient time constant for line-line fault
E	--	Rated voltage
T_f	Nm	Faulty torque
$T_{f(3)}$	--	Faulty torque in case of a 3-phase short circuit
$T_{f(l-l)}$	--	Faulty torque in case of a line-to-line short circuit

T_{f_stat}	--	Static component of faulty torque
T_{f_ω}	--	Single frequency component of faulty torque
$T_{f\_2\omega}$	--	Double frequency component of faulty torque
$\underline{\underline{P}}$	--	Point matrix
$\underline{\underline{F}}$	--	Field matrix

Frequently used indices

Index	Description
$-_{x,r}$	Value in radial and / or x-direction
$-_{y,\varphi}$	Value in tangential and / or y-direction
$-_{z}$	Value in axial and / or z-direction
$-_{C}$	Core
$-_{F}$	Frame
$-_{St}$	Stack (Core without air slots)
$-_{i}$	Integer for numbering
$-_{f}$	Condition at a case of failure
$-_{n}$	Nominal, operational value
$-_{pu}$	Per-unit value
$-_{SP}$	Soleplate
$-_{SPN}$	Soleplate node(s)
$-_{m}$	Average / mean value

All other used indices are self-evident or described in the context.

Abstract

This thesis deals with the dynamic behavior of large hydro generators in cases of exposure to transient internal or system fault forces. The focus is on the stator and its soleplates where all the forces are transmitted into the foundation concrete.

A hydro generator is not only designed to withstand just operational forces. It is also designed to withstand forces which might occur in exceptional circumstances. These exceptional circumstances this thesis has a look at are the short circuit of 2 or 3 phases (at the stator outlet) and the faulty synchronization. These occurring faulty forces are acting on the stator core in tangential direction (torque). Furthermore these faulty torques are, in contrast to the operational torque, of dynamic kind (transient). Their peak value is also multiple times higher than the static operational torque.

However, as initially mentioned, the stator has to be designed to withstand these faulty torques as well as the foundation of the powerhouse. Now, currently the stator design is based on a static force value, which is the maximal occurring peak value of the faulty torque. Due to the high stator core mass, the high excitation frequency and the loose tangential core-to-frame connection, it is expected that the force at the soleplate (where the main focus of this thesis is) might be lower than predicted with the static value. If so, stator and especially soleplate dimensions might be reduced. And as concrete forces are lower, a force reduction means also an indirect cost reduction for the customer, who has also to pay the costs for the foundation.

But as this thesis shows, with a traditional stator design this expectation did not occur. A buildup of reaction forces at the soleplates, multiple times above the static value, takes place in most of the cases. So instead of developing an easy-to-handle calculation method the regard the dynamic behavior in the development phase of a generator (which was the original target of this thesis), potential designs for a force reduction at the soleplates are discussed at the end of this thesis.

Table of Contents

1 Introduction into Hydro Power

1.1 Hydro Power Plants

Hydro power plants are used to transfer the energy of water to electric energy. This is done by a blade wheel (hydraulic turbine runner), which is attached by a shaft to the rotor part of the generator. In contrast to so called turbo generators (which are driven by steam) the majority[1] of hydro generators have a vertical shaft. The vertical construction is necessary to avoid needless redirections of water. However, the principal function of an electrical synchronous generator, described in Chapter 1.2.1, is for each design the same. Depending on the environmental conditions, hydro power plants are roughly divided into four main groups:

- Conventional plants
- Pumped-storage plants
- Run-of-the-river plants
- Tide power plants

Conventional plants (Figure 1-1) are understood as plants using the potential energy of water by damming water of a river. Depending on the water level and energy demands more or less generator units are activated by opening the water gates to the hydraulic turbine wheel.

Pumped-storage plants (Figure 1-2 and Figure 1-3) use the height difference of two different located, sometimes artificially built lakes. The benefit of this system is that during times with less energy consumption the energy surplus can be used to pump water to a higher geologic level. During times with a high demand of energy, the water will be discharged again, driving the turbine. Here the benefit is used, that a generator can also act as motor and power the pump, thereby minimizing the amount of base power needed to supply energy to an operating grid.

Run-of-the-river plants are similar to the conventional plants, but the dam might not be as high. As the water is not dammed, the natural river flow is not disturbed much.

Tide power plants use the daily tide of the sea.

[1] An exception builds the so called airbag generator.

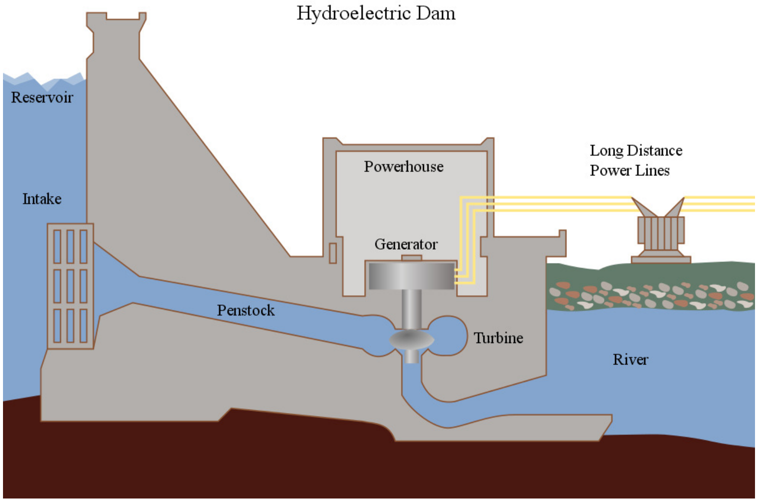

Figure 1-1: Cross section of a conventional power plant

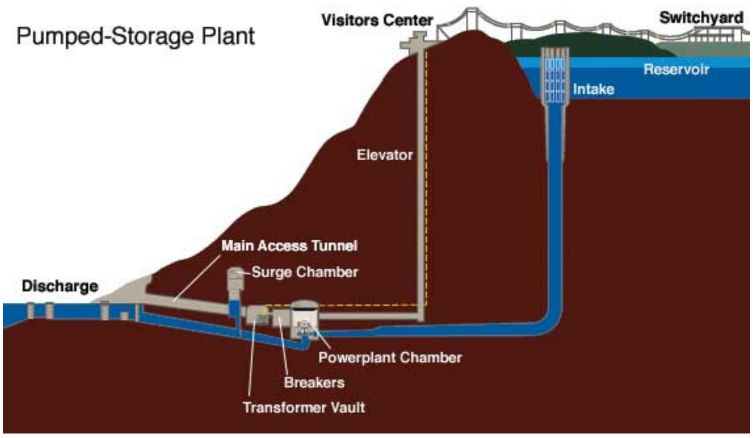

Figure 1-2: Cross section of a pumped-storage plant on Raccoon Mountain, USA

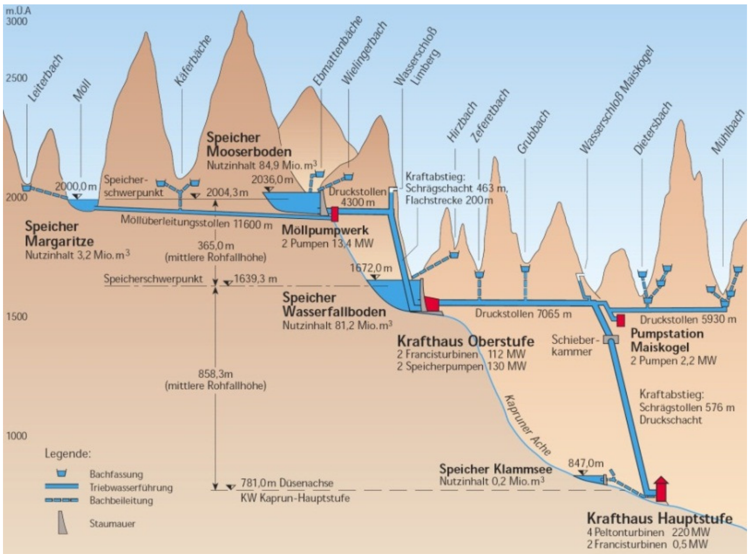

Figure 1-3: Projected view of a cross-linked pumped-storage plant in Kaprun, Austria

The most common generator used in industrial hydro power plants is the synchronous generator. Besides the synchronous generator there is the asynchronous generator – both are alternating-current (AC) generators – and the direct-current (DC) generator.

1.2 The Synchronous Hydro Generator

Some images and contents of this chapter (including subchapters) originate from [1], [2], [3], [4] and [5].

1.2.1 Basic Design and Functionality

Basic functionality

A generator is an electrical machine to transform mechanical to electrical energy. In most cases, mechanical energy sources for prime movers are water, gas or steam. The basic function of the whole generator is for each case the same: A fluid flows through a turbine and causes the turbine to move due to redirection. The turbine, connected to a shaft, sets the rotor in motion. The actual conversion of mechanical into electrical energy is based on the Lorentz force. Is a conductor moved normally in a unidirectional magnetic field, its electric charge is moved in the conductor's direction. The Lorentz force is acting on the conductor as long the conduction is in motion. The charge displacement causes a voltage between the conductor's ends. To increase the voltage several conductors can be connected in series.

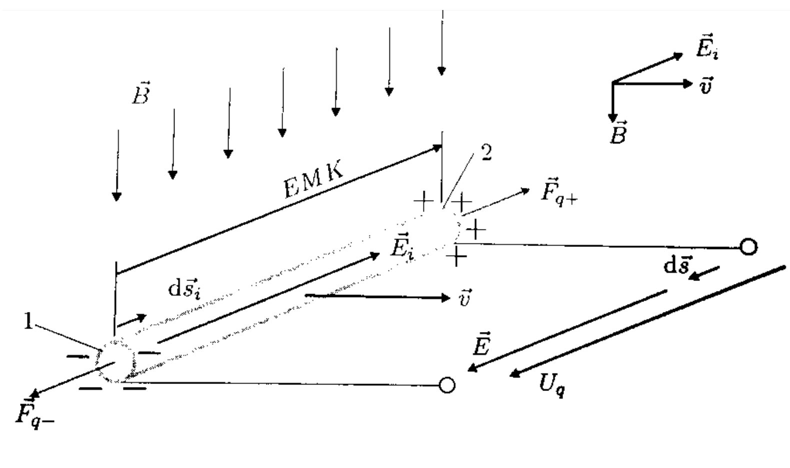

Figure 1-4: Magnetic induction by moving a conductor [3]

In case of most nowadays synchronous generators, the magnetic field is on the rotor part. The magnetic field is generated by a permanent magnet or – more often – by an electro magnet. The induced voltage occurs in the windings of the stator, by the circulating magnetic field on the rotor.

Basic design differences

Hydro generators have an L/D value[2] mostly lower than 1 (or around 1), whereas turbo generators have an L/D value high above 1. The large diameter of hydro generators is needed, as their rotational speed is much lower compared to turbo generators. Both types of generators must reach the same grid frequency, which is not only a function of the diameter, but also of the rotational speed and the amount of pole pairs:

$$n = 60 \cdot \frac{f_G}{\frac{p}{2}} \tag{1.1}$$

So compared to a turbo generator a hydro generator has more poles and also a larger diameter to reach the grid frequency.
However, rotors with a relative small diameter (higher-speed generators with 1200 RPM and more) are designed as so called round rotors. Round rotors have a massive rotor where the pole slots are milled out of a single piece magnetic steel. For large diameter machines the rotor is designed as so called salient pole rotor, where the windings are on pole pieces which are attached onto the rotor body (compare Figure 1-5). A salient pole rotor is not applicable for high speed machines as the stress levels in the rotor become excessive in comparison to available material strengths. In any case, the design of the stator core and the windings is completely independent of the rotor type.

[2] L/D = [Stator core height] / [Inner stator core diameter]

A value, smaller than 1, indicates a small stator height relative to its diameter.

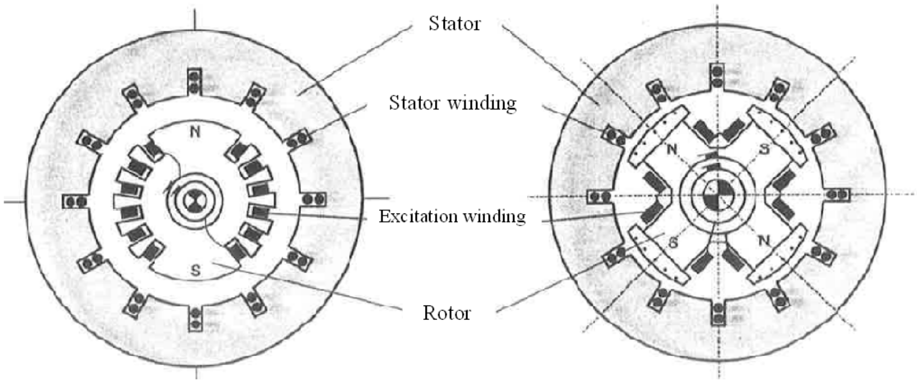

Figure 1-5: Round rotor (left) and salient pole rotor (right) [2]

As already mentioned, a major difference is the shaft axis orientation, whether it's horizontal or vertical. The majority of the fast rotating, steam-driven generators have horizontal shafts; the slower rotating generators, such as hydro generators, have in most cases vertical shafts.

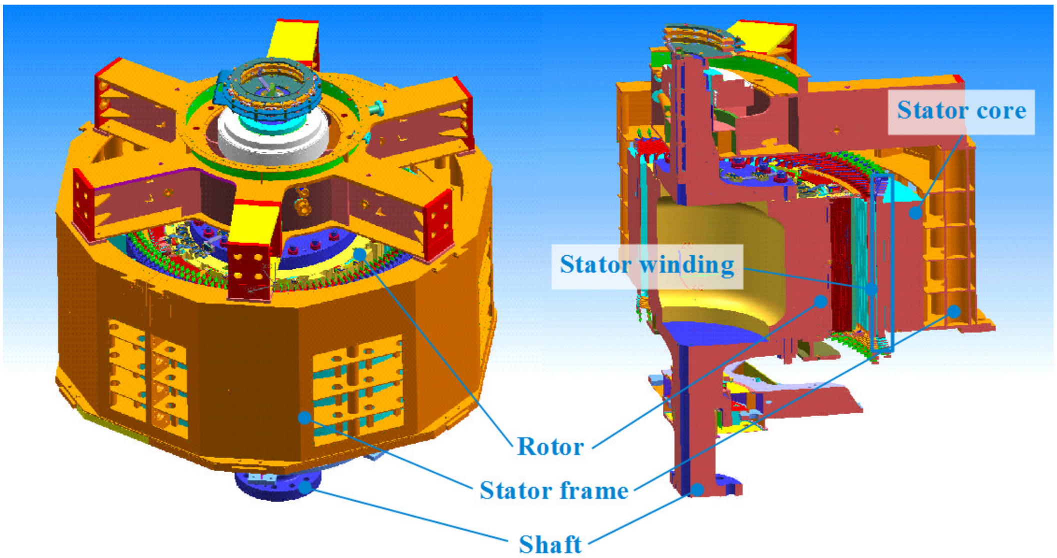

Figure 1-6: CAD model of a hydro generator [4]

Figure 1-6 shows a hydro generator design. The shaft is coupled to the turbine, which sets the rotor in motion. Between the coupling flange and the rotor is the guide bearing located. The orange colored structure is the stator frame. The stator frame supports the stator core (red-brown colored) and the upper bracket with the upper guide and thrust bearing. The stator frame and the stator core are the two main parts of the stator. The main focus in this thesis is on the stator. The rotor part is not relevant for the behavior in a case of failure. Its basic design is superficially described in the subchapter after the next.

Basic stator design

The two parts the stator can be divided into are the **frame** and the **core**. The core is the electrical part of the stator. It is built of thin laminations with slots for the winding coils. As electromagnetic forces are acting on the core, a stable structure – the frame – is required to support it.

As the main focus of this thesis is on the stator, its design is explicitly explained in Chapter 1.2.2.

Basic rotor design

Similar to the stator core, the pole pieces of a salient pole rotor are built up of lamination sheets with appropriate punched shapes for the coils. Coils and poles are usually attached to the rotor body by bolts, dovetail bars or similar mechanisms. The limited load capacity of these attachments is essential for the decision whether a round rotor or a salient pole rotor is used.

For high-speed designs (relatively small diameter) which use a salient pole rotor, the rotor body may be a solid forging with milled profiles for the poles. Low-speed salient pole rotors use spider-and-rim assembly. This spider-and-rim construction may be an integral weldment or casting. But for generators with a large diameter the rim is in most cases separated from the spider.

Round rotors have their winding slots directly milled into the massive rotor (left image of Figure 1-5). This is why the actual rotor shaft acts section wise as pole. The axial going windings are secured by wedges and rings at the coil ends.

Rotors are designed for operation at over speed, which is for hydro generators can be as high as 3 times rated speed depending on the type and design of the hydraulic turbine and water passage. Steam or gas driven generators' over speed rate is 20% above rated speed.

A salient pole rotor with a rim-and-spider design can be seen in Figure 1-14 of the next chapter.

1.2.2 Design Details of the Stator

As already explained, the stator consists of two parts: the core (for the electrical task) and the frame (to support the core). The connection between core and frame is explained in a separate subchapter.

The stator core

The core is built of thin laminations (thickness of 0.35 mm or 0.5 mm) of electrical steel (ASTM A677[3]), which are stacked together to the full core height. Each sheet is applied with a thin film (approx. 0.05 mm) of an insulating varnish. This is done to eliminate the electrical shorting of laminations and reduce the losses resulted by flux.

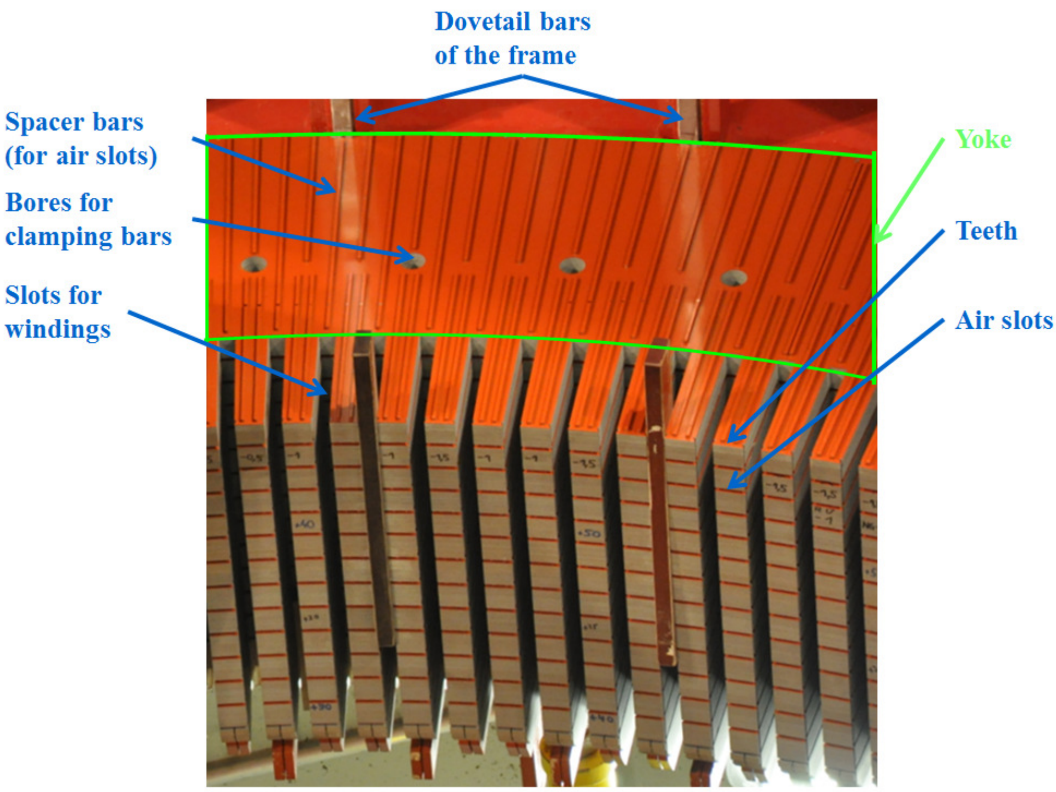

Figure 1-7: Photo of a stacked stator core [4]

Figure 1-7 shows a half-finished stacked core (without the winding coils). On the radial inner end of the core there are the so called teeth. The back end is called yoke. Every certain amount of laminations, a special red colored lamination is used. These red colored laminations have spacer bars applied, which cause ventilation ducts ("air slots" in Figure 1-7). To prevent vibrations and sliding of single lamination sheets, the completely stacked core is clamped at the end. This is done by bars ("clamping bars"), running through all laminations. At each end of these clamping bars an additional plate is applied and the core is clamped by screw nuts (see also sketch in Figure 1-9). In the slots between the teeth the

[3] DIN EN 10106

winding coils are fitted. Figure 1-8 shows exemplarily such a winding coil with a multitude of copper bars in the center, surrounded by plastic insulation.

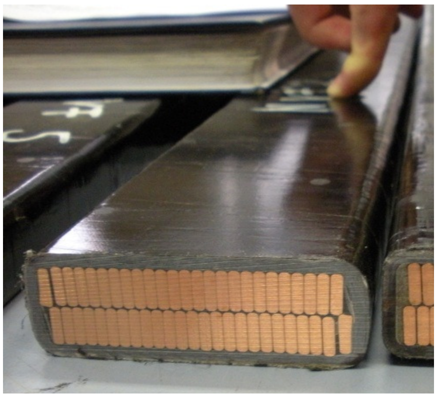

Figure 1-8: Photo of a turbo generator's winding coil [5]

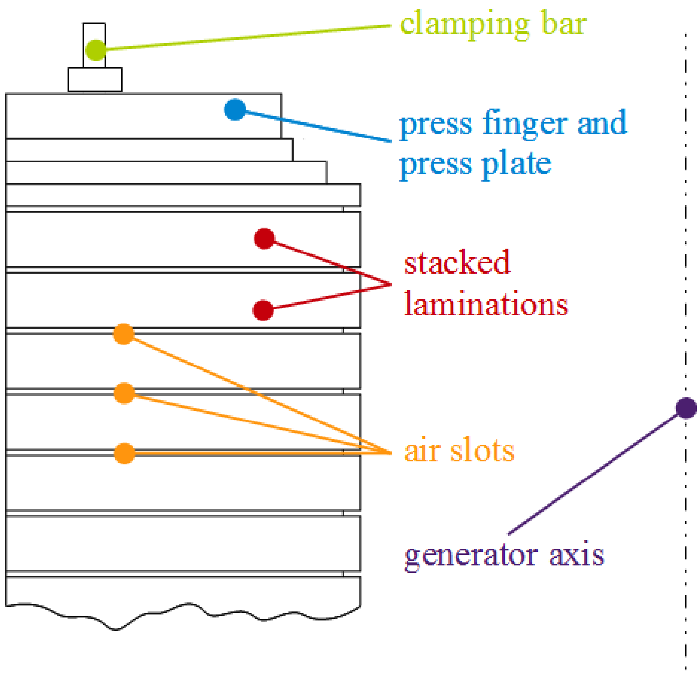

Figure 1-9: Side view of the lamination stack (stator core)

A sketch of one single lamination sheet is shown in Figure 1-10. On the radial outer end the dovetail bar slots (to connect each lamination to the frame) can be seen. The rhomboid shape of the slots for the dovetail bars has assembly reasons. This shape makes it possible to bend the sheet and attached it frontally to the dove tail bar. This is more time saving than threading the sheet from the very top end of the dove tail bar to the bottom. If a temperature monitoring system is desired by the customer, some lamination sheets have slots on their outer radius to attach temperature sensors measuring the core temperature.

On the radial inner end of each tooth it can be seen that all winding slots end up in a negative dovetail shape. In this dovetail shape a wedge is inserted to avoid the winding coils of coming out due to the electromagnetic forces. The bigger the axial core height is, the more susceptible the coils are to move. Very small machines may not need any coil support at all; the friction force after fitting the coils into the slot should withstand the forces, even in a case of failure.

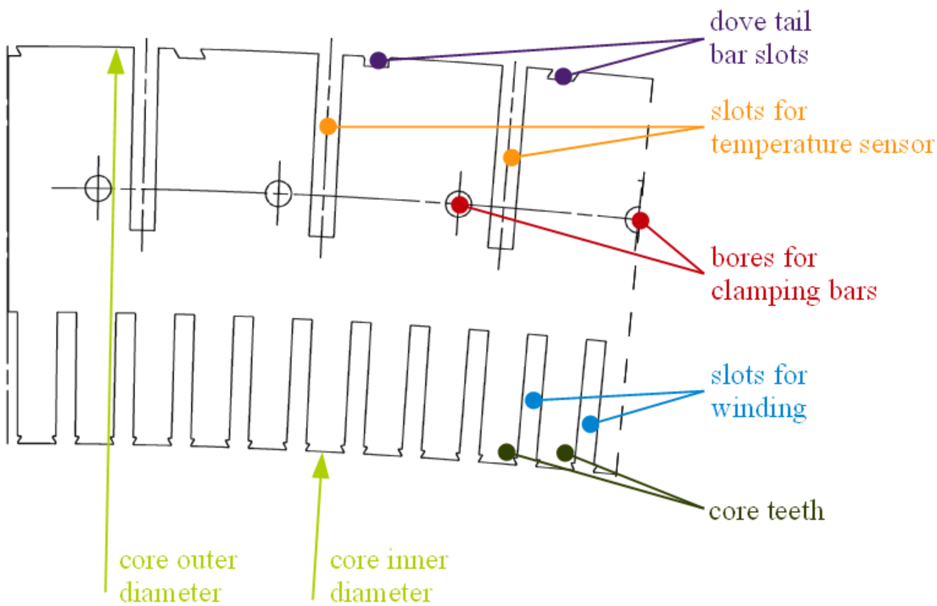

Figure 1-10: Top view of one single lamination sheet

Figure 1-11 is a photo of a few single lamination sheets with spacer bars. Furthermore the bores for the clamping bars and the dovetail shape on the end of each tooth is very well visible. This specific lamination sheet on the photo does not have slots for temperature sensors.

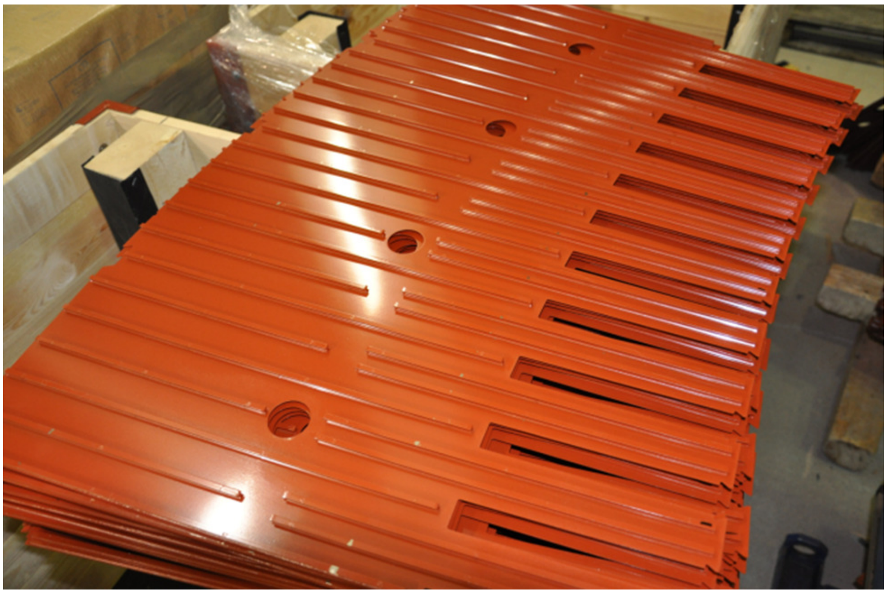

Figure 1-11: Photo of a few single lamination sheets with spacer bars [4]

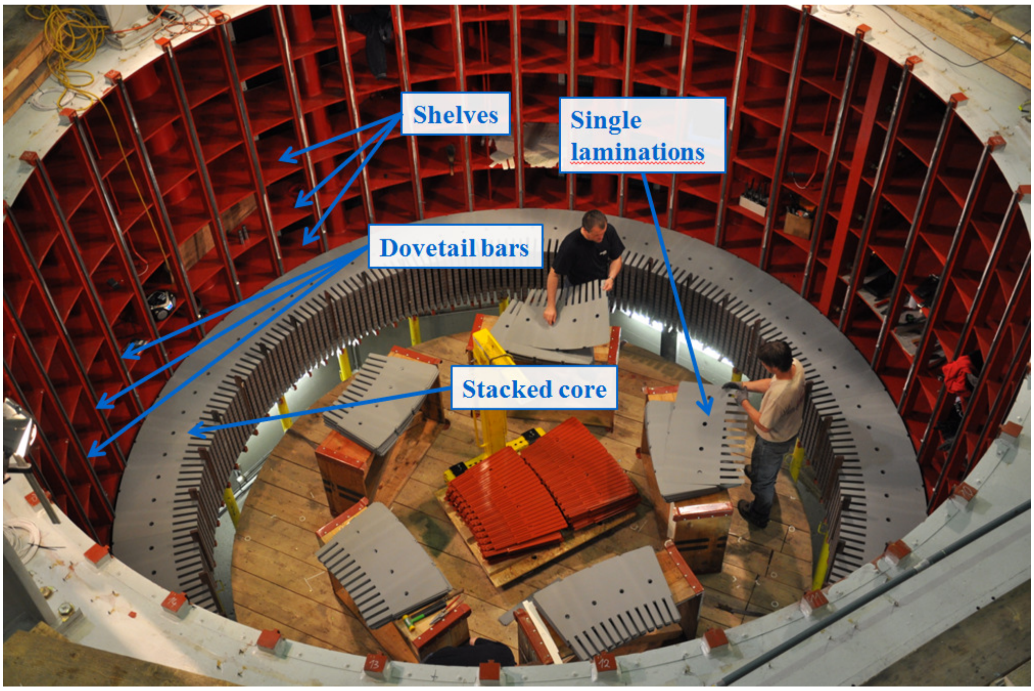

Figure 1-12: Photo of stacking the stator core [4]

Figure 1-12 shows two workers stacking the core on site. The red colored laminations in the center are laminations with spacer bars on the top to realize the ventilation ducts (see also Figure 1-7). They are stacked after every certain amount of usual, gray laminations. The gray laminations are regular laminations with the same shape but without these spacers. They are stacked in between the red colored laminations. When stacking the core, the single lamination segments are stacked interleaved, not to have an axially continues joint on the side edge of each lamination sheet. (Similar to the displaced arrangement of bricks, when building a house.) This would have negative effects on the mechanical stability of the core.

The core-to-frame connection

As roughly visible in Figure 1-12, the stator core is connected to the frame by dovetail bars. These dovetail bars connect the core in radial and tangential direction to the frame. Due to the high mass and the non-existence of high axial forces it is not necessary to fix the frame axially. It is just set onto a plate near the foundation.
However, before the generator reaches its operation temperature there is a tiny radial clearance between the stator core and the dovetail bar. This allows the core to expand radially unopposed a little, before it is pressing against the frame. A reduction of the buckling stress of the core is the result.

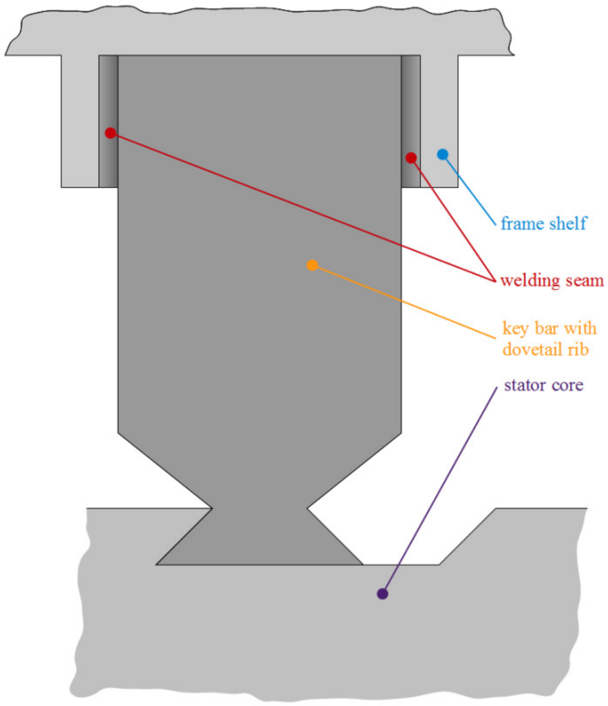

Figure 1-13: Key bar welded to the shelf

For all calculations (except those in Chapter 6.7) in this thesis the situation of the warm condition is assumed, what this means is that the core is radially, tangentially and axially rigidly connected to the frame.
The dovetail bars can be seen in Figure 1-12 very well.

The stator frame

The frame is the structure surrounding the core to support it and to guide the forces into the concrete. In some cases of vertical shaft generators, the thrust bearing, which supports the rotor, is attached (over a bracket) to the top of the stator (like in Figure 1-6). This means on the one hand that the radial bearing stiffness depends on the stiffness of the stator and on the other hand that the stator has to carry the rotor mass and hydraulic load. Additionally the frame must have appropriate openings for the power outlets and ventilation devices (Figure 1-6: big rectangular openings in the frame), what has a negative effect on its structural stiffness.

The stator frame’s basic structure is built of a certain amount of axially arrayed annuluses, called shelves (see Figure 1-12). Their offset or axial spacing among each other is, depending on the machine requirements, approximately 0.5 m. On their radial inside they have pairs of welding strips where the key bar is applied (Figure 1-13). On their radial outside they are encased by the wrapper ((5) in Figure 1-16). The wrapper has a cylindrical shape with a usual sheet thickness of 20 mm. The shelves are welded to the wrapper. In axial direction the shelves are supported by a diamond shaped plate construct, to guide the weight of the core directly to the ground ((4) in Figure 1-16).

If the shaft has a bearing (thrust and/or guide bearing) on it upper end, the bracket (which is the mechanical structure where the bearing is mounted) is connected to the stator frame and/or to a concrete wall. In case there is no wall support, a high axial load capacity and a high lateral stiffness of the stator frame is required. Also therefore the diamond shaped plate structures mentioned before help to increase the lateral stiffness and axial payload.

Most frames of hydro generators must be divided in their circumference direction, when their diameter exceeds transport limitations. To still achieve a uniform stiffness along the whole outline, the joint is tightly screwed together at its flanges at the construction site.

On the frame’s bottom shelf are the soleplates attached, which connect the stator with the concrete. The soleplates are radially guided, which allows the stator to expand while it reaches its operational temperature. This way stress in the core and frame is reduced.

Illustrative generator drawings

Figure 1-14 shows the machine “Grand Coulee”, installed at the Columbia River in Washington, USA. Built in 1974, it is still on the upper end of hydro generators, regarding its power output (700.05 MW per unit). The rotor is a salient-pole rotor with a rim-and-spider design (1). The poles are at (2). The frame (3) is supporting the core and has openings for the power outlets and the cooler (4). The key bars for the core-to-frame connection are not shown in this image. The upper thrust and guide bearing (5) for the shaft (6) is located below the actual generator. It is supported by the bracket (7). A further guide bearing is located closer to the turbine.

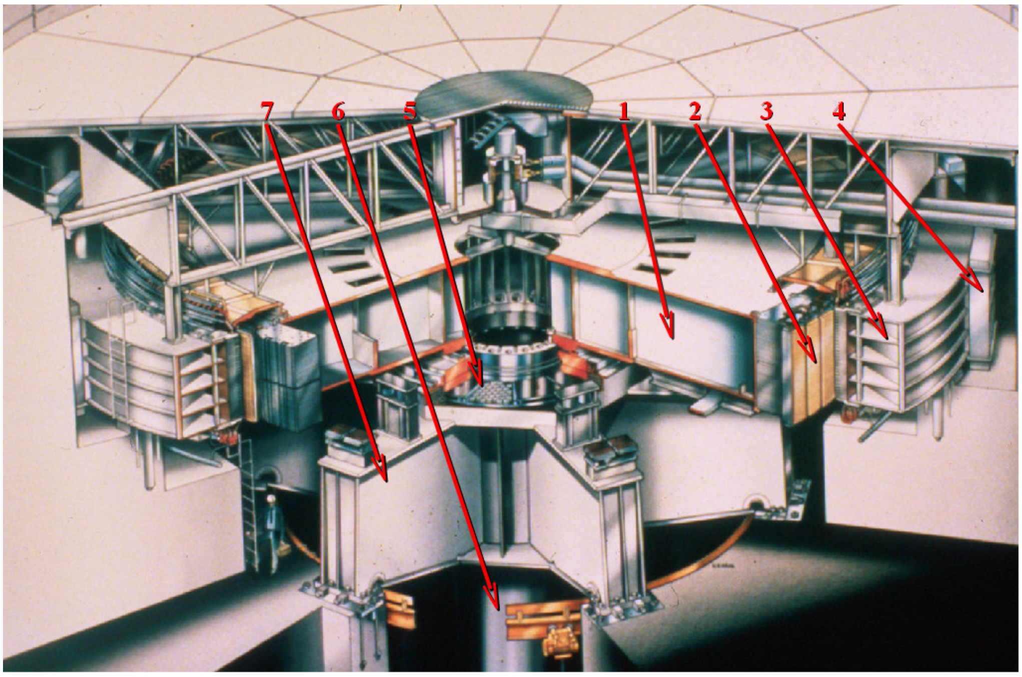

Figure 1-14: Drawing of "Grand Coulee" (84 poles, 718MVA, 85.7 RPM)

Figure 1-15 shows a sectional drawing of a generator with a salient pole rotor (rim-and-spider design) (1) with its poles (2) and the stator (3).

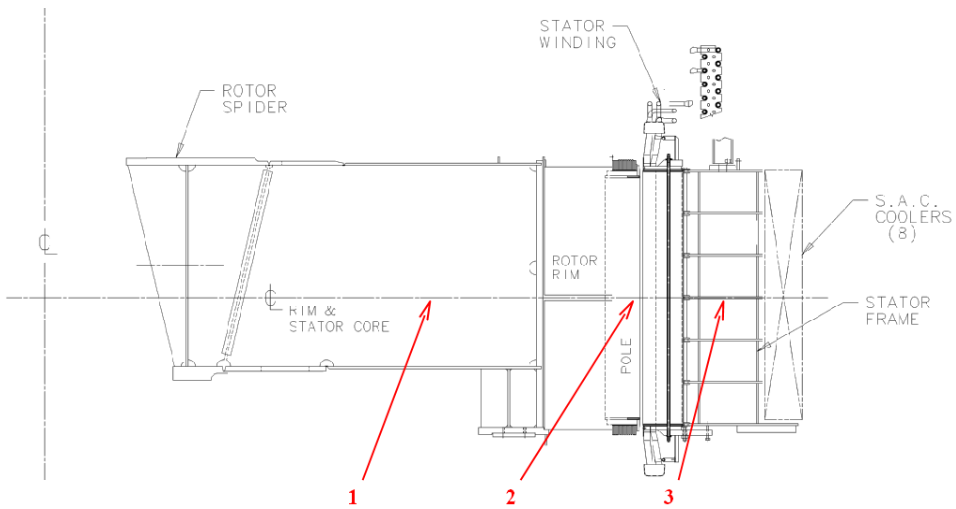

Figure 1-15: 2-D outline drawing of a generator

Figure 1-16 shows a detailed section of the stator of “Grand Coulee”. The end windings (1) can be seen on the top and bottom end of the stator core (2). The stator frame is built up from 5 shelves (3), axial support plates aligned in a diamond shape (4) and the wrapper (5). On the bottom shelf the soleplate with the anchoring (6) is attached. (Previously mentioned numbers are also valid for Figure 1-17). Figure 1-17 is a detailed section of Figure 1-15 which shows the clamping bar (8) with the press fingers and press plates (9). The slot (7) in the stator core for the winding coils is also shown in this 2-D outline drawing.

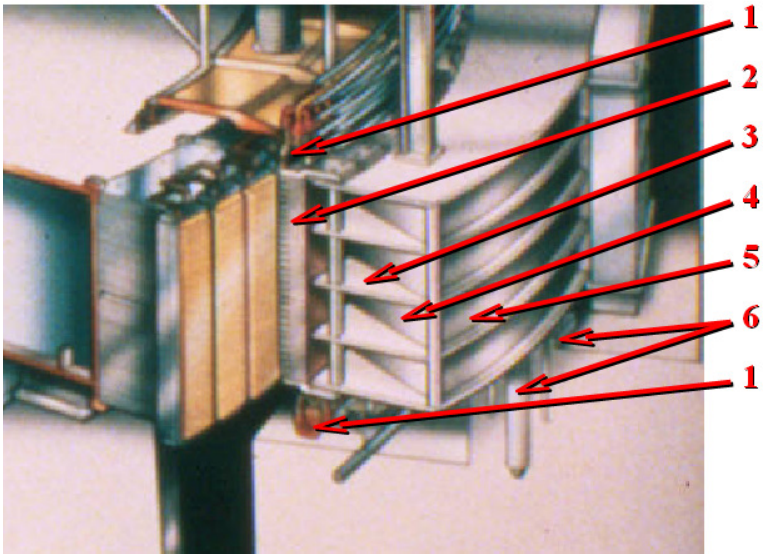

Figure 1-16: Drawing of “Grand Coulee”, detailed section

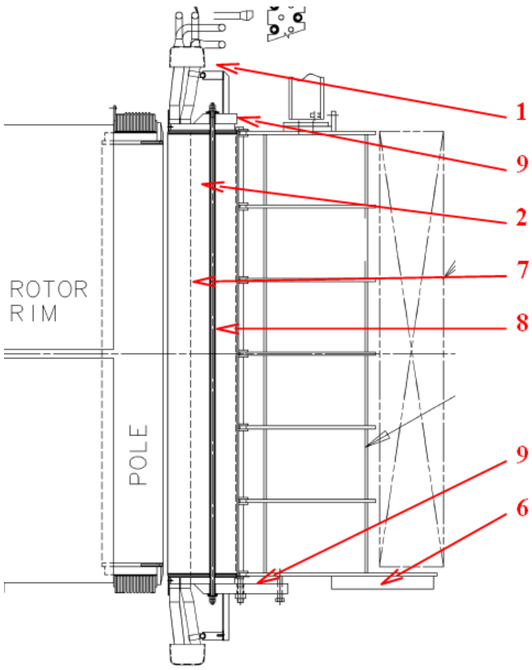

Figure 1-17: 2-D outline drawing of a generator, detailed view on stator

1.2.3 Electromagnetic Forces and Faulty Torques

During usual operation, electromagnetic forces act on the stator in radial and tangential direction. Whereas the radial forces are harmonic, which depend on the electromagnetic properties, the rotational speed and the number of poles, the tangential force (torque) is constant. It only becomes dynamic in case of an electrical failure, like it is discussed in this thesis. Anyway, the nominal torque during usual operation just depends on the rated rotational speed and the power output of the machine:

$$T = \frac{R}{\omega} \cdot \eta_{PF} = \frac{P}{\omega} \qquad (1.2)$$

The cases of failure looked at in this thesis are the electrical short circuit and the faulty synchronization. As mentioned, if one of these failures occurs, the usual constant torque ($T = P/\omega = const.$) suddenly becomes dynamic ($T = f(t)$).

Forces at a short circuit

In the case of an electrical fault, the torque, acting on the stator, becomes dynamic and increases its peak value to a value multiple times higher than the nominal torque. This all happens within a fraction of a second.

Most electrical faults occurring in power plants, at transformer stations and during transmission are asymmetric. This means that all 3 phases are effected differently. This may be

- a line-to-line short circuit (also known as 2-phase / 3-phase short circuit), where a short circuit between 2 or 3 phases occur,
- a line-to-ground short circuit, where one line becomes grounded, and
- a double line-to-ground, where 2 lines get in contact with the ground and consequently with each other.

These failures can occur during lightning, storm damage or due to a broken insulation.

The torque, acting on the stator in case of these failures, can be calculated with the basic electrical parameters of the equivalent circuit of the generator. The appropriate equations [6] are quoted in the next subchapters. They are simplified and therefore just valid if there is no load at the time of the short circuit. The required parameters can be retrieved from the equivalent circuit of the synchronous generator. (In transient analysis for electrical faults, the traditional 3-phase circuit model of a generator is usually converted to the d- and q-axis equivalent circuit model, in order to simplify the mathematical formulations. Their equivalent circuits are shown in Figure 1-18.)

Note: All parameters in the following equations, except the time constants, are per-unit values. This means that they are referred to a certain base value. In general the base value of each resistance or reactance (except r_f, x_f, x_{kd} and x_{kq}) is $R_{sb} = X_{sb} = U_a/I_a$, in which U_a is the rated L-N voltage and I_a the rated line current. The definitions of the rotor resistance and reactance base values R_{rb} and X_{rb} (which are the base values for r_f, x_f, x_{kd} and x_{kq}) involve some mathematical conversions between the rotor and the stator base values. Including these conversions would exceed the introduction chapter of this thesis.

However, also the results of following equations ($T_{f(3)}$ and $T_{f(l-l)}$) are per-unit values. They are referred to the nominal torque Tn.

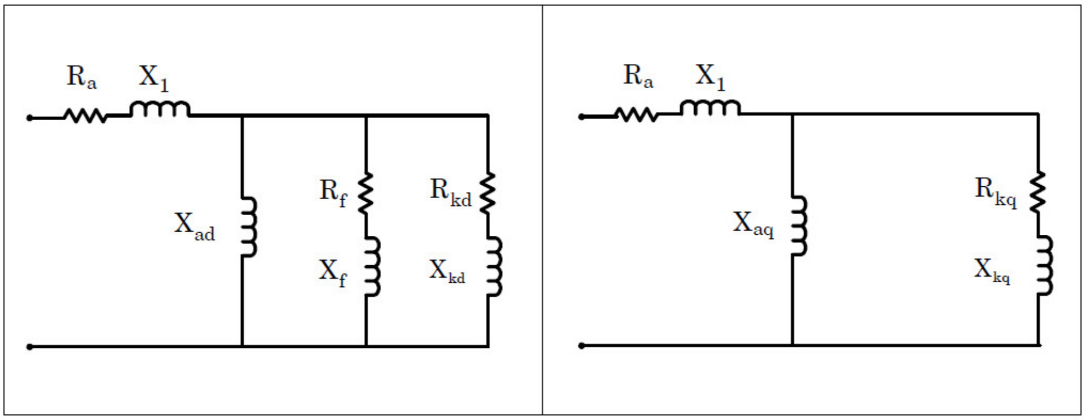

Figure 1-18: Equivalent circuit of d-axis (left) and q-axis (right)

R_a .... Amature resistance [--]
R_f .... Field resistance [--]
R_{kd} .... d-axis amortisseur resistance [--]
R_{kq} .... q-axis amortisseur resistance [--]
X_{ad} .... d-axis magnetizing reactance [--]
X_{aq} .... q-axis magnetizing reactance [--]
X_1 .... Armature leakage reactance [--]
X_f .... Field leakage reactance [--]
X_{kd} .... d-axis amortisseur leakage reactance [--]
X_{kq} .... q-axis amortisseur leakage reactance [--]

3-phase short circuit faulty torque equation

$$T_{f(3)} = E^2 \cdot \left[\frac{1}{2} \cdot \left(\frac{r_d}{x''^2_d} + \frac{r_q}{x''^2_q} \right) \cdot e^{-\frac{2t}{T_{a3}}} + \frac{F_1{}^2 \cdot r_a}{x''_d{}^2} + \frac{F_1}{x''_d} e^{-\frac{t}{T_a}} \sin(\omega t) + \frac{1}{2} \cdot \left(\frac{1}{x''_q} - \frac{1}{x''_d} \right) \cdot e^{-\frac{2t}{T_a}} \sin(2\omega t) \right] \quad (1.3)$$

where

$$F_1 = \left(1 - \frac{x''_d}{x'_d} \right) \cdot e^{-t/T''_d} + \left(\frac{x''_d}{x'_d} - \frac{x''_d}{x_d} \right) \cdot e^{-\frac{t}{T'_d}} + \frac{x''_d}{x_d}$$

and

$$r_d = \frac{(x_d - x'_d) \cdot T'_{d0pu}}{1 + T'^2_{d0pu}}$$

and

$$r_q = \frac{(x_q - x''_q) T''_{q0pu}}{1 + T''^2_{q0pu}}$$

and

$$T_{a3} = \frac{2 \cdot x_2}{x''_d + x''_q}$$

(For symbol declaration see next chapter.)

Line-to-line short circuit faulty torque equation

$$T_{f(l-l)} = \frac{2E^2}{x''_d + x_2} \left[\begin{array}{l} F_2 \cdot e^{-\frac{t}{T_a}} \sin\theta_0 \cdot \left(-\cos(\theta) + 3b \cdot \cos(3\theta) - 5b^2 \cdot \cos(5\theta) + \cdots \right) + \\ + \left(F_2^2 \frac{x_2}{x''_d + x_2} - \frac{x''_d - x_2}{x_2} e^{-2t/T_a} \sin^2\theta_0 \right) \cdot \left(\sin(2\theta) - 2b \cdot \sin(4\theta) + \cdots \right) \end{array} \right] \quad (1.4)$$

with

$$F_2 = \left(1 - \frac{x_d'' + x_2}{x_d' + x_2}\right) \cdot e^{-\frac{t}{T_{d(l-l)}''}} + \left(\frac{x_d'' + x_2}{x_d' + x_2} - \frac{x_d'' + x_2}{x_d + x_2}\right) \cdot e^{-\frac{t}{T_{d(l-l)}'}} + \frac{x_d'' + x_2}{x_d + x_2}$$

$$\theta = \omega \cdot t$$

$$b = \frac{x_2 - x_d''}{x_2 + x_d''}$$

$$T_{d(l-l)}'' = T_{d0}'' \frac{x_d'' + x_2}{x_d' + x_2}$$

$$T_{d(l-l)}' = T_{d0}' \frac{x_d' + x_2}{x_d + x_2}$$

x_d	d-axis synchronous reactance (saturated) [--]
x_q	q-axis synchronous reactance [--]
SCR	Short circuit ratio [--]
x_d’	d-axis transient reactance (saturated) [--]
x_d”	d-axis subtransient reactance (saturated) [--]
xqi”	q-axis subtransient reactance [--]
x_2	Negative sequence reactance [--]
T_a	Armature time constant [s]
T_{d0}’	d-axis open-circuit transient time constant [s]
T_{d0}”	d-axis open-circuit subtransient time constant [s]
T_{q0}”	q-axis open-circuit subtransient time constant [s]
T_d’	d-axis transient time constant [s]
T_d”	d-axis subtransient time constant [s]
T_q”	q-axis subtransient time constant [s]
T_{a3}	Armature short circuit time constant for 3-phase symmetrical fault [s]
$T_{d(l-l)}$’	d-axis transient time constant for line-line fault [s]
$T_{d(l-l)}$”	d-axis subtransient time constant for line-line fault [s]
E	Rated voltage [--]

The highest amplitude occurs at $\theta_0 = 90°$.

Forces at a fault synchronization

Once the synchronous generator reaches its operation speed frequency (Equation 1.1) it must be verified that all phases of the generator output are also in phase with the phases of the grid. Even though nowadays this process is done completely automated, fault synchronizations can occur. The equation [7] for the 3-phase fault synchronization shown below is valid for only the first two or three cycles, as the decay value is not regarded.

$$T = \frac{E^2 * \sin(\delta)}{\left(X_d'' + X_S\right)} * \left[1 - \cos(\omega t) + \tan\left(\frac{\delta}{2}\right) * \sin(\omega t)\right] \tag{1.5}$$

The final equations of the faulty torque look all very similar, independent of the actual case of failure (whether it’s a 2- or 3-phase short circuit or a faulty synchronization). They all have a static component, a single-frequency component and a double-frequency component. (The terms “single-frequency” and “double-frequency” are based on the grid frequency of the country the generator is installed. If the grid frequency is 60 Hz, the term “single-frequency” is appropriate to 60 Hz and “double-frequency” to 120 Hz.) Moreover they all decrease exponentially with a relative high, almost negligible, time constant, considering that all these transient fault torque forces just occur for two or three cycles (until safety devices power-down the generator, which happens after less than 0.05 s). The only differences are the values of the excitation amplitude and declination factor of each failure torque. This is the reason why all failure calculations in this thesis are based on the equations of the 3-phase short circuit. The dynamic response of the stator is expected to be very similar for all different cases of failure – just the amplitude would change linear.

Figure 1-19 shows plots, generated by a software used by Andritz Hyrdo Weiz. These dynamic torque forces are transient, composed of a static force, a single-frequency force and a double-frequency force, decreasing exponentially with different time constants. It can be seen that the single-frequency is dominating.

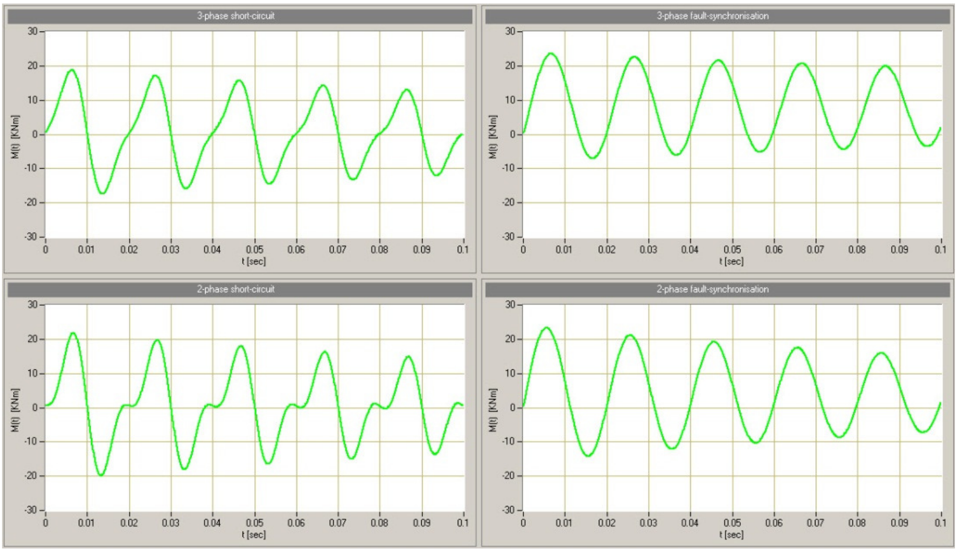

Figure 1-19: Example plots of four types of failures

Note: There is **no run up** to the faulty torque's frequency. If an electrical failure occurs, the faulty torque acts immediately on the stator with the single- / double-frequency.

1.3 Job definition

A hydro generator is – like every other machine – not only designed to withstand just operational forces. It is also designed to withstand forces which might occur in exceptional circumstances. For a hydro generator, these exceptional forces, which are of electromagnetic kind, are multiple times higher (up to ten times and even higher) than the operational forces. Not only the generator, but also the foundation of the powerhouse has to be designed to withstand these forces, what increases the costs for the customer significantly.

So far, the generator's design to withstand these forces is based on simple static correlations, which doesn't regard dynamic interactions. This diploma thesis analyses the dynamic behavior of the stator in case of exposure to electrical faults. The main focus is on the occurring reaction forces at the soleplates, where the stator is attached to the powerhouse.

These exceptional forces, mentioned before, are caused by a short circuit in the area of powerhouse or a faulty synchronization to the grid. The result is a dynamic torque force acting on the stator, which amplitude is multiple times higher than the static nominal torque under usual operation.

In case of such a suddenly occurring failure, emergency controls (i.e. circuit breaker) shut down the excitation device within a very few excitation cycles (after approximately 0.05 s) to avoid high forces acting on the stator for a long time. Before shutdown, the excitation force is also declining exponentially. These and some other facts (like the high mass of the stator, the relative high excitation frequency and a low stiffness connection between the stator core and the stator frame) allow the assumption that the reaction force, which is occurring at the soleplates / concrete in a case of failure, might be much lower than currently calculated. If these reaction forces are really lower than currently calculated, the costs of producing the generator and building the powerhouse can be minimized and the competitiveness of Andritz Hydro could increase.

A hydro generator is not a mass product. Each hydro power plant has its own hydro generators, designed just for this specific plant. Even though their basic design is the same, they differ vastly in dimensions and design details, which results in a unique dynamic behavior for each machine. This thesis takes a look at ten different projects of Andritz Hydro. The projects are chosen in a way that a lot of power, speed and dimension ranges are covered.

The first step in this thesis is to find out the basic dynamic behavior of the stator and its parts. Natural frequencies are analyzed and compared and similarities between the ten reference projects (regarding their dimensions, power output etc.) are tried to be found. After these calculations it should already be possible to make a prediction if a natural force reduction (hypercritical operation) does occur.

More detailed results concerning the dynamic behavior should be achieved in the next step, by applying the transient faulty torque onto the stator and evaluating the reaction forces.

A very unpredictable part of the generator is the core-to-frame connection with its tangential clearance at the dovetail bar. The influence of this clearance in a fault case should be analyzed in the next step.

Finally, if a natural force reduction is against initial expectations not occurring, possible ways of spring supports should be studied superficially.

Most calculations are done by using the finite element method software ANSYS Classic in version 13. Simplified models of the reference machines are used for the calculations. These models are built and all FE calculations are done by using the APDL (ANSYS Parametric Design Language).

Note: Unfortunately there is no data available of how often one of these faults occur. Neither is measuring data available of how the stator reacts in tangential direction in a case of applied faults, which makes it not possible to optimize models and compare results with the real behavior.

2 Theoretical Basics

2.1 Coordinate System Declaration

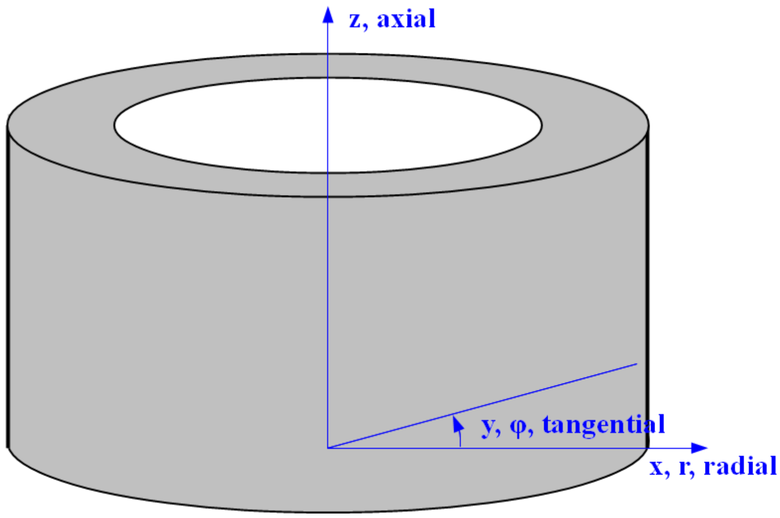

Figure 2-20: Cylindrical coordinate system, illustrated by the help of a stator shape

The majority of descriptions and calculations in this thesis are based on a cylindrical coordinate system. The different symbols used for each component is shown in Figure 2-20. The gray cylinder illustrates the stator. ANSYS still uses the letters x, y and z when working in the cylindrical coordinate system. For description issues, the letters r and φ are mostly used for the radial and tangential component in this thesis.
Unlike during the design process of a generator, the axial origin of the coordinate system in this thesis is at the level of the very bottom shelf. $\varphi=0$ at the center of any soleplate (axial symmetry is postulated for all calculation models). The radial origin is in the center of the circular shaped stator.

2.2 Principles of oscillations

Some contents of this chapter (including subchapters) originate from [8], [9] and [10].

For dynamic machineries the analysis of the dynamic behavior is inevitable for the mechanical structure design. In contrast to reaction forces caused by static loads, reaction forces caused by dynamic loads can increase to a multiple value of the peak excitation value. The dynamic analysis is essential to avoid these effects, or to design a mechanical structure which is strong enough to carry dynamic forces. But not only reaction forces and stress are the reason for including dynamic effects. Nowadays also noise emissions play an important role, which are often caused or increased by dynamic resonance effects.

To understand the mathematics behind vibrations, the next few subchapters will show mathematical basics and physical relationships by hand of mass-spring-damper models with one degree of freedom.

2.2.1 Free Oscillation without Damping

The simplest model to describe a vibration is single mass oscillator with one degree of freedom and no external forces.

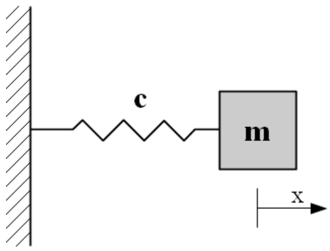

Figure 2-21: A single mass oscillator at its point of equilibrium

Its behavior is described by the ordinary 2nd order differential equation:

$$m \cdot \ddot{x} + c \cdot x = 0 \tag{2.6}$$

With

$$\omega_0^{\ 2} = \frac{c}{m} \tag{2.7}$$

follows:

$$\ddot{x} + \omega_0^{\ 2} \cdot x = 0$$

By using the exponential approach and its appropriate deviations

$$
\begin{aligned}
x &= C \cdot e^{\lambda \cdot t} \\
\dot{x} &= C \cdot \lambda \cdot e^{\lambda \cdot t} \\
\ddot{x} &= C \cdot \lambda^2 \cdot e^{\lambda \cdot t}
\end{aligned}
\tag{2.8}
$$

the equation can be solved:

$$
\begin{aligned}
&\left(\lambda^2 + \omega_0{}^2\right) \cdot C \cdot e^{\lambda \cdot t} = 0 \\
&\left(\lambda^2 + \omega_0{}^2\right) = 0 \\
&\lambda_{1,2} = \pm i \cdot \omega_0
\end{aligned}
$$

The Eigen values in this case are just imaginary.
Inserting the Eigen values into the exponential approach delivers:

$$
\begin{aligned}
x_1 &= C_1 \cdot e^{i \cdot \omega_0 \cdot t} \\
x_2 &= C_2 \cdot e^{-i \cdot \omega_0 \cdot t} \\
x(t) &= C_1 \cdot e^{i \cdot \omega_0 \cdot t} + C_2 \cdot e^{-i \cdot \omega_0 \cdot t}
\end{aligned}
$$

Using the Euler equation $e^{\pm i \cdot x} = \cos(x) \pm i \cdot \sin(x)$ and with $A = C_1 + C_2$ and $B = C_1 - C_2$ the solution is:

$$
x(t) = A \cdot \cos(\omega_0 t) + i \cdot B \cdot \sin(\omega_0 t) \tag{2.9}
$$

An initial displacement of $x(t = 0) = x_0$ leads to the final vibration equation of a free one mass oscillator with one degree of freedom:

$$
x(t) = x_0 \cdot \cos(\omega_0 t) = x_0 \cdot \cos\left(\sqrt{\frac{c}{m}} \cdot t\right) \tag{2.10}
$$

Velocities and accelerations are appropriate derivations of this equation; the term $\sqrt{c/m}$ is the oscillator's natural frequency ω_0.

2.2.2 Free Oscillation with Damping

Depending on the type of dynamic problem, there are several mathematical formulations available to describe damping:

- Coulomb friction damping
- Viscose damping
- Complex damping
- Frequency-independent damping
- Hysteresis damping

The most commonly used formulation is the viscose damping, which is proportional to the velocity $\dot{x}$. It is only valid for harmonic excitation, but delivers also for complex excitations acceptable results. The advantage of the viscose damping is the linearity, which establishes to calculate systems by super positioning results. The so called viscose damping coefficient is the most common number to quantify this damping.

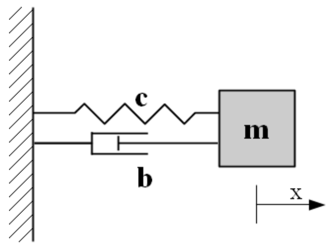

Figure 2-22: A damped single mass oscillator at its point of equilibrium

Including damping behavior (i.e. material damping), the 2nd order differential equation of a single freedom oscillator looks like:

$$m \cdot \ddot{x} + b \cdot \dot{x} + c \cdot x = 0$$

$$\ddot{x} + \frac{b}{m} \cdot \dot{x} + \frac{c}{m} \cdot x = 0 \tag{2.11}$$

b ($[b] = N \cdot s/m$) is the viscose damping coefficient and can only be determined with a further scalar parameter, as the next equation shows:

$$b = 2 \cdot D \cdot \sqrt{m \cdot c} \tag{2.12}$$

D is the dimensionless damping ratio.

Using the definition of the natural frequency (Equation 2.7) and the decreasing constant $\delta = D \cdot \omega_0$ (which is an approach and valid for $D << 1$) leads to

$$\ddot{x} + 2 \cdot \delta \cdot \dot{x} + {\omega_0}^2 \cdot x = 0 \tag{2.13}$$

Using the exponential approach (Equation 2.8) leads to the Eigen values

$$\lambda_{1,2} = -\delta \pm \sqrt{\delta^2 - {\omega_0}^2} \tag{2.14}$$

Depending on the values of δ^2 and ${\omega_0}^2$ the Eigen values can be real or complex.

Three cases are possible:

Subcritical damping

$\underline{\delta^2 < {\omega_0}^2 \xrightarrow{\delta = D\cdot\omega} D < 1}$

For this case the Eigen values are:

$$\lambda_{1,2} = -\delta \pm i \cdot \underbrace{\sqrt{{\omega_0}^2 - \delta^2}}_{\omega} \tag{2.15}$$

The Eigen angular frequency of the damped system is defined:

$$\omega = \sqrt{{\omega_0}^2 - \delta^2} = \omega_0 \cdot \sqrt{1 - \frac{\delta^2}{{\omega_0}^2}} = \omega_0 \cdot \sqrt{1 - D}$$

$$\begin{aligned} &\Rightarrow \\ &x(t) = C_1 \cdot e^{(-\delta + i\cdot\omega)\cdot t} + C_2 \cdot e^{(-\delta - i\cdot\omega)\cdot t} \\ &= e^{-\delta\cdot t} \cdot \left(C_1 \cdot e^{(i\cdot\omega)\cdot t} + C_2 \cdot e^{(-i\cdot\omega)\cdot t}\right) \end{aligned} \tag{2.16}$$

Using the Euler equation on the term and $A = C_1 + C_2$ and $B = C_1 - C_2$, the final result of the decreasing vibration is:

$$x(t) = e^{-\delta\cdot t} * (A \cdot \cos(\omega \cdot t) + B \cdot \sin(\omega \cdot t)) \tag{2.17}$$

Velocities and accelerations are appropriate derivations of this equation.

With appropriate initial conditions (i.e. $x(t=0)=x_0$ and $\dot{x}(t=0)=v_0$) A and B can be found.

Supercritical damping

$\underline{\delta^2 > \omega_0^{\ 2} \xrightarrow{\delta=D\cdot\omega} D>1}$

$$\lambda_{1,2} = -\delta \pm \underbrace{\sqrt{\delta^2 - \omega_0^{\ 2}}}_{\delta_C} \tag{2.18}$$

In this case both Eigen values are real and negative. After the same procedure like before, the solution of the differential equation is:

$$\begin{aligned} & x(t) = e^{-\delta\cdot t} * \left(C_1 * e^{\delta_C\cdot t} + C_2 * e^{-\delta_C\cdot t}\right) \\ & e^{\pm x} = \sinh(x) \pm \cosh(x) \\ & \Rightarrow x(t) = e^{-\delta\cdot t} * \left(A\cdot\cosh(\delta_C\cdot t) + B\cdot\sinh(\delta_C\cdot t)\right) \end{aligned} \tag{2.19}$$

Critical damping

$\underline{\delta^2 = \omega_0^{\ 2} \xrightarrow{\delta=D\cdot\omega} D=1}$

In the case of critical damping, the characteristic equation has just one Eigen value:

$$\begin{aligned} & \lambda = -\delta = -\omega_0 \\ & \Rightarrow x(t) = C_1\cdot e^{\lambda\cdot t} + C_2\cdot t\cdot e^{\lambda\cdot t} \\ & x(t) = e^{-\delta\cdot t}\cdot(A + B\cdot t) \end{aligned} \tag{2.20}$$

Figure 2-23 was created on Matlab and plots the three different types of damping on a 50 Hz oscillation. The ordinate plots the relative position about the point of equilibrium (initial displacement: x_0); the abscissa plots the time.

In case of a subcritical damping, the oscillator overshoots, but can approach the point of equilibrium – depending on the damping ratio – pretty quickly. With a supercritical damping ratio an overshoot can be avoided, but the time to approach the point of equilibrium is higher. This plot shows also the low material damping of steel (D=0.0015): The curve hardly deviates from the free oscillation curve within the first few cycles.

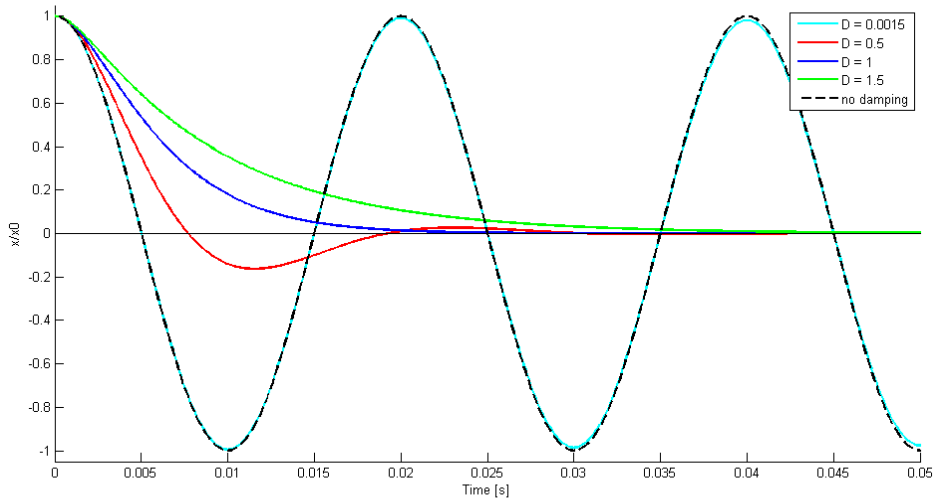

Figure 2-23: Results of different damping ratios on a 50 Hz oscillation

Typical values for the damping ratio D are listed in Table 2-1.

Table 2-1: Common material damping ratios [8]

Material	Damping Ratio D [-]
High strength steel	0.0003 … 0.0015
Construction steel	0.0025
Cast iron	0.01 … 0.05
Concrete	0.01 … 0.1

2.2.3 Forced Vibration

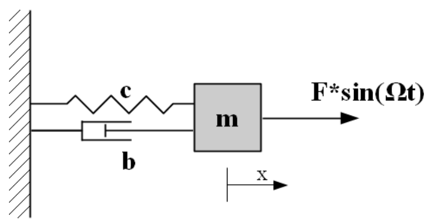

Figure 2-24: An excited, damped single mass oscillator at its point of equilibrium

Harmonic Excitation

The differential equation of a damped vibration has following structure (using the symbol declarations of the previous chapters):

$$\ddot{x} + 2 \cdot \delta \cdot \dot{x} + {\omega_0}^2 \cdot x = \frac{\hat{F}}{m} * \sin(\Omega \cdot t) \tag{2.21}$$

$\hat{F}$ is the exciting force amplitude, Ω the exciting frequency.
The solution of this equation is:

$$x(t) = \underbrace{\frac{\hat{F}}{c} \cdot \frac{1}{\sqrt{\left(1-\eta^2\right)^2 + 4 \cdot D^2 \cdot \eta^2}}}_{\hat{x}} \cdot \sin(\Omega \cdot t + \gamma - \varphi) \tag{2.22}$$

with

$$\eta = \frac{\Omega}{\omega_0} \tag{2.23}$$

and

$$\tan(\varphi) = \frac{2 \cdot D \cdot \eta}{1-\eta^2} \tag{2.24}$$

In equation (2.22) γ is the phase shift due to the combination of the spring force ($c \cdot x$) and damping force ($b \cdot \dot{x}$). φ is the phase shift between excitation force and the motion. $\hat{x}$ is the distance related amplitude.

Periodic, non-harmonic Excitation

For damped vibration systems, a periodic, non-harmonic excitation force is described by a Fourier series. The vibration equation is

$$\ddot{x} + 2 \cdot \delta \cdot \dot{x} + \omega_0{}^2 \cdot x = \sum_{k=1}^{\infty} \hat{F}_k * \sin(k \cdot \Omega \cdot t + \beta_k) \tag{2.25}$$

whereas

$$\sin(\beta_k) = \frac{a_k}{c_k}$$

$$\cos(\beta_k) = \frac{b_k}{c_k}$$

$$c_k = \sqrt{a_k{}^2 + b_k{}^2}$$

and a_k, b_k and c_k are the parameters which are to be solved by the Fourier analysis.
The solution of the equation is similar to the harmonic excited one. It's only valid for linear systems.

$$x(t) = \frac{1}{c} \cdot \sum_{k=1}^{\infty} \frac{\hat{F}_k}{\sqrt{(1 - k^2 \cdot \eta^2)^2 + 4 \cdot D^2 \cdot k^2 \cdot \eta^2}} \cdot \sin(k \cdot \Omega \cdot t + \beta_k - \varphi_k) \tag{2.26}$$

Figure 2-25 and Figure 2-26 plot an example:

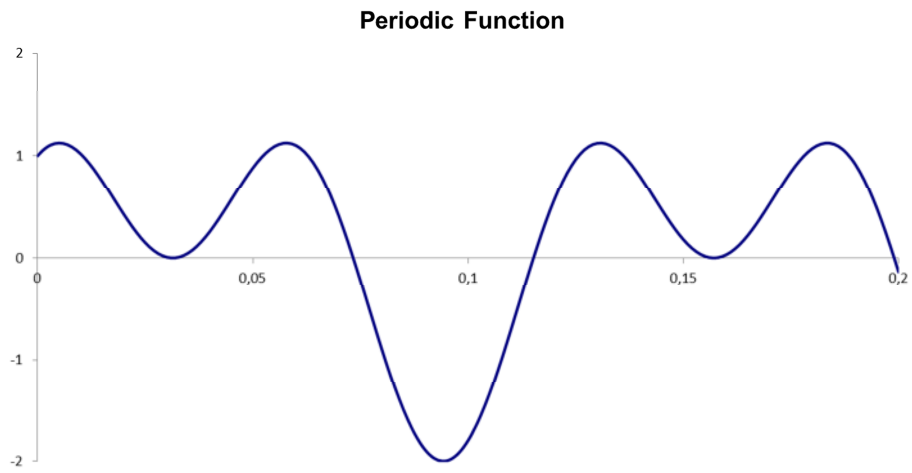

Figure 2-25: Non-harmonic, periodic function

Figure 2-25 plots a periodically repeating function. With the help of the Fourier analysis the function can be split up in its harmonic functions (Figure 2-26).

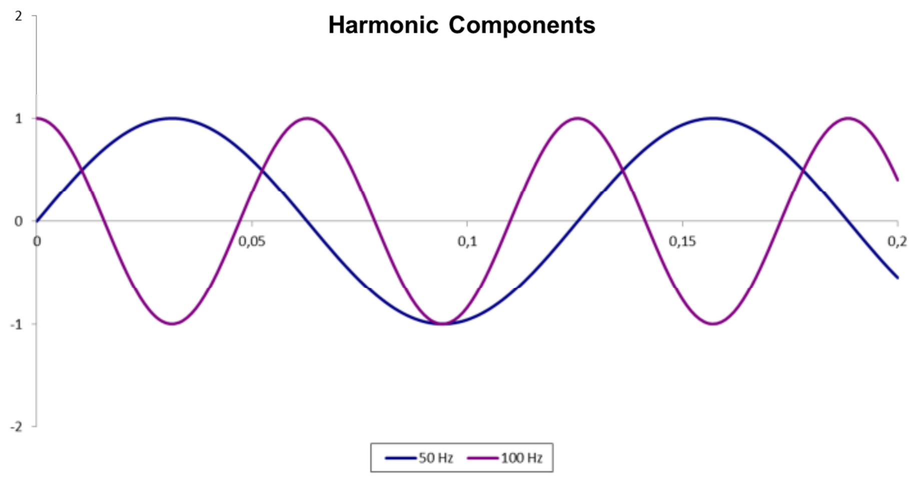

Figure 2-26: Harmonic components of the periodic function

Figure 2-26 shows the harmonic components of the periodic function in Figure 2-25. These harmonic functions summed up equals the periodic function again. So the periodic function in Figure 2-25 contains a 50 Hz oscillation and a 100 Hz oscillation with a phase shift of $\beta_k=\pi/2$.

2.3 Nyquist–Shannon Sampling Theorem

Some contents of this chapter originate from [11] and [12].

The Nyquist-Shannon sampling theorem is a fundamental result for converting a continuous signal into a numeric sequence. The theorem implies that any signal with a maximal frequency of f_{max} must be sampled with a frequency of at least $2*f_{max}$.

$$f_{sample} \geq 2 \cdot f_{\max} \tag{2.27}$$

Only if this theorem is fulfilled it can be ensured that the resulting time discrete signal has no loss of information and can be approximated as exact desired.
For illustration reasons, Figure 2-27 shows a plot of a 50 Hz frequency, which is once sampled fulfilling, and once not fulfilling equation 2.27.

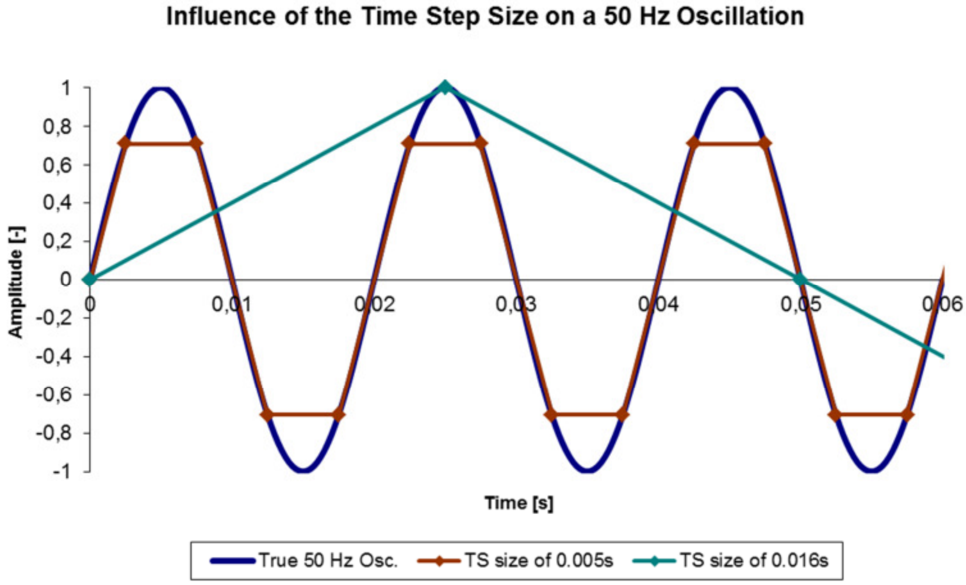

Figure 2-27: Influence of time step sizes

The dark blue line in Figure 2-27 plots the exact 50 Hz oscillation, which may represent an excitation force. To picture this oscillation properly with discrete time values, at least 2 time points with a constant time in between them are required per cycle. In this example $f_{sample} = 4 \cdot f_{\max}$ is chosen. The brown line shows the correct sampling of the 50 Hz oscillation. The square dots represent the discrete time points, which are congruent with the 50 Hz oscillation plot. It can be seen that the amplitude is pretty close to the original one. Also the zero crossing is almost identical. However, if two adjoined discrete time points are too far apart (resp. the sample frequency is too low), the oscillation might be pictured wrong. This is described by the green line. The green squared dots indicate the discrete time points, when the 50 Hz oscillation is tried to be pictured. Even though the squared dots are congruent with the 50 Hz oscillation, the total oscillation appears to be a 10 Hz oscillation. The sampled frequency would be wrong.

2.4 The Transfer Matrices Method

Some content and images of this chapter originate from [13].

To perform a manual estimation of the torsional Eigen frequencies, the transfer matrices method (TMM) can be used. The TMM is a method where inertia and stiffness properties are sequenced by using kinematic compatibility conditions and angular momentums.

Therefore the system is split into a finite amount of torque oscillators and torsional springs (see Figure 5-41).

A single element of a compound of torque oscillators and torsional springs is illustrated in Figure 2-28.

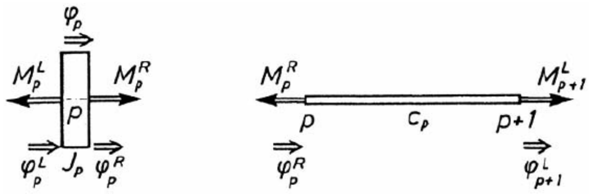

Figure 2-28: Single rotary mass and torsional spring [13]

The index P indicates the number of one single rotary mass in the whole system; the indices R and L indicate the position left or right of the mass P.

The equations describing what happens "in" the mass are:

$$\varphi_P^L = \varphi_P^R$$

$$M_P^L = \theta_P \cdot \omega^2 + M_P^R$$

The rotary mass is a rigid body (the elasticity is introduced by the springs), which is why the angles left and right of the mass remain the equal. The torque right of the mass equals the torque left of the mass, minus the torque needed to accelerate the mass (assuming that the torque is introduced on the left side).

Written in a matrix it is:

$$\underbrace{\begin{bmatrix} \varphi_P^R \\ M_P^R \end{bmatrix}}_{z_P^R} = \underbrace{\begin{bmatrix} 1 & 0 \\ -\theta_P \cdot \omega^2 & 1 \end{bmatrix}}_{P_P} \cdot \underbrace{\begin{bmatrix} \varphi_P^L \\ M_P^L \end{bmatrix}}_{z_P^L}$$

P_P is called point matrix, z_P is the state vector.

The massless spring between mass P and P+1 is described by following conditions:

$$M_P^R = M_{P+1}^L$$

$$M_{P+1}^L = c_P \cdot \left(\varphi_{P+1}^L - \varphi_P^R\right)$$

The spring is massless, which is why the torque along the spring remains constant. And the torque is depending from the spring stiffness and the relative amount of rotation between the two masses P and P+1.

Written in a matrix again, it is:

$$\begin{bmatrix} \varphi_{P+1}^{L} \\ M_{P+1}^{L} \end{bmatrix} = \underbrace{\begin{bmatrix} 1 & \frac{1}{c_P} \\ 0 & 1 \end{bmatrix}}_{F_P} \cdot \begin{bmatrix} \varphi_{P+1}^{R} \\ M_{P}^{R} \end{bmatrix}$$

FP is called field matrix.

These matrices are valid for masses in between the whole system. An open end (no torque, but torsion → M_P=0) of the spring-mass string is described by the state vector

$$z_P = \begin{pmatrix} 1 \\ 0 \end{pmatrix},$$

a clamped end (no torsion, but torque → φ_P=0) by the state vector

$$z_P = \begin{pmatrix} 0 \\ 1 \end{pmatrix}.$$

Now, in general, a single spring-mass system is defined by following equation:

$$z_{P+1}^{L} = z_P^{R} \cdot F_P = F_P \cdot P_P \cdot z_P^{L} = z_P^{L} \cdot U_P$$

U_P is the transfer matrix which represents the relation of the conditions left of Mass P and left of mass P+1.

In practice, the Falk schema is used for calculation to keep the track of a large amount of rotary masses and springs.

2.5 *Theory of Strength*

Some content of this chapter (including subchabpters) originate from [2] and [14].

The strength theory is used to reduce multiaxial stress to uniaxial stress, which is comparable with results received from a tensile test. This means the simple results from a tensile test (i.e. the yield stress σ_F) are not enough to predict if a certain multiaxial stress causes yielding. Now the question is: does a certain multiaxial stress cause yielding (for a ductile material), breaking (for brittle materials) or – in general – a failure?
In in Chapter 7.4 of this thesis, the maximum shear stress criterion by von-Mises is used. Besides the von-Mises criterion there is also the criterion by Tresca (for ductile materials), the criterion by Rankine (for brittle materials) and the criterion by Mohr-Coulomb and Drucker - Prager for materials which show different behavior on compression and tension.

2.5.1 von-Mises Criterion

The von-Mises criterion is based on the stress of an octahedron. Therefore an octahedral shape is positioned into a stress loaded body. The axes of the octahedron are congruent with the principal stress directions.
Figure 2-29 shows such an octahedron, with its axes aligned congruent to the principal stress directions (σ_{11}, σ_{22}, σ_{33}).

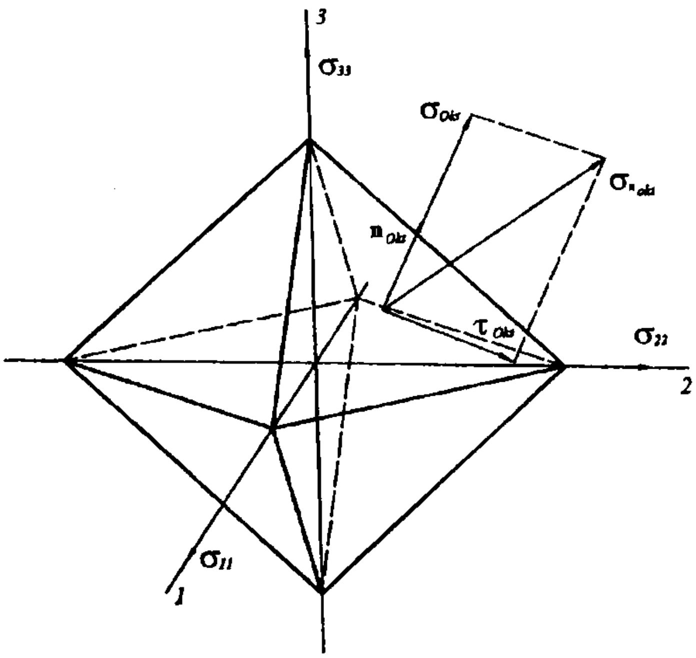

Figure 2-29: Octahedron [14]

As the octahedron's axes are congruent with the principal stress directions, the stress tensor S is:

$$S = \begin{bmatrix} \sigma_{11} & 0 & 0 \\ 0 & \sigma_{22} & 0 \\ 0 & 0 & \sigma_{33} \end{bmatrix}$$

As the outer surfaces of the octahedron are not aligned normally to one of the axes, the surface normal n_{Okt} is required.

$$n_{Okt} = \begin{bmatrix} \frac{1}{\sqrt{3}} \\ \frac{1}{\sqrt{3}} \\ \frac{1}{\sqrt{3}} \end{bmatrix}$$

With the help of the Cauchy equation it is possible to determine the stress vector of any surface, which is not aligned normally to one of the axes.

So the stress, acting on the surface (related to Figure 2-29), is:

$$\sigma_n = S^T \cdot n_{Okt} = \begin{bmatrix} \sigma_{11} & 0 & 0 \\ 0 & \sigma_{22} & 0 \\ 0 & 0 & \sigma_{33} \end{bmatrix} \cdot \begin{bmatrix} \frac{1}{\sqrt{3}} \\ \frac{1}{\sqrt{3}} \\ \frac{1}{\sqrt{3}} \end{bmatrix} = \frac{1}{\sqrt{3}} \cdot \begin{bmatrix} \sigma_{11} \\ \sigma_{22} \\ \sigma_{33} \end{bmatrix}$$

By projecting σ_n to the surface normal n_{Okt}, the normal stress σ_{Okt} can be determined:

$$\underline{\sigma_{Okt} = \sigma_n^T \cdot n_{Okt} = \frac{1}{3}(\sigma_{11} + \sigma_{22} + \sigma_{33})} \qquad (2.28)$$

Projecting σ_n onto the surface delivers the shear stress.

Using the theorem of Pythagoras delivers:

$$\tau_{Okt}^2 = \sigma_n^T \cdot \sigma_n - \sigma_{Okt}^2 = \frac{1}{3} \cdot \left(\sigma_{11}^2 + \sigma_{22}^2 + \sigma_{33}^2\right) - \frac{1}{9}\left(\sigma_{11} + \sigma_{22} + \sigma_{33}\right)^2$$

$$\Rightarrow \underline{\tau_{Okt} = \frac{1}{3} \cdot \sqrt{\left(\sigma_{11} - \sigma_{22}\right)^2 + \left(\sigma_{22} - \sigma_{33}\right)^2 + \left(\sigma_{33} - \sigma_{11}\right)^2}} \qquad (2.29)$$

The uniaxial situation of a tensile test is described this way:

$$\sigma_{11} = \sigma_V$$

$$\sigma_{22} = \sigma_{33} = 0$$

$$\Rightarrow \left(\tau_{Okt}\right)_V = \frac{1}{3}\sigma_V \sqrt{2} \qquad (2.30)$$

Equating τ_{Okt} of the uniaxial tensile test (equation 2.30) with τ_{Okt} of the octahedral surface (equation 2.29) delivers the equivalent stress σ_V:

$$\frac{1}{3} \cdot \sqrt{\left(\sigma_{11} - \sigma_{22}\right)^2 + \left(\sigma_{22} - \sigma_{33}\right)^2 + \left(\sigma_{33} - \sigma_{11}\right)^2} = \frac{1}{3}\sigma_V \sqrt{2}$$

$$\Rightarrow \underline{\sigma_V = \sqrt{\frac{1}{2} \cdot \left[\left(\sigma_{11} - \sigma_{22}\right)^2 + \left(\sigma_{22} - \sigma_{33}\right)^2 + \left(\sigma_{33} - \sigma_{11}\right)^2\right]}} \qquad (2.31)$$

3 The FE Model

Most static and dynamic problems are solved with the help of the FE software ANSYS. Therefore a finite element model of the stator (and every other calculated part) is required. If the correspondence to a machines behavior in reality is not a primary issue, it might be helpful to use a very simplified model of the object of interest. Simple models are pretty fast generated, calculated and easily checked for plausibility. Especially for this case, where all models have very similar outlines, simple models can be created parametrically with the APDL very fast. A further advantage of simple kept models in this thesis is that small design differences among single generators are not regarded. This makes it much easier to compare reference projects among each other. Hence it is easier to find trends and influences of different parameter (diameters, number of shelves, etc.) on the dynamic behavior. But, as mentioned, in contrast to that, the absolute results do not represent the machine's real ones.

3.1 The Basic Stator Model

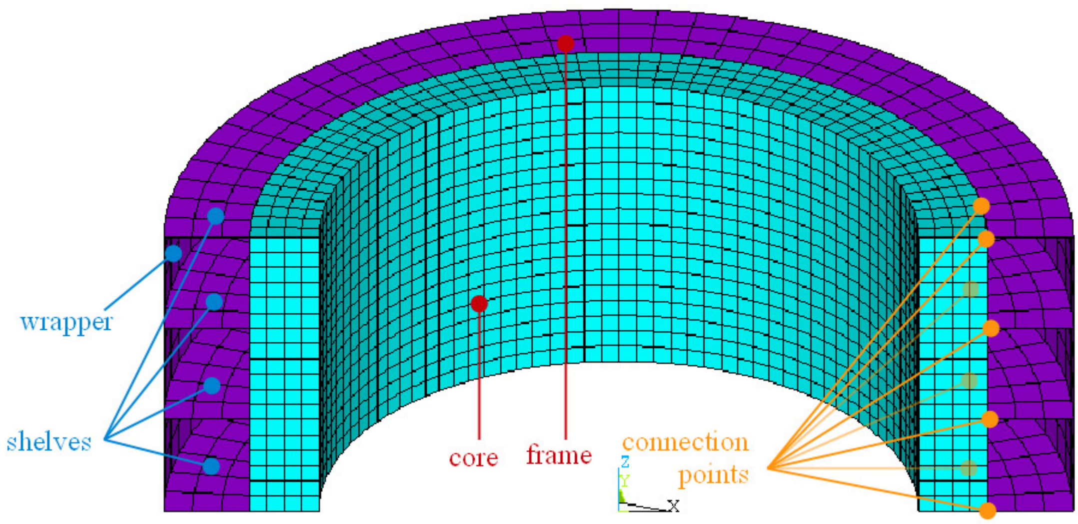

Figure 3-30: FE model of the stator of "Birkapili"

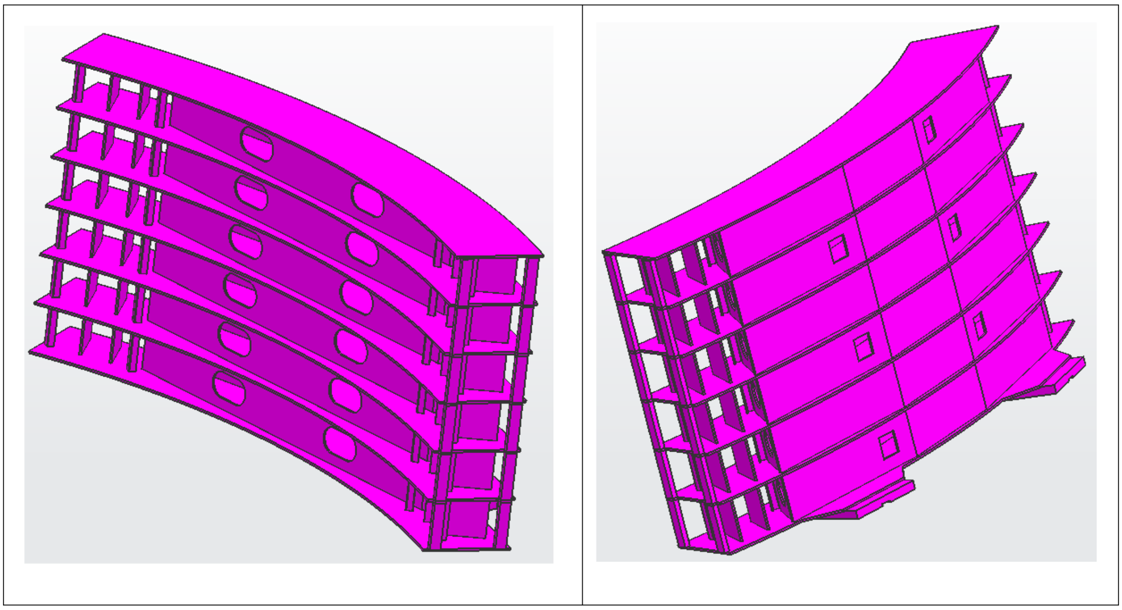

Figure 3-31: CAD model of the frame of "Mica" (dovetail bars are not shown)

The stator core is modeled as a cylindrical shaped, solid body, with no air slots and no teeth. This means that for all calculations in this thesis, the inner diameter of the core equals the yoke diameter (inner diameter of red area in Figure 3-38). So the inner core diameter does not include the teeth, but the teeth's mass is regarded by increasing the core's / yoke's density value (Equation (3.32)).

The mass and stiffness of the winding coils is not regarded. The coils consist of different materials with very different volume and mass proportions and different head winding heights for every machine. This would make a comparison of the principal influencing factors among the reference models more difficult again.

The stator frame in the calculation model is just made up of its shelves, which all have the same thickness, and of its wrapper. The lowermost and uppermost shelf is on the same axial level like the lower and upper end of the core. The frame's inner diameter is assumed to be the same like the core's outer diameter; the radial length of the key bars is not regarded, which means that the core is directly attached to the shelves. These connection points are at the exact same tangential position where the key bars are located. The core is axially, radially, tangentially connected to the frame at these locations.

The soleplates (Figure 3-32 and Figure 3-33) are in terms of their radial location also abstracted. They are represented by tangentially and axially fixed[4] nodes (henceforth these

[4] "Fixed" means that a boundary condition (BC) of Zero displacement is applied

nodes are called "soleplate nodes"), reaching from the shelf center[5] to the wrapper. In reality, the radial inner edge of the soleplate is also approximately at the shelf center but the outer edge would reach further outside (see Figure 3-31, view on the right hand side). Some machines have a non-uniform angular distance between their soleplates. Nevertheless have the soleplates of the calculation models regular angular distances in the calculation model.

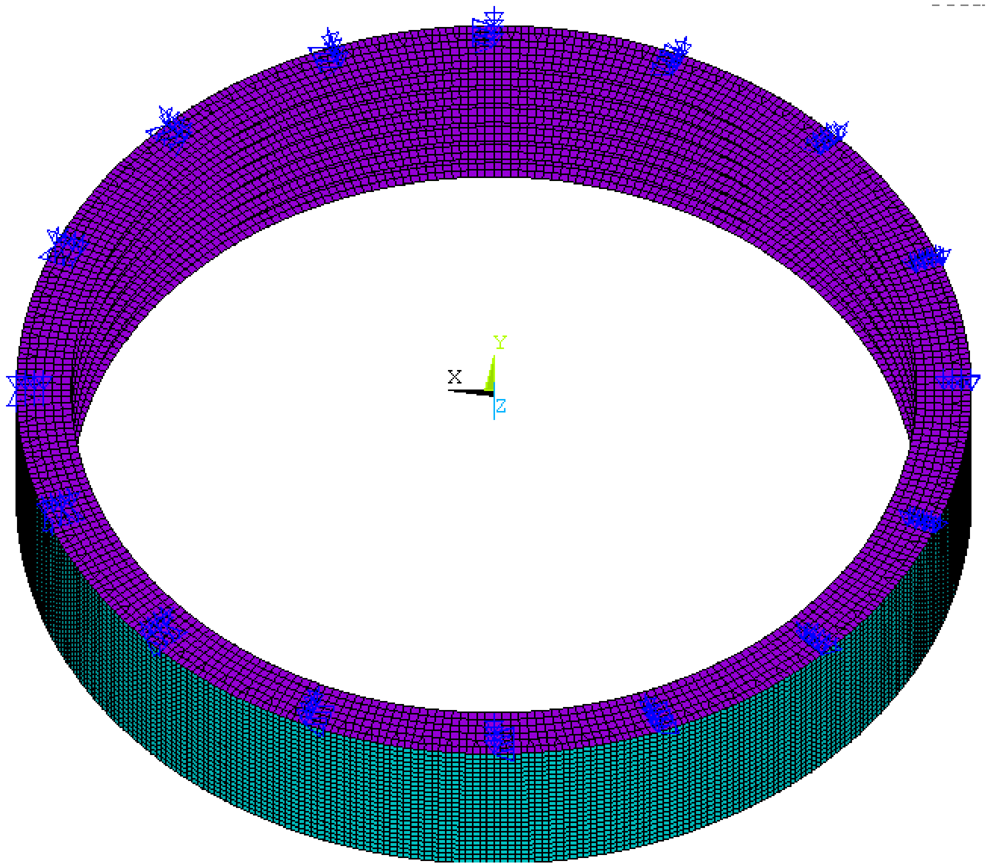

Figure 3-32: Bottom view "Mica's" frame with tangential and axial BC

[5] The shelf center is the radial midpoint between the inner and outer diameter of the shelf.

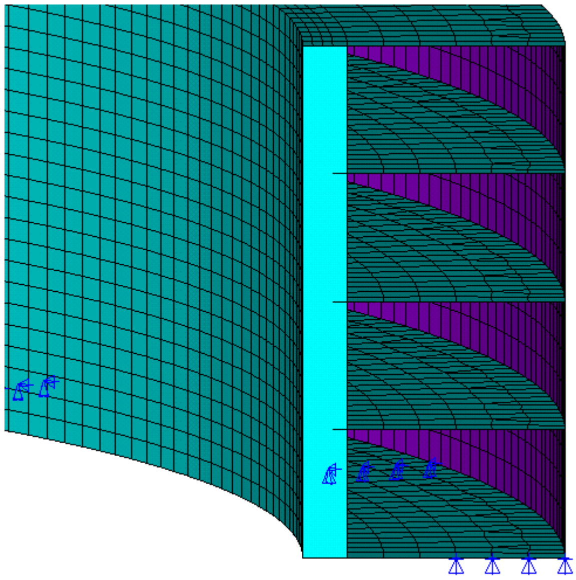

Figure 3-33: 4 sole plate nodes of each soleplate at "Caruachi" (BC showing through elements)

The stator core is made of 8-noded SOLID45 elements in ANSYS (cyan colored in Figure 3-30). The frame is made of 4-noded SHELL63 elements (purple colored in Figure 3-30), with a mathematical thickness applied by different real constants.

Comparing Figure 3-30 with Figure 3-31 the differences between the simplified FE model and the real design can be seen. The biggest difference is the structure between the shelves of the frame. This structure differs from project to project. The view on the right hand side of Figure 3-31 shows the wrapper of the frame. The wrapper is discontinued on the both ends of this frame section. This is where the coolers are applied. These openings cause a loss of stiffness, which is also not regarded in the simplified model.

3.1.1 The Core-to-Frame Connection

As explained before, the frame of the FE model is built up of shell elements, whereas the core is made of solid brick elements. Nodes, building up these elements, have different properties concerning their degrees of freedom.

Any deformation of a solid brick element can be described just by translating its nodes (→ 3 degrees of freedom per node, one for each axis). Nodes of a shell element have 6 degrees of freedom (additional 3 rotational degrees, one for each axis) to describe deformations.

Connecting these two element types is not trivial. An ordinary node-to-node connection would deliver wrong results (Figure 3-34, left). As solid elements don't have rotational degrees of freedom, the torque, caused by force F in Figure 3-34, will not appear in the reaction force of the bearings.

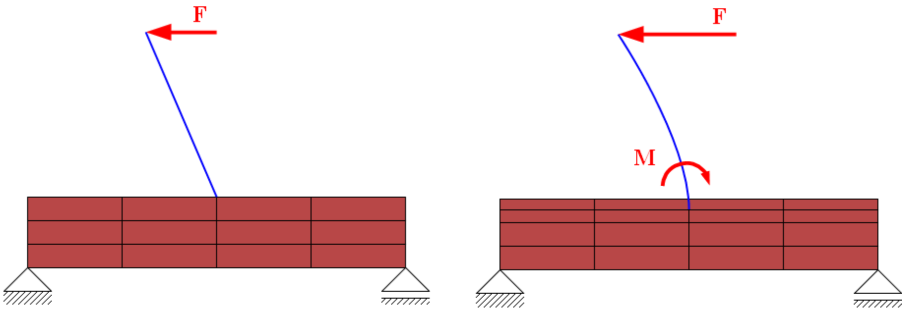

Figure 3-34: Illustration of the shell-solid connection problem (blue: shell elements; red: solid elements / left: no torque is transferred over nodes; right: torque transferred by displacing two nearby nodes)

ANSYS recommends using contact elements to establish a bonded contact and to arrange a proper connection this way. But as the locations of interests (the soleplates) are relatively far away from the core-to-frame connection nodes, following approach provides sufficient accuracy:

As sketched in Figure 3-34 (right) and Figure 3-35, the shell element is extended by a very few millimeters into the direction of the solid body so that the shell overlaps with the solid element. The solid body (core) gets an additional row of elements, which is as thin as possible[6]. The shell element gets connected to the solid body on two nodes at the top and bottom edge of the new element. This is how the torque can be transferred by translation of two nodes properly.

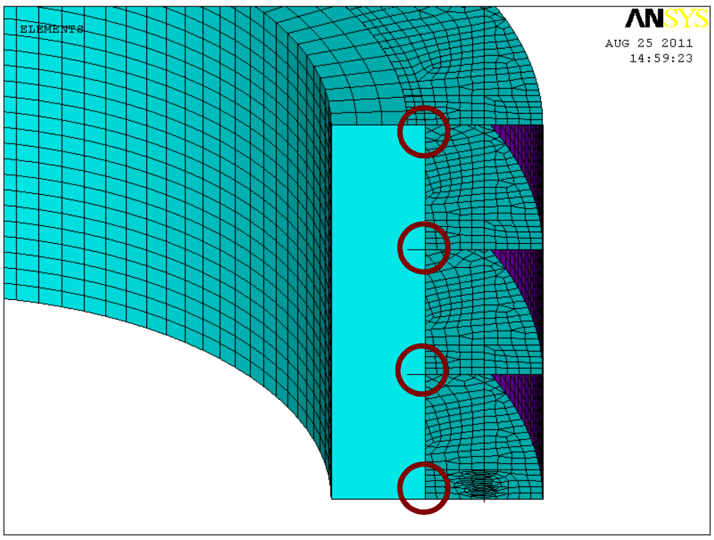

Figure 3-35: Shelves extended into core for a proper connection

[6] Element aspect ratios must not be exceeded.

3.2 Finite Element Sizes

The size of finite elements plays an important role if stress and strains are supposed to be evaluated at certain locations. For modal analyses the element size plays a minor role. Depending on the mode shape, elements must be small enough to have enough nodes (resp. degrees of freedom) to represent all shapes of interest.

This means that the axial number of core nodes is important if the torque modes of the stator core are of note. The number of axial nodes equals the maximal amount of torsional modes. The amount of angular and radial nodes has just a minor influence on the torsional mode frequencies (as long as the geometry is not influenced by using too large element sizes).

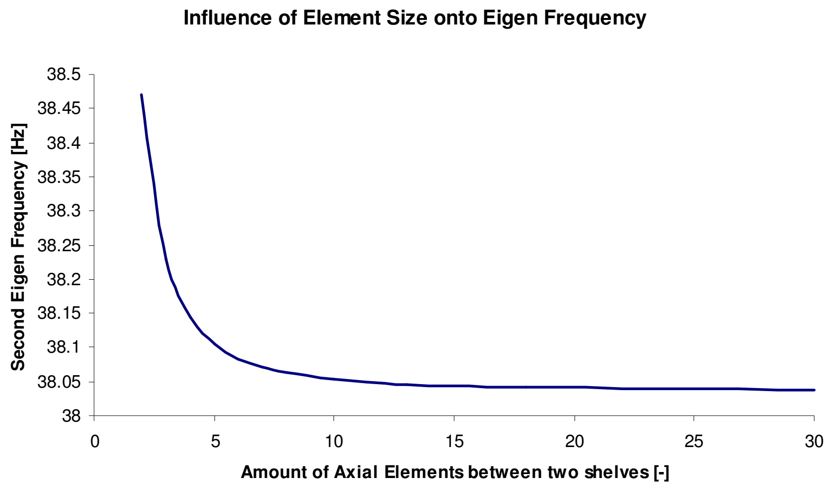

Figure 3-36: Influence of the element size on the 2nd Eigen frequency of a core, without the frame attached

Even though the curve shown in Figure 3-36 has a huge drop at the left end, the relative frequency differences are low. Anyhow, for the following calculations a value of 8 elements between each shelf has shown to be a good compromise between calculation time and accuracy. The angular amount of elements is 3 (between two key bars), so is the total amount of radial elements.

To gain an appropriate element size for the frame, the stiffness at the core-to-frame connection is evaluated (Figure 3-37).

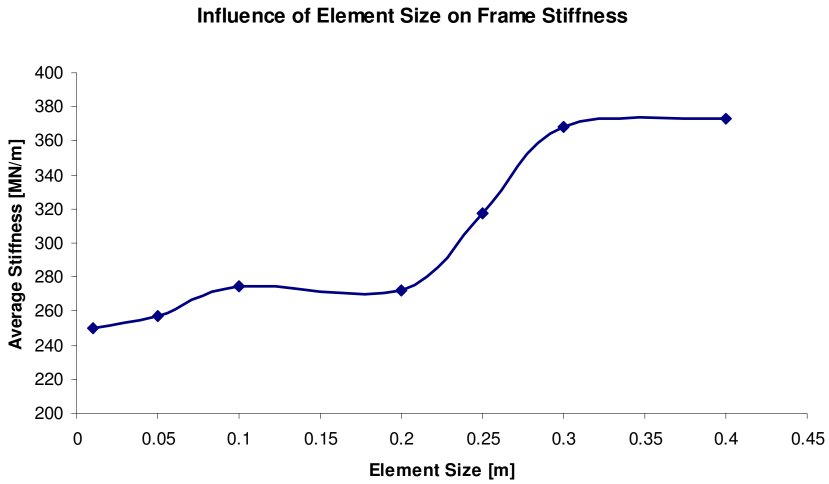

Figure 3-37: Influence of the element size on the frame's FE-calculated stiffness

A good compromise between calculation time and result accuracy is an element size between 0.1 m and 0.2 m.

3.3 Materials and its Properties

3.3.1 Stator Core Material Properties

As initially mentioned, the stator core is built of layered electrical steel sheets which are coated on both sides and clamped together after stacking. The combination of the sheet metal properties, the insulation material properties and the pressure makes it difficult to gain overall properties for a solid modeled core. Significant values must be determined by experiments. Some experiments have already been performed by Andritz Hydro, but the results among these experiments differ. The most transparent reports [15], [16] have been used to achieve the properties for the stator core.

Table 3-2: Material constants of the stator core

Symbol	Value	Unit	Description
E_r [15]	155E3	MPa	Young's modulus in radial direction.
E_y [15]	138E3	MPa	Young's modulus in tangential direction.
E_z [15]	0.8E3	MPa	Young's modulus in axial direction.
G_{xy} [15]	40E3	MPa	Shear modulus in axial direction.
G_{xz} [16]	103	MPa	Shear modulus in radial direction.
G_{yz} [16]	103	MPa	Shear modulus in tangential direction
ρ_{St}	7800	kg/m^3	Density of the layered stator core (steel)

As mentioned, the air and winding slots are regarded in the core's density for the FE calculation. The resultant density is:

$$A_{teeth} = \left((r_C + l_{tooth})^2 - r_C{}^2\right) \cdot \pi$$

$$A_{yoke} = \left(R_C - \left(r_C{}^2 + l_{tooth}\right)^2\right) \cdot \pi$$

$$\rho_{teeth} = \frac{w_{tooth}}{w_{tooth} + w_{gap}} * \rho_{St}$$

$$\rho_{eq} = \left(\frac{V_{teeth}}{V_{yoke}} \cdot \rho_{teeth} + \rho_{St}\right) \cdot \frac{h_c}{h_{St}} \qquad (3.32)$$

A_{teeth} .... Teeth cross section area (see Figure 3-38) [m^2]
A_{yoke}....................... Yoke cross section area (see Figure 3-38) [m^2]
l_{tooth} .... Radial tooth length [m]
ρ_{teeth}....................... Density of the teeth area, regarding the winding slots with a density of 0 [kg/m^3]
w_{tooth} .... Tooth width [m]
w_{gap} .... Tooth gap width [m]
ρ_{eq} .... Equivalent core density, regarding air slots and teeth mass [kg/m^3]
h_c........................... Total core height [m]
h_{St}.......................... Stack height (core height without air slots) [m]

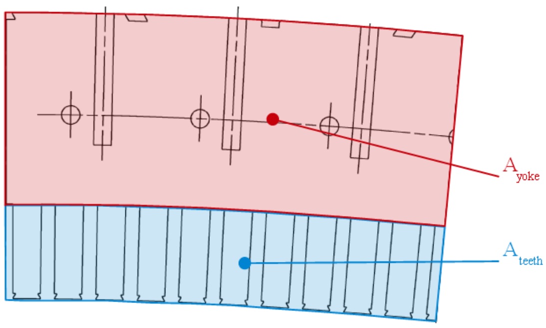

Figure 3-38: Illustration of the yoke and teeth cross section area

3.3.2 Stator Frame Material Properties

The stator frame is a welded structure of commonly used steel sheets (ASTM A36[7]) with isotropic material behavior. The usual sheet thickness used for the shelves and the wrapper is about 20mm. Depending on demands the thickness of some sheets might also exceed 30mm. Anyhow, the material properties of this used steel are listed in Table 3-3.

Table 3-3: Material constants for the stator frame

Symbol	Value	Unit	Description
E	2.1e5	MPa	Young's modulus
υ	0.3	-	Poisson ratio
ρ_{St}	7800	kg/m^3	Density of steel

Furthermore the mass of the upper bracket, which is attached to the frame in some cases, is not regarded. As mentioned, the target is to compare the dynamic behavior by a very simplified model, to be able to see influences of basic geometric parameters. Different bearings and brackets would make a comparison more difficult again.

3.3.3 Damping

As the transient FE calculations in this thesis examine just a very small time range, the effect of damping is negligible. So damping is not regarded in any of the following dynamic calculations.

[7] S235

4 Reference Projects

To figure out which geometries affect the dynamic behavior in a certain way, a list of ten generators (some of them exist already, some are under construction) has been generated, to have a wide range of dimensions, speed and power output to look at. The electrical characteristics can be found in Table 4-4. The major dimensions are listed in Table 4-5, further detailed dimensions can be found in Table 4-6.

Table 4-4: Ratings of reference projects

Project Name	Grid Frequency [Hz]	Speed [rpm]	Power Factor [-]	Rated Power [MVA]	Output Power [MW]
Symbols (if used)	f_g		η_{PF}	R	P
Mica	60	133.3	0.9	570	513
Bad Creek	60	300	-	313	-
SM3	60	257.1	0.95	440	418
THP	50	500	0.9	333	299.7
NT2	50	333.3	-	281.5	-
R2/R7	50	120	0.85	19	16.15
Caruachi	60	94.7	0.85	220	187
Caojie	50	68.1	-	143	-
Lower Mattagami	60	100	-	87.3	-
Birkapili	50	750	0.9	66.8	60.12

Table 4-5: Main dimensions of reference projects

Project Name	Core Inner Diameter [m]	Core Outer Diameter [m]	Core Height [m]	Number of Key Bars [-]	Frame Outer Diameter [m]	Number of Shelves [-]	Number of Soleplates [-]	Mass of Frame [kg]	Mass of Core [kg]
Symbol (if used)	d_{CT}	D_C	h_C		D_f		n_{SP}	m_F	m_C
Mica	13.300	13.870	2.784	108	15.66	7	16	66701	300546
Bad Creek	6.731	7.341	2.985	72	8.641	6	8	26592	179386
SM3	7.640	8.250	3.200	60**	9.762	7	16	36829	213265
THP	5.136	5.950	3.050	56**	7.530	7	8	28118	183475
NT2	6.580	7.314	2.260	80	8.978	5	12	26552	151456
R2/R7	6.240	6.450	0.760	56	7.474	3	8	7644	16663
Caruachi	12.437	12.802	2.121	96	14.585	5	16	42934	233809
Caojie	14.689	15.070	1.300	96	17.064	4	24	50357	109142
Lower Mattagami	10.860	11.100	1.270	80	12.520	4	8	24230	54756
Birkapili	2.795	3.435	1.475	36	4.238	4	8	5792	41174

Table 4-6: Detailed dimensions of reference projects

Project Name	Tooth Width [m]	Tooth Gap Width [m]	Tooth Gap Depth [m]	Number of Air Slots [-]	Thickness of Air Slots [m]	Frame Shell Thickness [m]	Frame Shelf Thickness [m]	Equiv.C. Dens. [kg/m3] ***
Mica	.025	.022	.150	59	.005	.020	.020*	8875
Bad Creek	.039	.039*	.178	84 (+7)	.003 (.005)	.019	.019*	8909
SM3	.039	.039*	.140	62	.004	.019	.019*	8754
THP	.044	.044*	.193	62	.005	.019	.019*	8488.5
NT2	.055	.055*	.140	50	.004	.02	.020*	8366.9
R2/R7	.033	.033*	.120	17	.006	.019	.019*	10475.3
Caruachi	.043	.043*	.122	49	.005	.019	.019*	9212.5
Caojie	.053	.053*	.135	33	.004	.019	.019*	9427.9
Lower Mattagami	.025	.046	.180	27	.005	.02	.020*	10415.8
Birkapili	.055	.055*.	.127	32	.005	.019	.019*	8181.2

*) Values are assumed.

**) Decreased to an even amount to ease the modeling.

***) Regards air gaps and teeth mass; calculation see equation (3.32) in Chapter 3.3.1.

5 Basic Dynamic Behavior of the Stator

Before having a closer look to the actual problem (the investigation of the soleplate reaction forces in case of an electrical failure), the natural frequencies of all reference projects are examined. The reason therefore is that the dynamic behavior of a body strongly depends on its natural frequencies. Furthermore all single projects with their different dimensions can be compared easily by the hand of their natural frequencies. This way it is possible to predict in which way the dynamic behavior is affected by i.e. the number of shelves or any other geometric parameter.

5.1 Natural Frequencies of the Core

At the beginning the natural frequencies of the core only (without the frame attached) are determined, to see the influence of the core's mass, stiffness and dimensions.

The range of interesting natural frequencies leads from **0 Hz to 140Hz**. (The excitation frequencies of the faulty torque are, as mentioned, the single and double grid frequency, which is – depending on the country's grid system – up to 120 Hz plus a safety factor.) Radial magnetic forces, which dominate during regular operation, are left aside so that the only modes of interest are those in tangential direction. Therefore it is enough to give all nodes of the FE model just one degree of freedom, which is in tangential direction. This may distort some natural frequencies (especially those who are symmetric along an axial plane, seen in Figure 5-40). But the essential modes, which will be excited primarily in a case of electrical faults, will not be influenced (Figure 5-39). This procedure allows a faster computation and an easier interpretation. A detailed analysis concerning this simplification issue has been done in Chapter 6.5.

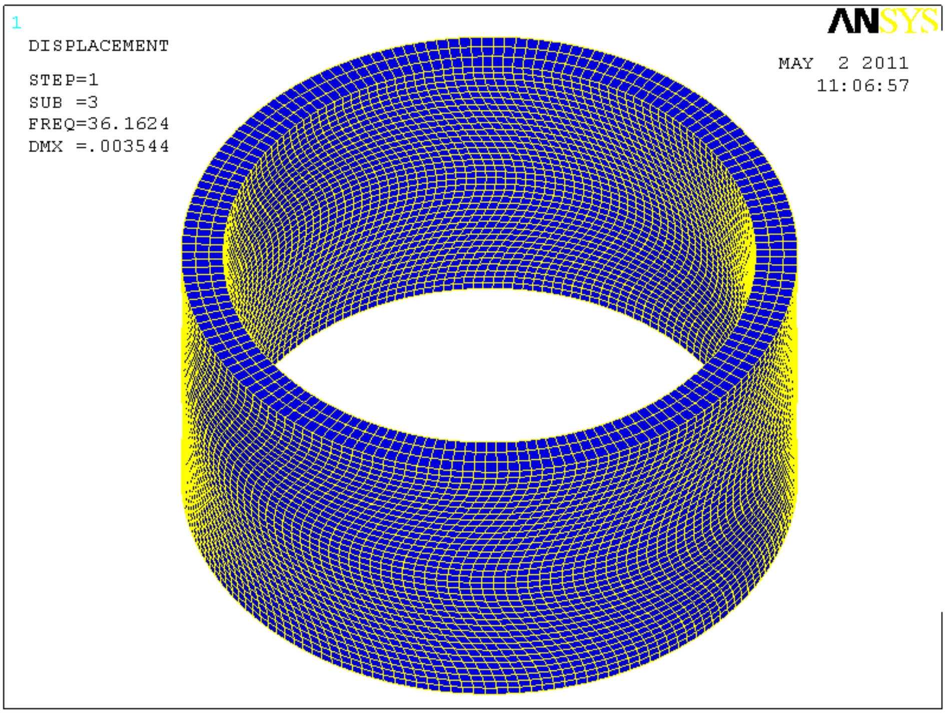

Figure 5-39: 1st order torsional mode shape, anti-symmetric

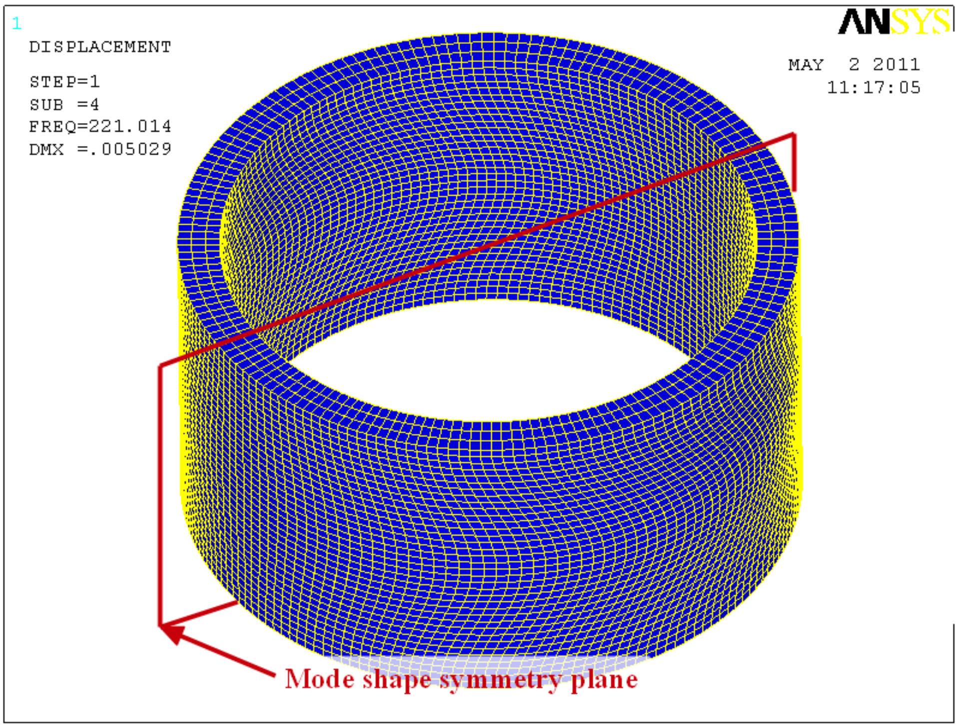

Figure 5-40: Torsional mode shape, which can not be excited by torque

5.1.1 Natural Frequencies of the Core – not Regarding the Stator Frame

This chapter is divided into three subchapters. To verify the accuracy and rightness of the FE model, the first chapter deals with a analytical estimation of the core's natural frequencies by means of the transfer matrices method. The second chapter is a FE calculation, but with the same abstracted model as it was used for the analytical estimation (only 1-D rotary masses and springs). The third part is the modal analyses with the solid FE model of the stator core.

Analytical estimation of a simplified model of "Mica"

The analytical estimation is done by means of the TMM, explained in Chapter 2.4.

Therefore the stator core is split into 3 finite torque oscillators, connected by massless torsional springs (see Figure 5-41). With this model it is possible to calculate the first 3 modes, as it has 3 degrees of freedom. The more degrees of freedom (resp. the more torque oscillators the core is split into) the more modes can be calculated and the more accurate the result will be.

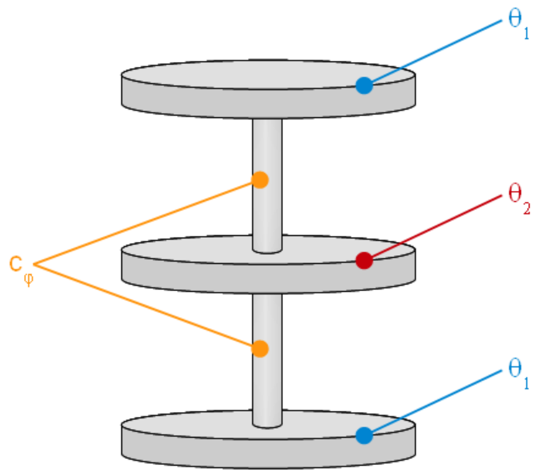

Figure 5-41: Equivalent system of the stator core

As the stator core is a simple cylinder (and the frame is not attached) the mass moments of inertia can be calculated easily. Also the shear modulus is known what establishes the calculation of the torsional spring stiffness.

The essential geometric and mechanic values are summarized in Table 5-7. They can also be found in Table 4-5, Table 4-6 and Table 3-2.

Table 5-7: Geometric and mechanical properties for a manual Eigen frequency estimation

Symbol	Value	Unit	Description
h_C	2.784	m	Stator core height
r_C	6.650	m	Stator core inner radius (excluding teeth length)
R_C	6.935	m	Stator core outer radius
G_{yz}	0.103E9	N/m^2	Stator core shear modulus
ρ_{equ}	8875.4	kg/m^3	Equivalent stator core density

Using the appropriate values, the mass moment of inertia and the torsional spring stiffness can be calculated.

$$I_P = \frac{\left(R_C{}^4 - r_C{}^4\right)\cdot \pi}{2} = 651.441 m^4$$

$$l = \frac{h_C}{2} = 1.392 m$$

$$c_\varphi = \frac{G_{yz} \cdot I_P}{l} = \underline{4.154 \cdot 10^{10} \frac{Nm}{rad}}$$

$$r_{C\_m} = r_C + \frac{R_C - r_C}{2} = 6.793 m$$

$$\theta = m * r_{C\_m}{}^2 = \underline{1.387 \cdot 10^7 \, kg \cdot m^2}$$

I_P	Polar area moment of inertia [m^4]
l	Distance between two rotary masses [m]
c_φ...........................	Torsional spring stiffness [Nm/rad]
r_{C_m}........................	Average radius of the stator core [m]
θ	Mass moment of inertia (of the total core) [kgm^2]

The mass moments of inertia of the reduced rotary masses are $\theta_1 = \theta/4$ and $\theta_2 = \theta/2$. (Indices according Figure 5-41).

Using the TMM, the first 3 mode frequencies can be calculated. To calculate the Eigen values, this term is substituted by λ during the Falk schema:

$$\frac{\theta}{c_\varphi} \cdot \omega^2 = \lambda \tag{5.33}$$

Point Matr. **Field Matr.**	**State vector after particular mass / spring**	
	$\begin{pmatrix}1\\0\end{pmatrix}$ ← State vector of an open end	$=\begin{pmatrix}\hat{\varphi}_0\\ \hat{M}_0\end{pmatrix}$
$\begin{pmatrix}1 & 0\\ -\frac{\theta\omega^2}{4} & 1\end{pmatrix}$	$\begin{pmatrix}1\\ -\frac{\theta\omega^2}{4}\end{pmatrix}$	$=\begin{pmatrix}\hat{\varphi}_1\\ \hat{M}_1\end{pmatrix}$
$\begin{pmatrix}1 & \frac{1}{c_\varphi}\\ 0 & 1\end{pmatrix}$	$\begin{pmatrix}1-\frac{\lambda}{4}\\ -\frac{\theta\omega^2}{4}\end{pmatrix}$	$=\begin{pmatrix}\hat{\varphi}_2\\ \hat{M}_2\end{pmatrix}$
$\begin{pmatrix}1 & 0\\ -\frac{\theta\omega^2}{2} & 1\end{pmatrix}$	$\begin{pmatrix}1-\frac{\lambda}{4}\\ -\frac{\theta\omega^2}{2}+\lambda\frac{\theta\omega^2}{8}-\frac{\theta\omega^2}{4}\end{pmatrix}$	$=\begin{pmatrix}\hat{\varphi}_3\\ \hat{M}_3\end{pmatrix}$
$\begin{pmatrix}1 & \frac{1}{c_\varphi}\\ 0 & 1\end{pmatrix}$	$\begin{pmatrix}1-\lambda\frac{1}{4}-\lambda\frac{1}{2}+\lambda^2\frac{1}{8}-\lambda\frac{1}{4}\\ -\frac{\theta\omega^2}{2}+\lambda\frac{\theta\omega^2}{8}-\frac{\theta\omega^2}{4}\end{pmatrix}$	$=\begin{pmatrix}\hat{\varphi}_4\\ \hat{M}_4\end{pmatrix}$
$\begin{pmatrix}1 & 0\\ -\frac{\theta\omega^2}{2} & 1\end{pmatrix}$	$\begin{pmatrix}1-\lambda\frac{1}{4}-\lambda\frac{1}{2}+\lambda^2\frac{1}{8}-\lambda\frac{1}{4}\\ -\frac{\theta\omega^2}{4}+\lambda\frac{\theta\omega^2}{16}+\lambda\frac{\theta\omega^2}{8}-\lambda^2\frac{\theta\omega^2}{32}+\lambda\frac{\theta\omega^2}{16}-\frac{\theta\omega^2}{2}+\lambda\frac{\theta\omega^2}{8}-\frac{\theta\omega^2}{4}\end{pmatrix}$	$=\begin{pmatrix}\hat{\varphi}_5\\ \hat{M}_5\end{pmatrix}$ $=\begin{pmatrix}1\\0\end{pmatrix}$

$$\hat{M}_5 = 0 = \theta\omega^2 \cdot \left(-\frac{1}{32}\lambda^2 + \frac{6}{16}\lambda - 1\right).$$

$$\lambda_1 = 4$$

$$\lambda_2 = 8$$

$$\underline{\omega_0 = 0Hz}$$

Re-substituting λ (Equation 5.33) delivers the free natural frequencies:

$$\omega = \sqrt{\lambda \cdot \frac{c_\varphi}{\theta}}$$

$$\omega_1 = \sqrt{4 \cdot \frac{4.154 \cdot 10^{10}}{1.387 \cdot 10^7}} = 109.472\frac{rad}{s} \mathrel{\hat{=}} \underline{17.4Hz}$$

$$\omega_2 = \sqrt{8 \cdot \frac{4.154 \cdot 10^{10}}{1.387 \cdot 10^7}} = 154.818\frac{rad}{s} \mathrel{\hat{=}} \underline{24.6Hz}$$

Comparing the results with those in Table 5-8, it can be seen that the first mode of the FE calculation fits the analytical result very well, whereas the second mode differs already about 36%. The reason is the very coarse number of only 3 degrees of freedom in the analytical model.

Simple FE calculation

To be able to calculate the previous model with more than 3 degrees of freedom quickly, ANSYS is used to set up a simple 1-D FE model, using the same values like used for the analytical calculation above. This calculation model is also required in in Chapter 7.1.2 to gain the additional spring stiffness by means of ANSYS.

Therefore three MASS21 elements (2-D masses with rotary inertia) are connected with COMBIN14 elements (1-D torsional spring-dampers). Their only degree of freedom is the rotation about their z-axis.

Using the same properties as for the analytical estimation before, the results are identical until the first decimal place:

$$\omega_1 = 17.4Hz$$
$$\omega_2 = 24.6Hz$$

Performing the same FE analysis with 7 rotary masses and appropriate spring stiffness, the first 3 modes approach the results of the full FE calculation with the solid stator core model very well (compared to Table 5-8 in the next chapter):

$$\omega_1 = 17.5Hz$$
$$\omega_2 = 38.4Hz$$
$$\omega_3 = 52.3Hz$$

Full FE calculation

Now as the rightness of the FE model is verified, modal analyses of all projects have been performed. Table 5-8 lists all mode frequencies between 0 Hz and 140 Hz, using the solid FE model of the stator core.

Table 5-8: Natural torsional frequencies of the free stator core

	Mode order (all values in Hz)							
Project	**1**	**2**	**3**	**4**	**5**	**6**	**7**	**8**
Mica	19.4	38.7	58.1	77.6	97.2	116.8	136.6	
Bad Creek	18.0	36.1	54.2	72.5	91.0	109.8	128.8	
SM3	17.0	33.9	51.0	68.1	85.4	102.9	120.5	138.4
THP	18.1	36.2	54.3	81.6	91.0	109.6	128.4	
NT2	24.6	49.2	74.1	99.3	124.9			
R2/R7	65.4	132.0						
Caruachi	25.0	50.0	75.3	100.9	126.9			
Caojie	40.2	80.6	121.4					
Lower Matt.	39.2	78.5	118.2					
Birkapili	38.1	76.3	114.8					

It can be seen that there are a lot of natural frequencies between 0 Hz and 140 Hz. Some of them are ever very close to the single- and double-grid frequency, which is disadvantageous in a fault case. (As mentioned, the excitation frequency in a case of failure is the single- and double-grid frequency). But these results are only valid for the free stator core, not attached to anything. In which way the frame will affect the natural frequencies, the following two chapters will show.

5.1.2 Natural Frequencies of the Core – Assuming a Massless, Infinite Stiff Stator Frame

By fixing all stator-to-frame connection nodes in tangential direction, a massless, infinite stiff stator frame is simulated (Figure 5-42). Due to increasing the tangential stiffness to infinite while keeping the mass constant, natural frequencies will increase to their maximal possible value of each specific project. The natural frequencies, with the real frame attached, will be somewhere in between these natural frequencies and the natural frequencies of the “free” core.

Note: In reality, the mass of the frame is very low compared to the core mass (see Table 4-5).

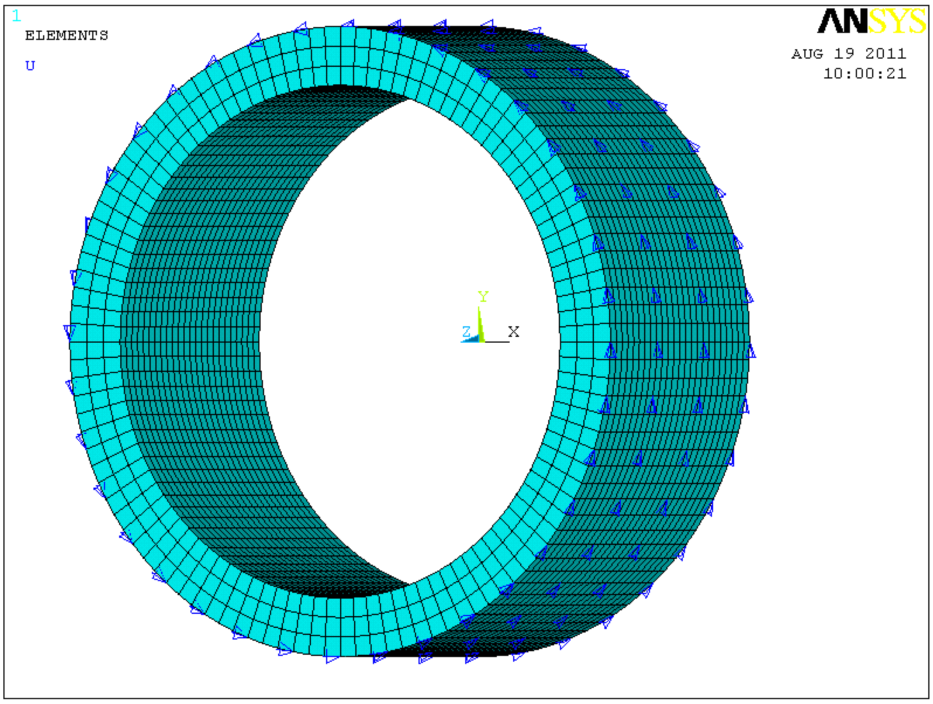

Figure 5-42: Core of "Birkapili" with BC (blue) simulating an infinite stiff frame

Table 5-9 shows the results of the modal analysis, where the stator core is attached to an infinite stiff frame. It can be seen that now all natural frequencies are higher than the single-frequency. The question arising now is: Is the stator frame heavy enough and its stiffness low enough to lower at least the first mode again, that a supercritical operation is possible? This is discussed in Chapter 5.2 later on.

Table 5-9: Natural torsional frequencies of the stator core attached to an infinite stiff frame

	Mode order (number of mode shape nodes)					
Project	**0**	**1**	**2**	**3**	**4**	**5**
Mica	113.6 Hz	113.8 Hz	114.4 Hz	115.2 Hz	116.0 Hz	116.6 Hz
Bad Creek	90.0 Hz	90.1 Hz	90.4 Hz	90.7 Hz	90.9 Hz	
SM3	101.1 Hz	101.2 Hz	101.6 Hz	102.0 Hz	102.4 Hz	102.7 Hz
THP	107.4 Hz	107.5 Hz	107.9 Hz	108.5 Hz	109.0 Hz	109.4 Hz
NT2	97.9 Hz	98.1 Hz	98.6 Hz	99.1 Hz		
R2/R7	130.7 Hz	131.3 Hz				
Caruachi	104.4 Hz	104.7 Hz	105.4 Hz	106.1 Hz		
Caojie	118.4 Hz	119.1 Hz	120.6 Hz			
Lower M.	116.5 Hz	116.9 Hz	117.8 Hz			
Birkapili	113.7 Hz	114.1 Hz	115.0 Hz			

Another interesting fact of Table 5-9 is that all natural frequencies between 0 and 140 Hz are in a very narrow range for each machine. The reason is that the shelves force a certain mode shape. This effect is explained with the help of an example in the next paragraph:

"NT2", for instance, has 5 shelves. These 5 shelves "force" the core to shape like it does in the case of the 4-noded natural frequency. The natural frequency of the 4-noded mode of the free core is (according to Table 5-8) 99.3 Hz. This means every mode with less or equal to 4 nodes is due to the 5 shelves forced to adopt a 4-noded shape. Hence the mode's frequency approaches also the value of the 4-noded mode (99.3 Hz). This phenomenon is illustrated in Figure 5-43. As mentioned, this is just possible for shapes with (in the case of "NT2") less equal 4 nodes in the modal analysis of the free core. Mode shapes with more than 4 nodes might have nodes "between" the shelves. These modes just increase their natural frequency value due to the higher stiffness, so that they are not in the range up to 140 Hz any more. (The 5^{th}-order mode of "NT2" (124.9 Hz) increases its frequency value above the calculated range from 0 to 140 Hz.) The conclusion derived from this knowledge is that the natural frequencies can be influenced by the amount of shelves (even if the global frame stiffness remains constant).

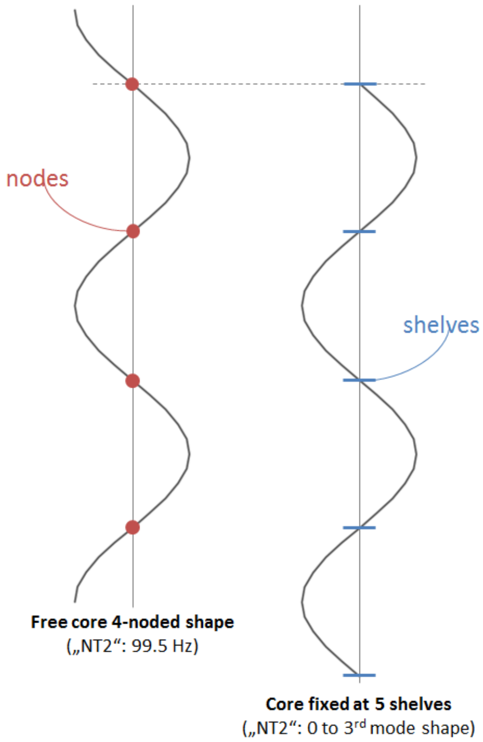

Figure 5-43: Illustration of the influence of the amount of shelves

The top image of Figure 5-44 shows the 4-noded mode shape of the free "NT2" stator core. The red dots illustrate the nodes for this shape. The bottom image is the fixed core and shows the actual 0-order shape (the shape with no nodes, which natural frequency was 0 Hz in the case of the free stator). The orange dots illustrate the 5 shelves.

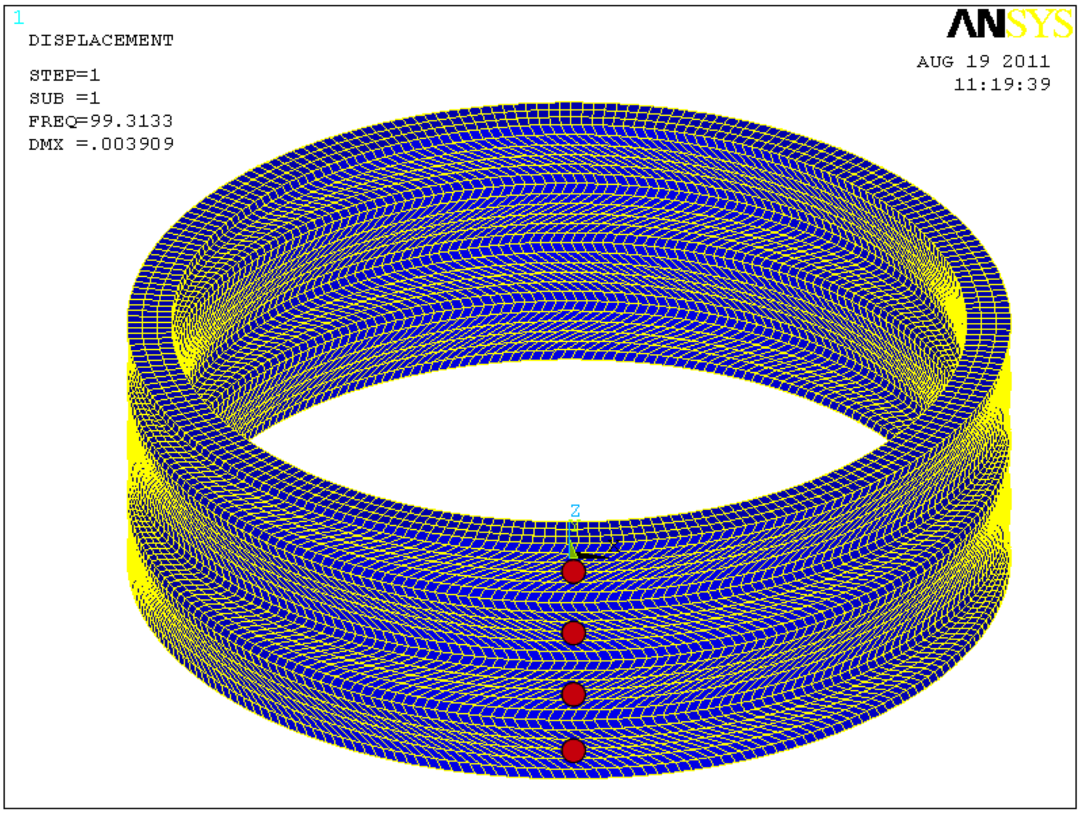

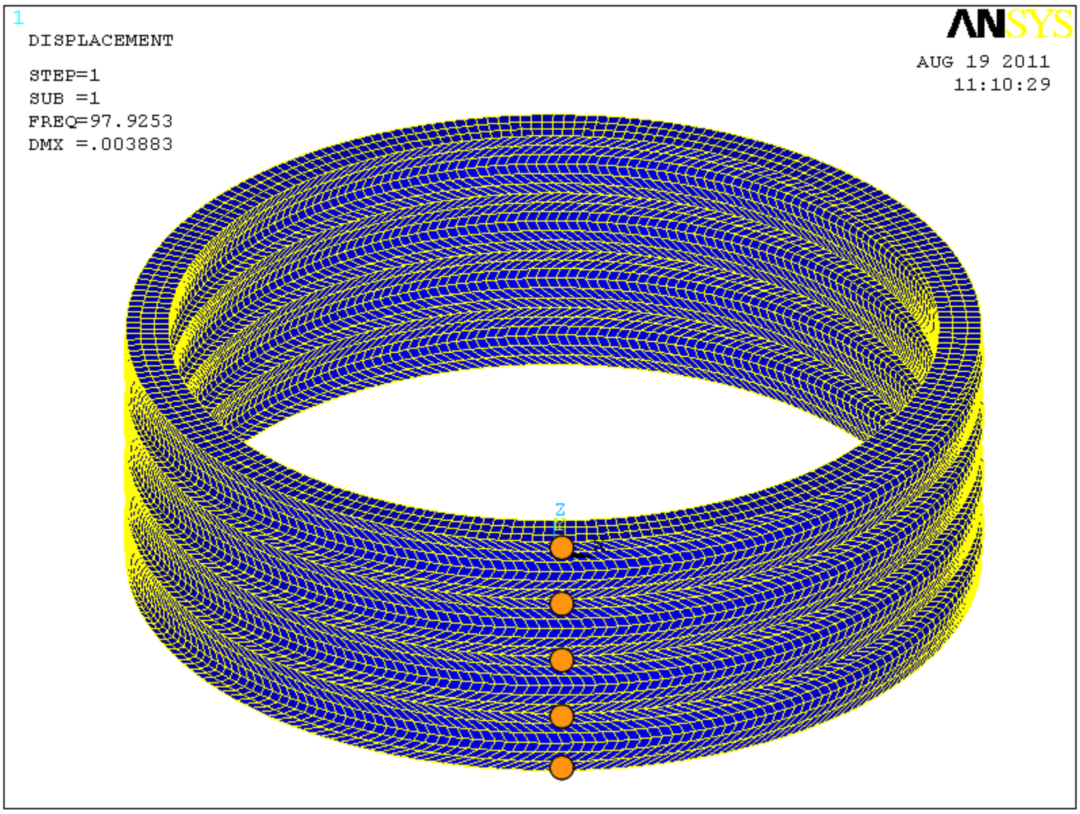

Figure 5-44: Core of "NT2", top: 4th-order mode of free core; bottom: 0-order mode of fixed core

The effect of the amount of shelves can be seen if projects “THP” and “Bad Creek” are compared. Both of them have a very similar mass, geometry (and consequently a similar stiffness) and very similar natural frequency values for their free core. But if their cores are connected to an infinitely stiff frame, their average mode frequency values of their first few modes differ vastly. (“THP” has 7 shelves and its 6th-order natural frequency of the free core is at 109.6 Hz; “Bad Creek” has 6 shelves and its 5th-order natural frequency of the free core is at 91.0 Hz.) This can be seen in Figure 5-45.

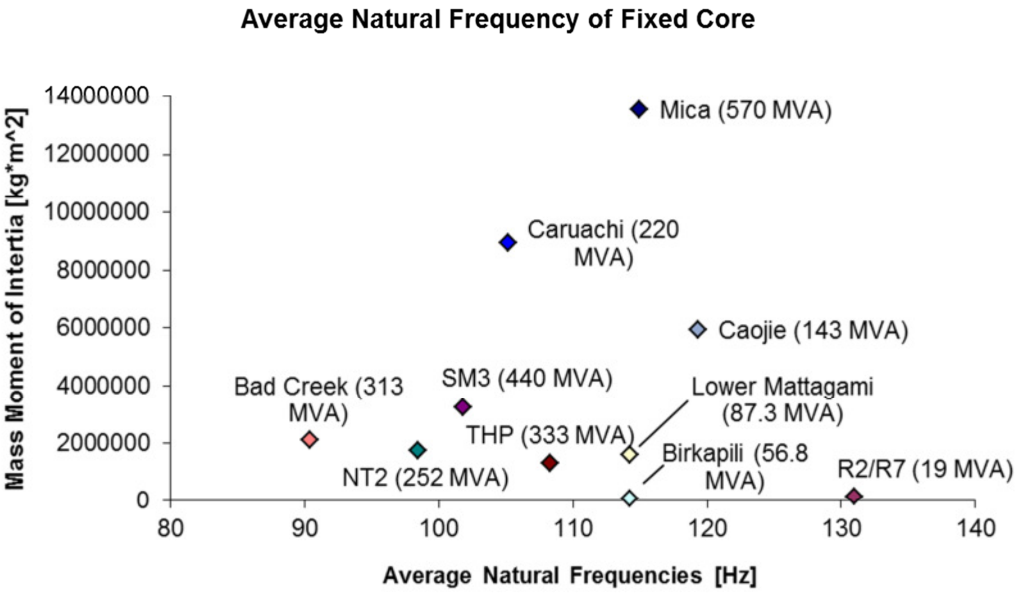

Figure 5-45: Average natural frequencies (between 0 and 140 Hz) by core inertia

Figure 5-45 was created to find a predictable correlation between the core dimension and its average natural frequency[8] between 0 Hz and 140 Hz. A tendency towards smaller mass moments of inertia for lower power ratings can be seen. But this is not very astonishing, as higher power ratings require a higher core mass and / or bigger dimensions. There is also a slight tendency towards higher natural frequencies for lower power ratings. This can be explained by the previous statement: Lower power rating causes → lower mass moment of inertia causes → higher natural frequency. But the variance is too high to find a solid trend which can be helpful for future project designs. Too many other parameters (like the number of shelves and the angular distance between two key bars) seem to influence the natural frequency.

[8] As all natural frequencies of one machine are in a tiny range of max. 3 Hz, an arithmetic average value with all of these frequencies is calculated to be able plot the results in a chart.

Also the radial thickness of the core (illustrated in Figure 5-46) seems to have a big influence on the natural frequency: “Mica” (radial core thickness: 0.57 m) and “SM3” (radial core thickness: 0.61 m) have both seven shelves. Even though “Mica” has a much higher mass moment of inertia than “SM3” (see Figure 5-45), its natural frequency is also higher. This contrariety can be explained with the lower radial core thickness of “Mica”, which makes the core more stiff in tangential direction.

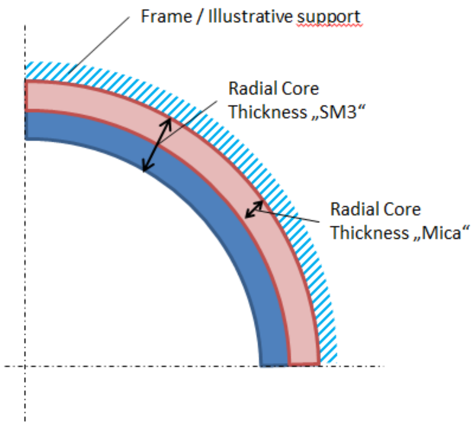

Figure 5-46: Radial core thickness of “Mica” and “SM3” (same outer diameter D_C for illustration reasons)

Anyhow, as mentioned, it can be seen in Table 5-9 that now all natural frequencies are higher than the single-frequency and a supercritical operation is not possible. The effect of the attached stator frame is discussed in the next chapter, where a modal analysis of the whole stator (core + frame) is performed.

5.2 Natural Frequencies of the Whole Stator

For this modal analysis, the FE model of the whole stator (Chapter 3.1) is used. The results can be seen in Table 5-10.

Table 5-10: Natural frequencies of the whole stator

Project	Single-frequ.	Mode orders (all values in Hz)						
		0	1	2	3	4	5	6
Mica	60	59.0	97.6	105.7	108.4	109.9	110.4	114.0
Bad Creek	60	53.9	81.1	86.0	88.7	90.4		
SM3	60	56.7	88.0	94.0	97.6	100.3	102.2	
THP	50	57.9	92.2	99.2	103.3	106.5	108.8	
NT2	50	67.6	89.7	94.8	98.1			
R2/R7	60	119.2	129.9					
Caruachi	60	72.9	93.5	97.6	100.0			
Caojie	50	92.8	110.8	118.2				
Lower Matt.	60	91.8	113.2	116.8				
Birkapili	50	93.2	109.3	113.3				

The previously mentioned effects (influence of shelves, radial core thickness and the mass – power output relation) can also be seen in Figure 5-47, in a less distinctive way though. Figure 5-47 is the same chart like Figure 5-45, with the only difference that now the real frame is attached to the core.

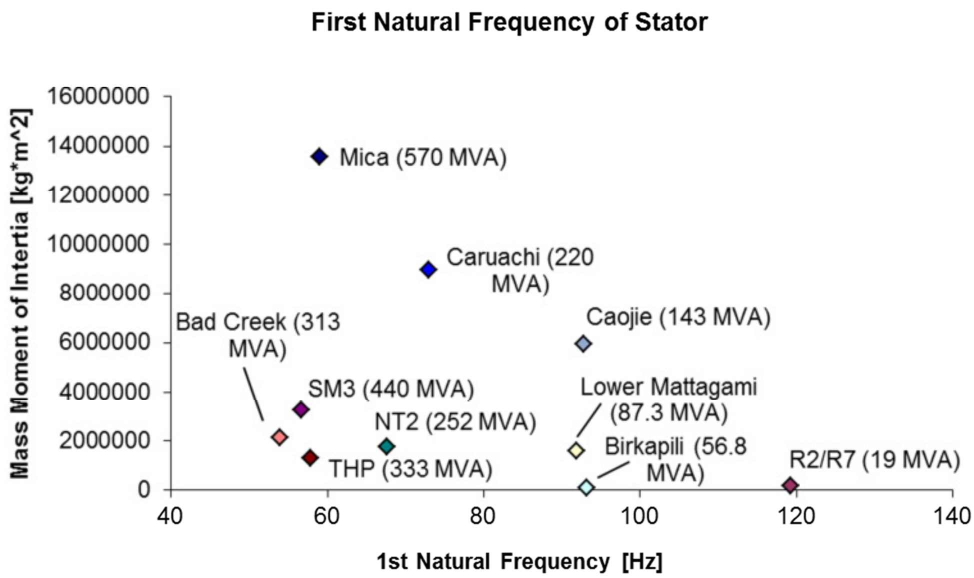

Figure 5-47: First mode frequencies of the whole stator (core with frame attached)

However, referring again to Table 5-10, the natural frequencies are, as expected, in between those of the free and the fixed stator core. But the initial expectations, that the first natural frequency of each stator is much lower than the excitation frequency, did not occur. Most of the natural frequencies are above the dominating single-frequency of excitation; some of them are even very close to this excitation frequency. Also these values which are below the single-frequency are probably not low enough to achieve a significant reaction force reduction in the soleplates.

Now the essential questions arising are: How big is the reaction force on the soleplates after a few excitation cycles, before the circuit breaker is activated. How quick does the vibration build up? How strong is the excitation force related to the stator mass? To answer these questions a transient vibration calculation is necessary.

6 Dynamic Behavior in a Case of Failure

To investigate the behavior of the complete stator in a fault case, a transient calculation is necessary. A transient calculation is necessary as the fault force occurs suddenly during regular operation (initial condition) and lasts only for a very few tenths of seconds. Furthermore the excitation force is transient, as consists of a single- and double-grid frequency and different decay rates. For the calculation the same FE model like in Chapter 5.2 is used.

At first some assumptions concerning the previously mentioned initial condition and the electrical faulty torque have to be made.

6.1 Assumptions

One of the assumptions of the equations, describing the faulty torque (Equation 1.3 in Chapter 1.2.3), is that at the beginning of the faulty torque force the current (and consequently the torque) is zero. But in reality the existent torque is $T_n = P/\omega$. Another electrical unknown factor is the phasing (the time) at which the faulty torques occur.

Summarized, the **problematic issues** are:

- The electrical torque equations are not exactly correct for occurring during operation.
- The phasing at the time when faulty torques occurs is unknown. (Essential for the line-to-line short circuit.)
- The faulty torque has a different value at the beginning (t=0) than the operational torque ($T_n \neq T_f(t=0)$). A point of discontinuity occurs.

Following **assumptions** are made:

- The faulty torque equations are assumed to be the same, independent whether there is torque or not.
- The worst case of phasing is assumed.
- The torque, acting on the stator until the faulty torque occurs, is *not* the operational torque, but the faulty torque: $T(t \leq 0) = T_f(t=0)$. (The effect of this assumption can be seen on Figure 6-49).

6.2 Modeling and Evaluation

6.2.1 Choosing the Time Step Size

When performing a transient analysis, discrete time points have to be set. At each time point a calculation is performed and results can be retrieved. How to set these time points primarily depends on the natural frequencies of the calculated body and the frequencies of the excitation forces. It is described in this chapter.

The term “time step size” (henceforth also called “time step” or abbreviated “TS”) is the time between two adjoined discrete chosen time points. At each time point a new calculation force value can be applied and a calculation takes place. Choosing an adequate time step size is very important in terms of the result’s accuracy. Too small time step sizes may cause a gratuitous long calculation and postprocessing time; too large time steps end up in wrong results. Not only because the calculation points are far apart from each other, but also because excitation frequencies might not be pictured properly.

To avoid this, the Nyquist-Shannon sampling theorem has to be regarded (equation 2.27). This results in a maximal allowable time between two time points of

$$\Delta t_{\max} = \frac{1}{2 \cdot f_{\max}} \tag{6.34}$$

In case of a compound of excitation frequencies, the highest occurring frequency must be used to calculate the maximal time step size.

For all following calculations a time step size of $t_{\max} = 1/(4 \cdot 140) = 0.001786s$ is used. It allows plotting the double-frequency (plus tolerance) of the excitation frequency. Also all natural frequencies up to 140 Hz (in the strict sense even up to 280 Hz) will be pictured properly.

The total number of time steps (the “length” of the calculation, thus the last calculated time point) is related to the lowermost frequency in a compound of frequencies. In this case, the lowermost appearing frequency is the single-frequency of 50 Hz. This means the last calculated time is $t_{End} = 1/50 = 0.02s$. After 0.02 s 1 period of a 50 Hz frequency and approximately 11 periods of a 140 Hz frequency are over. But as those fault forces are 2 to 3 periods alive, and excited reaction frequencies can be lower than 50 Hz, the end time is set to $t_{End} = 2.5/50 = 0.05s$.

Some models have a large number of nodes. To reduce calculation time, all transient calculations have just in radial and tangential direction degrees of freedom. Deviations in results are negligible.

6.2.2 Applying the Faulty Torque

The faulty torque is applied homogenously as tangential force on the nodes at the inner radius of the stator core. How this is done exactly is explained in Chapter 6.5.1 (subchapter "Applied forces", page 77). Even though this detailed explanation is done on the basis of a one-quarter model, it is still valid in general.

The equations of the faulty torque are initially inputted into ANSYS, whereas the parameter "t" remains variable in these equations. For each time step the faulty torque value is calculated (with the appropriate time value "t") and reassigned to the force vectors on the model.

6.2.3 Evaluating the Soleplate Forces and Plotting the Results

It is expected that the reaction force spreads equally on all soleplates. This allows evaluating the reaction forces of just one soleplate after the analysis.

To get the total soleplate reaction force, the reaction forces of all soleplate nodes are simply summed up:

$$F_{SP} = \sum_{i=1}^{n_{SPN}} F_{SPN\_i}$$

Referring to Figure 6-48, where the boundary conditions at the soleplate nodes (numbered) can be seen, the total reaction force for one time step is:

$$F_{SP} = \sum_{i=1}^{4} F_{SPN\_i} = F_{SPN\_1} + F_{SPN\_2} + F_{SPN\_3} + F_{SPN\_4}$$

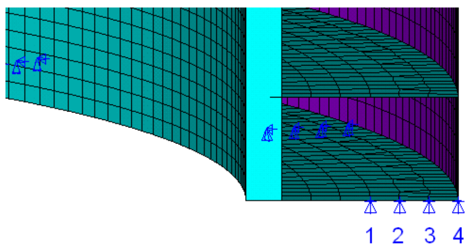

Figure 6-48: Boundary conditions simulating soleplates (show through elements)

To be able to represent the excitation torque together with the soleplate reaction forces in the same chart, the **excitation torque is plotted as soleplate reaction force** with no mass effects. It is comparable to a static calculation for each time step. As the basic mechanical system is very simple (homogenously applied torque, periodical soleplate distribution) the reaction force of one single soleplate is

$$F_{SP\_Static}(t) = \sum_{i=1}^{n_{SPN}} \frac{T_f(t)}{r_{SPN\_i} * n_{SP} * n_{SPN}} \tag{6.35}$$

r_{SPN_i} .... Radial location of the appropriate soleplate node n [m]

Referring to Figure 6-48, the total reaction force for one time step t_1 is:

$$F_{SP\_Static}(t_1) = \frac{T_f(t_1)}{n_{SP} \cdot 4} \cdot \left(\frac{1}{r_1} + \frac{1}{r_2} + \frac{1}{r_3} + \frac{1}{r_4} \right)$$

That’s why the **excitation torque is named “static soleplate reaction”** in most of the charts. This is technically not totally correct, as the excitation torque / reaction force appears to be dynamic, but it is based on a static calculation for each time step.

6.3 Example Calculation for "Mica"

This chapter shows for explanation reasons an example calculation with the help of machine "Mica", like it is performed for every other machine. All results can be found in Chapter 6.4.

The first step is to retrieve the torque in case of a 3-phase short circuit:
Inserting the appropriate electrical values in the equations shown in Chapter 1.2.3, the torque force of a 3-phase short circuit is:

$$T_{f\_stat} = 0.0658 \cdot e^{-\frac{t}{0.1534}} + 3.419 \cdot 10^{-3} \cdot e^{-\frac{t}{0.0295}} + 0.0107 \cdot e^{-\frac{t}{1.9583}} + 0.0121 \cdot e^{-\frac{t}{0.0580}}$$

$$+ 5.028 \cdot 10^{-3} \cdot e^{-\frac{t}{0.0589}} + 8.911 \cdot 10^{-3} \cdot e^{-\frac{t}{3.9167}} + 1.849 \cdot 10^{-3} = 0.107807\Big|_{t=0}$$

$$T_{f\_\omega} = 1.4355 \cdot e^{-\frac{t}{0.0494}} + 2.5441 \cdot e^{-\frac{t}{0.2845}} + 1.0556 \cdot e^{-\frac{t}{0.3068}} = 5.0352\Big|_{t=0}$$

$$T_{f\_2\omega} = 0.1792 \cdot e^{-\frac{t}{0.1534}} = 0.1792\Big|_{t=0}$$

$$T_f = 36740.92 \cdot 10^3 \cdot \left(T_{f\_stat} + T_{f\_\omega} \cdot \sin(\omega \cdot t) + T_{f\_2\omega} \cdot \sin(2\omega \cdot t)\right)$$

The initial condition problem, explained in Chapter 6.1 before, can be seen for the time t=0:

$$T_f(t=0) = 36740.92 \cdot 10^3 \cdot (0.107807 + 5.0352 \cdot \sin(0) + 0.1792 \cdot \sin(0)) = 3960.93 \cdot 10^3\ Nm$$

$$T_n = \frac{P}{\omega} = \frac{570 \cdot 10^6 \cdot 0.9}{\frac{133.3}{60} \cdot 2\pi} = \underline{36740.92 \cdot 10^3\ Nm \neq 3960.93 \cdot 10^3\ Nm}$$

The operational torque and the faulty torque at the very beginning are not identical. The resulting effects of the assumption (initial condition is the faulty torque, not the nominal torque) made in Chapter 6.1 can be seen on the chart below:

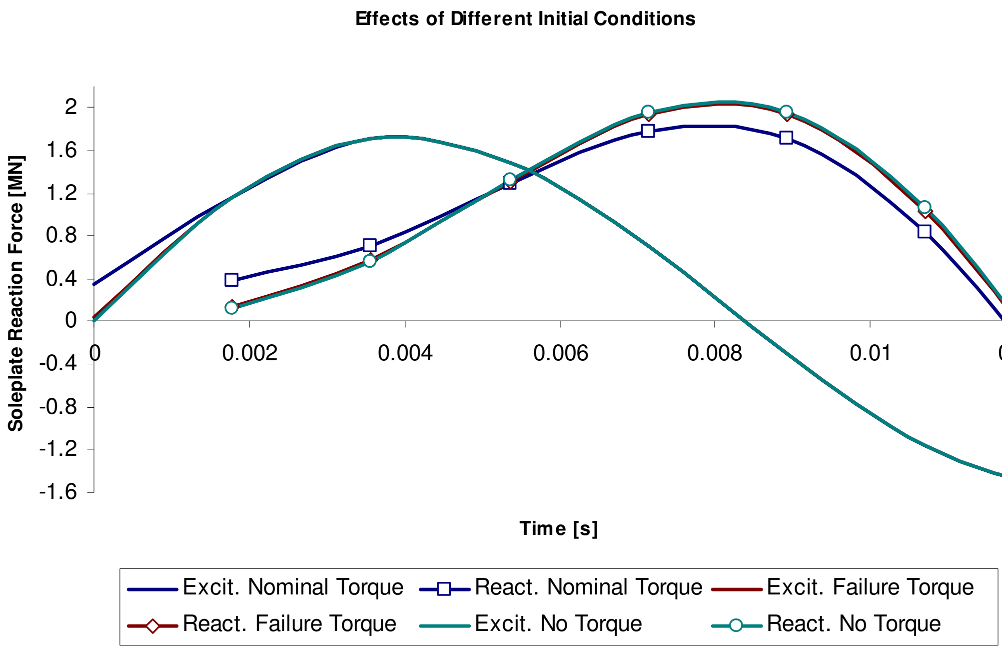

Figure 6-49: Effects of different initial conditions

How the chart in Figure 6-49 is created and to be read is explained later in a more detailed way. The curves starting at t=0 are the curves of the excitation force. The curves starting further to the right (at t=0.001786 s) represent the reaction force of one soleplate. The single time steps are indicated by the squares, diamonds and circles on the reaction curves. At time t=0 the different initial conditions can be seen. The green curve shows the excitation force with no initial condition (no force applied). The associated curve, representing the reaction, is the green line with the circular shaped time step points, starting at t=0.001786 s. The brown line is the excitation force with the initial force of the calculated failure torque at t=0. The force is relatively small. Hence this curve is pretty much congruent with the green one. The initial condition represented by the blue line is this one with the operational torque at the beginning. The associated reaction force curve is again the blue one with the square shaped time step points. Even though the blue line has a much higher initial value, the peak value of the reaction is a little lower compared to the brown line. Considering that every time steps, since t≥0.001786 s, are the same for all excitation curves, the brown curve experiences (mathematically) a much higher acceleration than that of the blue curve. (The brown curve has to overcome a higher force difference in the same amount of time compared to the blue curve. Therefore a higher acceleration is needed / calculated, which acts on the stator and affects the reaction curve.) This higher acceleration has an impact on the peak value of the reaction force.

Figure 6-50 shows the final result of the transient calculation of a 3-phase short circuit of “Mica”. The reaction force of one single soleplate is plotted.

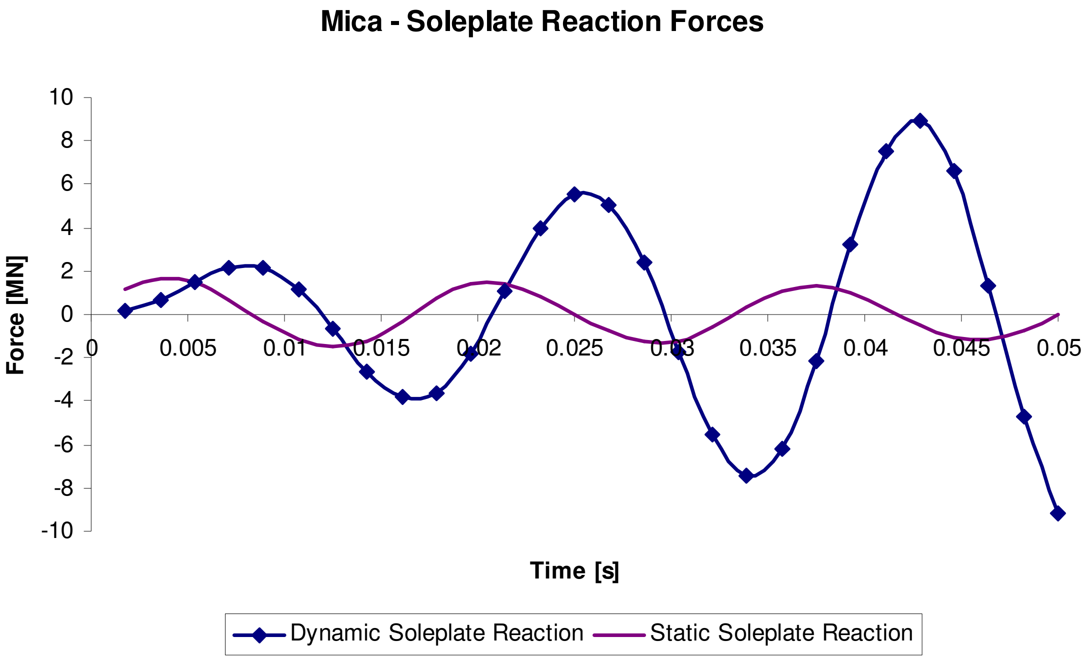

Figure 6-50: Reaction force of one Soleplate of “Mica”

The dark purple line is the for each time step calculated “static” reaction of one soleplate (see Equation 6.35). This curve represents the excitation force due to the electrical fault, downscaled to a soleplate reaction without regarding mass effects. Its peak value is the value used for the soleplate layout so far. The blue line is the transient response and its diamond shaped dots are the time steps. The initial condition at t=0 is not shown.

The shape of the reaction curve shows that there is no force reduction like initially expected. What happens is quite the contrary: The reaction force builds up very quickly. But this is not really astonishing, as the first natural frequency of “Mica” is very close to 60 Hz.

6.4 Results of Related Projects in Case of a 3-Phase Short Circuit

On the basis of the charts on the following pages (Figure 6-51 to Figure 6-56) it can be seen that the built up of the reaction force is very significant, even for machines which natural frequencies that are relatively far away from the single-frequency. “Mica” shows in this chart a relatively homogenous build-up with its absolute peak value at the end of the excitation. “Caruachi”, “THP” and “SM3” have similar characteristics with a peak value of

4.59 to 5.49 times the static reaction. (As mentioned, the term “static reaction” (purple line in subsequent charts) describes in this case the soleplate reaction force in case of a failure without regarding dynamic effects.) In contrast “Birkapili” and “R2R7”, which are all 50 Hz machines, have a peak value of only 2.34 to 2.60 times the static reaction. Furthermore the peak value is already reached within the first excitation cycle and doesn’t change significantly afterwards.

In the following table, the peak value of the reaction force within the first 0.05 seconds is listed. The static value (F_{static}) refers to the reaction where no mass, spring or damping effect is regarded (deep purple line in the following charts). The dynamic value ($F_{dynamic}$) is the peak value of the transient soleplate reaction (blue line in the following charts). As mentioned, the static peak value (plus safety factors) is nowadays used for designing the soleplate and the foundation.

Table 6-11: Peak reaction values of one soleplate in case of a 3-phase short circuit

Project	F_{static} [MN]	$F_{dynamic}$ [MN]	Build up factor [-]
Mica	1.661	9.114	5.49
SM3	1.519	7.378	4.86
THP	1.244	6.795	5.46
R2/R7	0.223	0.579	2.60
Caruachi	0.986	4.530	4.59
Birkapili	0.349	0.815	2.34

The number of reference projects has been reduced, as the difference of dynamic behavior among these projects is not as big as initially expected. The remaining 6 projects were chosen, because of their big differences in terms of their dimensions and output power.

Charts of the reaction force in case of a 3-phase short circuit

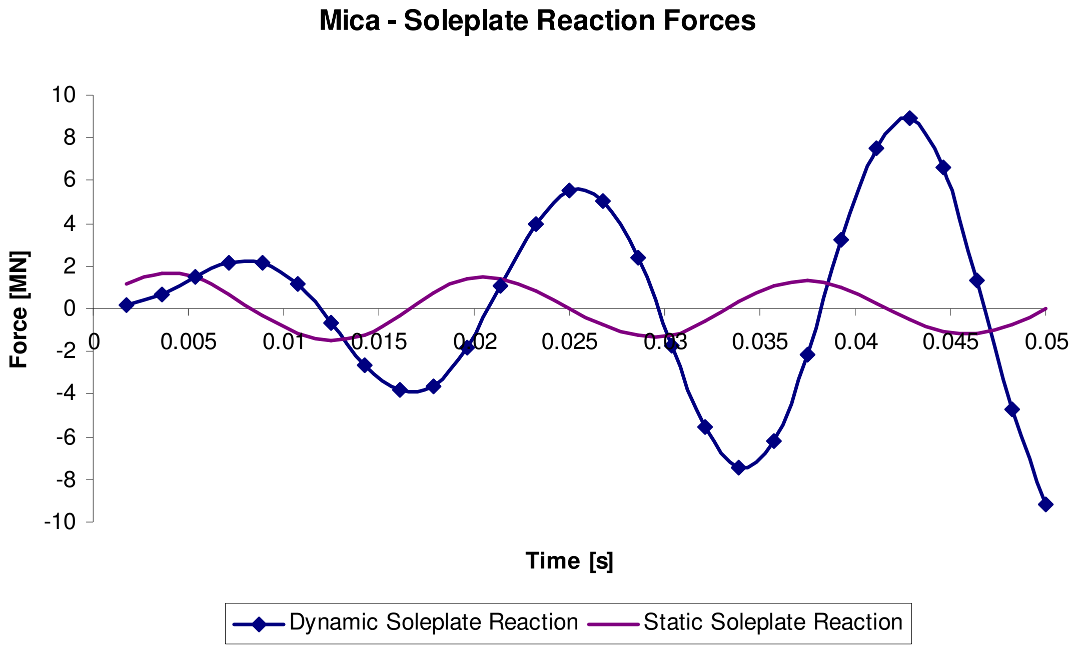

Figure 6-51: Soleplate reaction force of "Mica" in case of a 3-phase short circuit

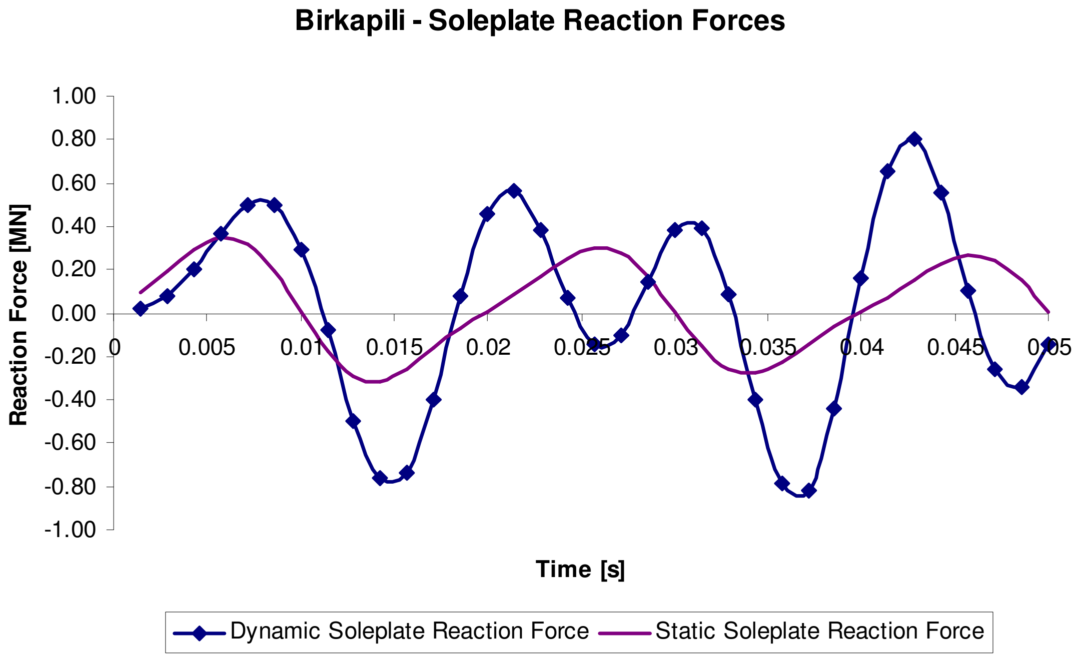

Figure 6-52: Soleplate reaction force of "Birkapili" in case of a 3-phase short circuit

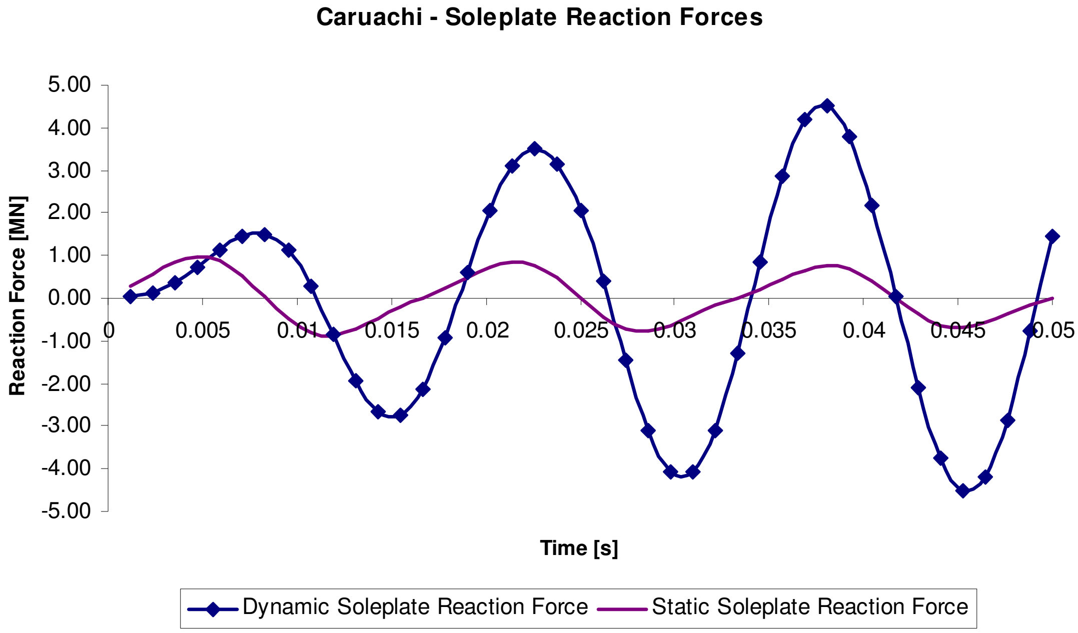

Figure 6-53: Soleplate reaction force of "Caruachi" in case of a 3-phase short circuit

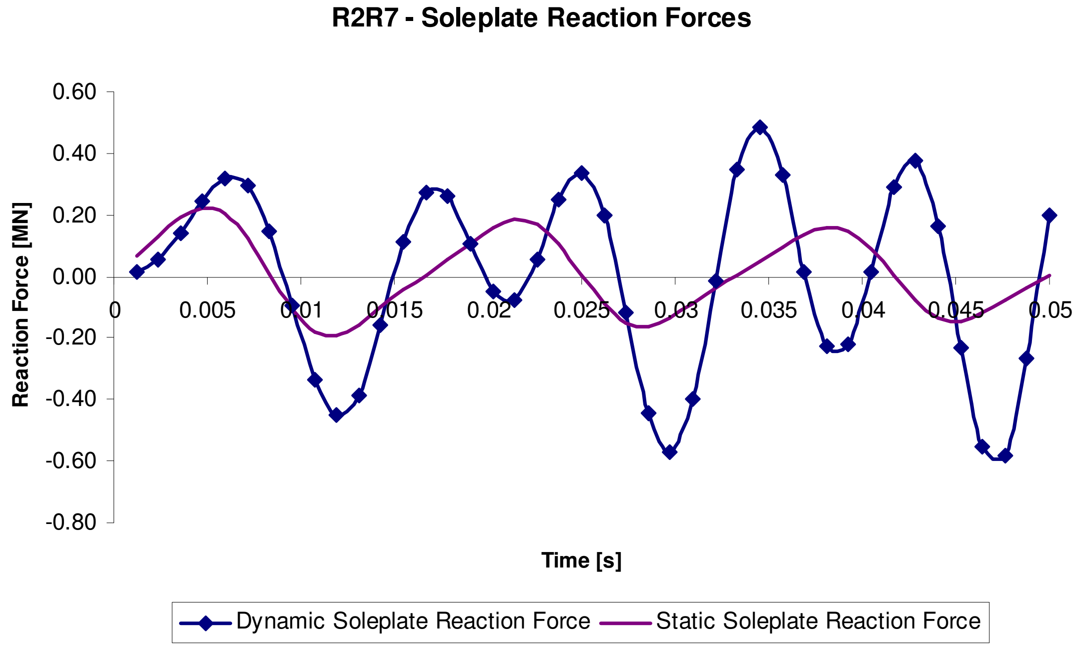

Figure 6-54: Soleplate reaction force of "R2R7" in case of a 3-phase short circuit

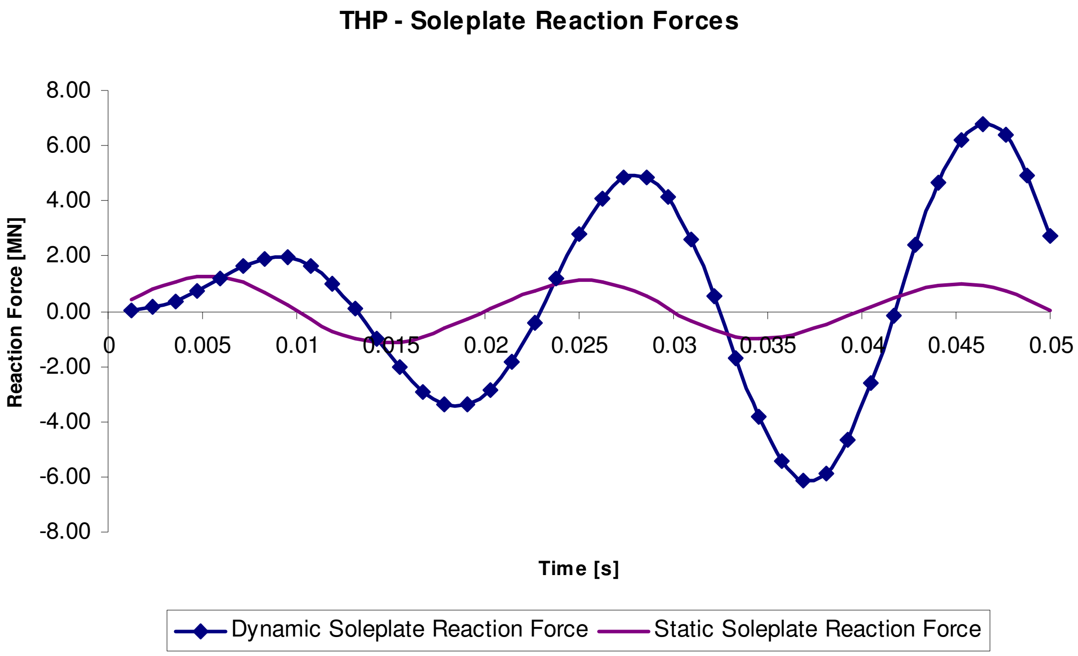

Figure 6-55: Soleplate reaction force of "THP" in case of a 3-phase short circuit

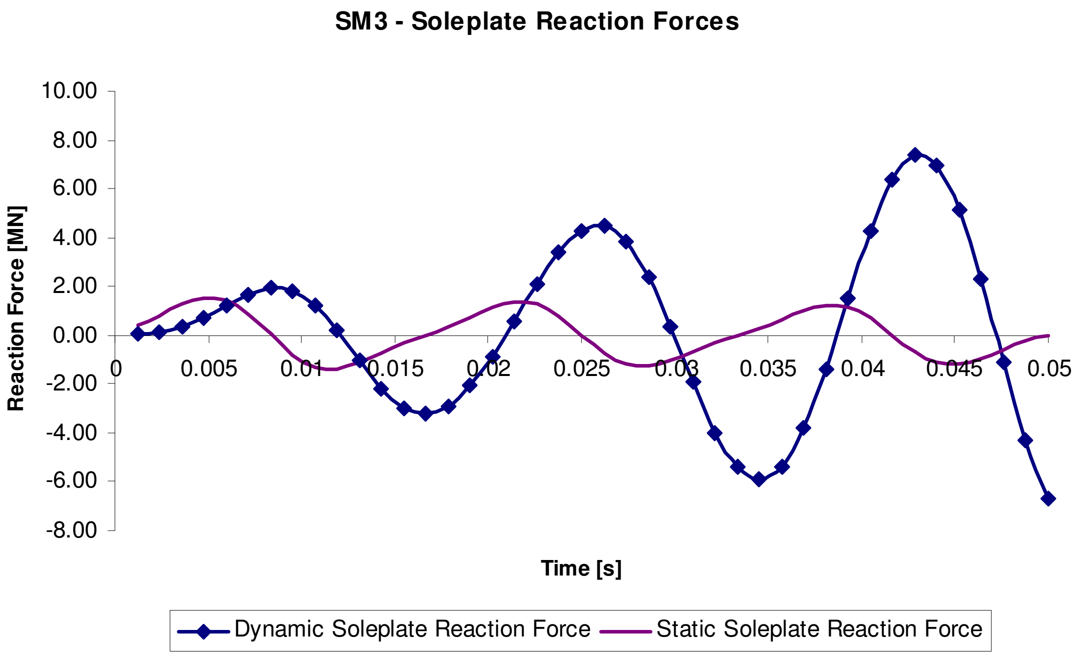

Figure 6-56: Soleplate reaction force of "SM3" in case of a 3-phase short circuit

6.5 Comparing the Simple Model with a Solid Model

All previous FE calculations are based on a very abstracted model of the stator. As the results are quite alarming, a solid CAD model (shown in Figure 6-57) of the project "Mica" has been calculated in this chapter, to quantify the difference between the simplified and the real, solid model.

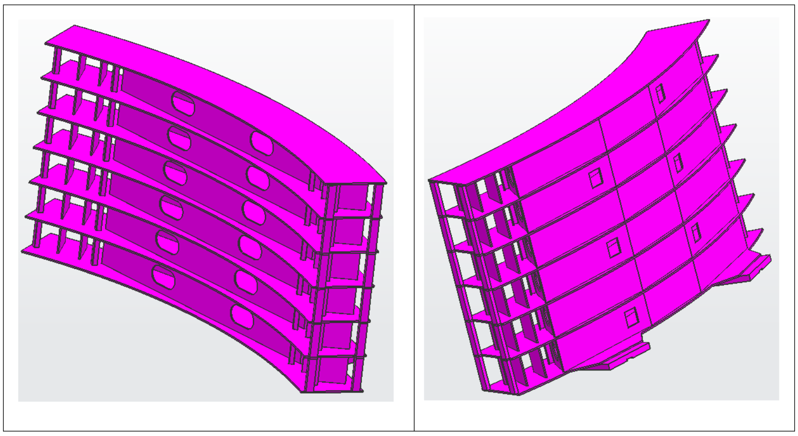

Figure 6-57: CAD model of "Mica" with eliminated details

The major problem which was faced when performing calculations with a solid CAD model is the high amount of degrees of freedom. The stator diameter of "Mica" is more than 13 meters, but sheets' thicknesses remain relatively small. This causes a very high amount of nodes, to keep appropriate aspect ratios of elements. Therefore, the following steps have been considered, to establish a calculation in an acceptable time on available computer systems:

- All details, such as chamfers, roundings, notches, bores, very thin and structurally not essential features, have been removed from the CAD model.
- To use symmetry effects, only a quarter of the stator is calculated.[9]
- Except at the core-to-frame connection area, an element size of approximately 5 cm is used.
- The node's only degree of freedom is in tangential direction.

The latter simplification has been verified by a static analysis. Therefore two analyses have been performed: one where the element nodes have all three degrees of freedom, and the second one where the nodes just have one (tangential) degree of freedom. The results,

[9] The imported CAD model is even just a 1/8 model and is enlarged to a quarter model in ANSYS.

which don't differ a lot, can be seen in Figure 6-58. The influence on the dynamic behavior (natural frequencies) is discussed in Chapter 6.5.2.

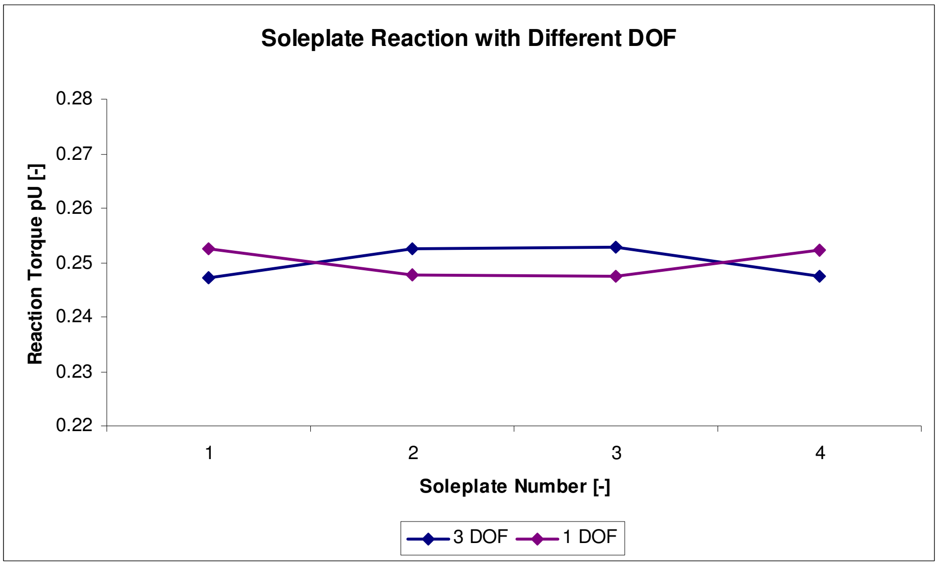

Figure 6-58: Influence onto the soleplate reaction with different degrees of freedom

The ordinate of Figure 6-58 plots the per-unit reaction torque of the excitation torque. On the abscissa the four soleplates of the quarter model are plotted, ordered ascending by their tangential position.

6.5.1 Special Treatments of a Quarter Model

Boundary Conditions

A torque acting on the surface of a cylindrical structure is antisymmetric. To achieve this, the quarter model is fixed in radial direction at its symmetry plane. The effect of this antisymmetric boundary condition is illustrated in Figure 6-59.

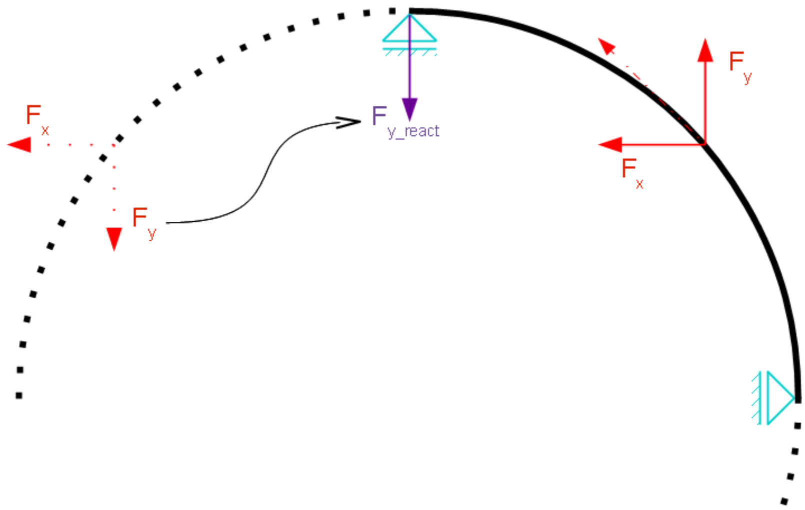

Figure 6-59: Illustration of an antisymmetric boundary condition on a circle with torque force

Applied Forces

The torque on the inner surface of the stator core is a homogenous force. The best way would be to apply the force as shear force, which is not possible in ANSYS. So the total torque must be distributed on all nodes as nodal force, regarding also their area of influence. Figure 6-60 shows for illustration a plane 3x3 mesh (black lines with turquoise colored background) with its nodes (red, orange and violet colored). The hatching indicates each node's area of influence.

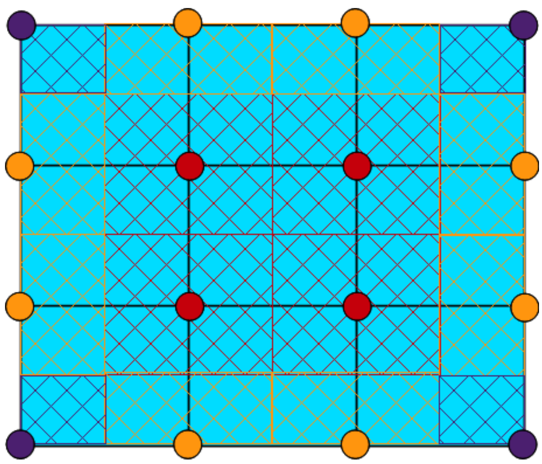

Figure 6-60: Distribution of a homogenous force (i.e. pressure) on the nodes of a 3x3 mesh

As mentioned, depending on the location of the node, each node as a different element surface to "act on". For example, a node on a body's corner is acting on just one quarter of

the element surface area compared to a node in the center of a body. Now to calculate each nodal force, based on the total torque, following calculation has been done:
Calculating total force acting on the inner core surface by means of the fault torque:

$$F_f = \frac{T_f}{r_C}$$

Calculating a general force per node, based on the fact that the sum of all nodal forces has to be F_f. (only ¼ of the fault torque is required, as only a quarter section of the stator is calculated):

$$F_{nodal} = \frac{\frac{F_f}{4}}{n_{Center} + \frac{n_{Edge}}{2} + 1}$$

Now the nodal force of corner nodes, nodes on an edge and nodes in in center can be calculated:

$$F_{Center} = F_{nodal}$$

$$F_{Edge} = \frac{F_{nodal}}{2}$$

$$F_{Corner} = \frac{F_{nodal}}{4}$$

F_f	Total fault force acting homogenously on the body [N]
n_{Center}	Amount of nodes in the center (red colored) [--]
n_{Edge}	Amount of nodes on edges, excluding corner nodes (orange colored) [--]
F_{Center}	Force applied onto each center node [N]
F_{Edge}	Force applied onto each edge node [N]
F_{Corner}	Force applied onto each corner node [N]

In case of a full cylindrical stator, used in the chapters before, the general nodal force is

$$F_{nodal} = \frac{F_f}{n_{Center} + \frac{n_{Edge}}{2}}$$

because of the nonexistent corner nodes (no "+1" in the denominator) and the distribution along the whole core circumference (no division of F_f by 4).

6.5.2 Natural Frequencies and Transient Response

Table 6-12 shows the results of the modal analysis. Compared to the simplified FE model, the solid model has slightly higher natural frequencies. But regarding the high degree of abstraction of the simplified model, the deviations are in an acceptable range. But this also means that the behavior in a failure case won't change significantly. The results of the transient calculation are plotted in Figure 6-61.

Table 6-12: Natural frequencies of the real model

	Mode order (all values in Hz)					
Project	**0**	**1**	**2**	**3**	**4**	**5**
Mica	69.5	107.2	115.2	120.3	124.3	127.1
Mica *	?	105.8	114.3	119.7	?	?

*) As mentioned, all previous dynamic FE calculations have been performed with only one degree of freedom (in tangential direction). To verify the accuracy, these values in Table 6-12 are the results from a modal analysis (range: 105 Hz to 121 Hz) with two degrees of freedom (tangential and radial) for each node. It can be seen that the influence is very low, as it is for all previous calculations with the simplified model.

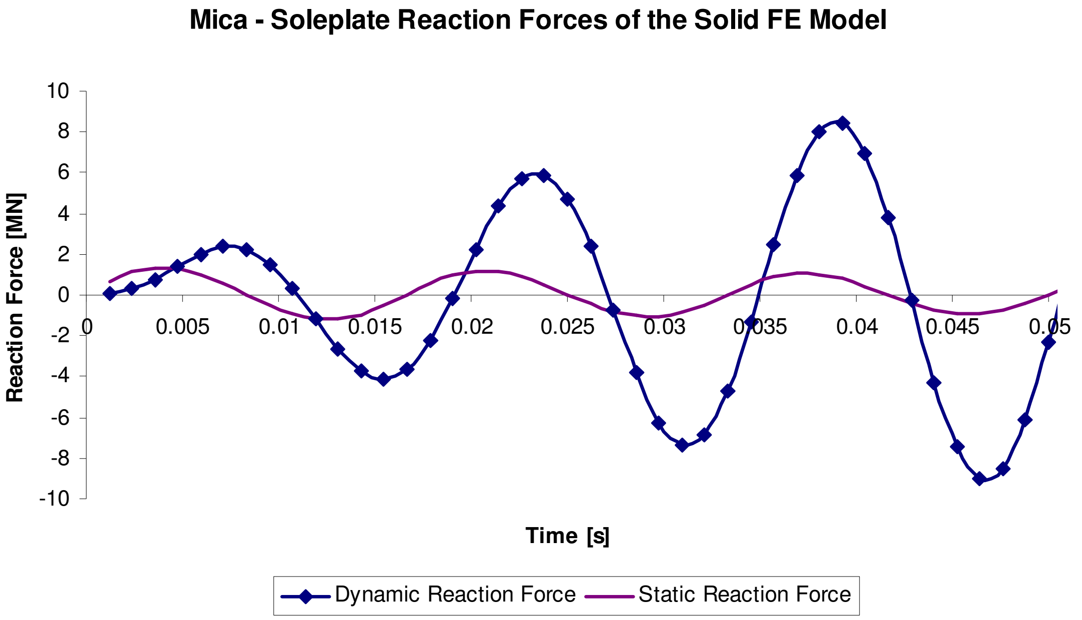

Figure 6-61: Soleplate reaction forces of "Mica" (CAD model)

Referring to Figure 6-61, the peak reaction value is, due to the higher natural frequency, slightly below the peak reaction value of the simple FE model (Figure 6-51). The small difference in the static reaction force is caused by the location of the soleplate. As mentioned, the soleplates at the simplified FE model are located on a smaller radius than they are actually. Consequently, higher reaction forces occur at the soleplates of the simple FE model.

6.6 Conclusion

Regarding the time-transient effects, the soleplate reaction forces are significantly higher than currently used in the design calculations of the stator structure.

Some older machines have been tested by short circuiting them on purpose (applying a sudden short circuit of the 3 phases). All of them survived the test without damage. A modal analysis has shown that also some of those old, tested machines have a natural frequency close to 60 Hz.[10] Why did they not break, even though they seem to be undersized?

An explanation might be the tangential clearance (d_c ~ 0.7 mm) between the stator core and the key bars which was not regarded in one of the previous calculations. If the sinusoidal

[10] Simplified FE models of the short circuit-tested projects "Guavio" and "Brisay" have been used for this modal analysis.

excitation force changes its sign before the stator core gets in contact with the key bar, not as much energy is transferred to the soleplates as in case of a rigid core-to-frame connection.

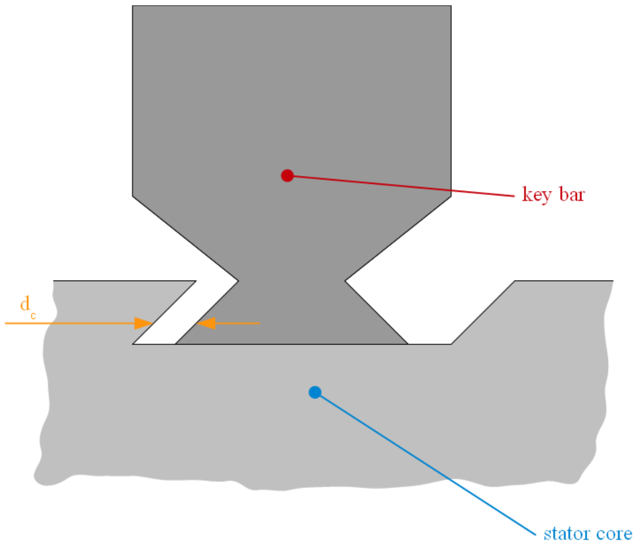

Figure 6-62: Tangential clearance between stator core and key bar

An example calculation is done with the values of the project "Mica":

$$m_C = 300527 kg$$

$$\Theta_C = 1.38657 \cdot 10^7 \, kg \cdot m^2$$

$$T_f(t) \approx 36.74 \cdot 10^6 \cdot (0.1 + 5 \cdot \sin(\omega \cdot t) + 0.2 \cdot \sin(2 \cdot \omega \cdot t))$$

$$\omega = 2 \cdot \pi \cdot 60$$

$$\varphi_{\max} = \frac{d_c}{R_C} = \frac{0.7 \cdot 10^{-3}}{6.935} = 0.101 \cdot 10^{-3} \, rad$$

θ_C	Core's mass moment of inertia [kgm^2]
φ_{max}	Clearance [rad]

$$T(t) = \Theta \cdot \ddot{\varphi}$$

$$\Theta \cdot \dot{\varphi} + C_1 = \int T(t) \cdot dt = 36.74 \cdot 10^6 \cdot \left(0.1 \cdot t - \frac{5}{\omega} \cdot \cos(\omega \cdot t) - \frac{0.2}{2 \cdot \omega} \cdot \cos(2 \cdot \omega \cdot t) \right)$$

with

$$\dot{\varphi}(t=0)=0$$

$$\Rightarrow C_1 = 36.74\cdot 10^6 \cdot \left(-\frac{5}{\omega}-\frac{0.2}{2\cdot\omega}\right) = 36.74\cdot 10^6 \cdot \left(-\frac{5.1}{\omega}\right)$$

$$\Theta\cdot\varphi + C_1\cdot t + C_2 = \int 36.74\cdot 10^6 \cdot \left(0.1\cdot t - \frac{5}{\omega} * \cos(\omega\cdot t) - \frac{0.2}{2\cdot\omega}\cdot\cos(2\cdot\omega\cdot t)\right)\cdot dt$$

$$\Theta\cdot\varphi + C_1\cdot t + C_2 = 36.74\cdot 10^6 \cdot \left(0.1\cdot\frac{t^2}{2} - \frac{5}{\omega^2}\cdot\sin(\omega\cdot t) - \frac{0.2}{4\cdot\omega^2}\cdot\sin(2\cdot\omega\cdot t)\right)$$

with

$$\varphi(t=0)=0$$

$$\Rightarrow C_2 = 0$$

Now the time “t”, when the stator core rotates about 0.101E-3 rad and finally gets in contact with the key bar, can be calculated:

$$\varphi(t) = 0.101\cdot 10^{-3} = \frac{36.74\cdot 10^6}{1.38657\cdot 10^7}\cdot\left(\frac{5.1}{\omega}\cdot t + 0.1\cdot\frac{t^2}{2} - \frac{5}{\omega^2}\cdot\sin(\omega\cdot t) - \frac{0.2}{4\cdot\omega^2}\cdot\sin(2\cdot\omega\cdot t)\right) \qquad (6.36)$$

$$\Rightarrow t = 0.005133s$$

The time of a 60 Hz oscillation period (which dominates the faulty torque) is 0.01667 s. This shows that the core of “Mica” gets in contact before the excitation torque changes its sign. So no significant reduction of the soleplate force can be expected. Chapter 6.7 takes a closer look on this issue.

However, the short circuit tested machine “Guavio” (which is not in the list of the reference projects) has, as mentioned, a similar first mode frequency like “Mica” and has survived the test without any damage. The same calculation shows that also the core of “Guavio” gets in tangential contact with the frame before the excitation torque changes its sign (contact after t=0.001381 s). So the core’s mass inertia is not an explanation why there was no damage.

Also the structural damping is too low to cause any major differences. Tests of Andritz Hydro's turbine division has shown that $\delta/\delta_{krit} \approx 0.00001$. The reason why "Guavio" survived the test may be a combination of following unsteadiness:

- The real natural frequency differs from the calculated one, due to
  - abstraction of calculation model,
  - stiffness deviations at joints,
  - insecure stator core properties and
  - friction and gap effects at the core-to-frame connection (see Chapter 6.7).
- The excitation torque was not as high as calculated.
- The structural capability was much higher than expected.
- Occurrence of yielding may be possible.
- Safety factors are high enough.

6.7 Influence of the Core-to-Frame Connection

Even though the calculation on the previous pages have shown that the gap d_C closes before the sinusoidal excitation force changes its sign, this chapter has a closer look on this non-linear core-to-frame connection.

The connection between stator core and stator frame is not rigid, as it is assumed in all previous FE calculations. The difference between a rigid core-to-frame connection and the real connection might be large. In this chapter this connection is regarded in a more detailed way to quantify the effect on the calculation results.

6.7.1 Simplifications and Assumptions

Before the generator reaches its operational temperature ("cold condition"), the stator core is radially not in contact with the key bars. (This is done to avoid high stresses in the stator core.) Due to the core's thermal expansion while reaching operational temperature ("warm condition"), it is pressing frontally against the key bars, like it can be seen in Figure 6-63.

The resulting friction force in tangential direction is very low compared to the torque, even during normal operation conditions. The consequence is that the gap between the core and key bar is permanently closed from the time the generator is powered up. The calculation model doesn't regard this fact. Hence there is also no initial deformation.

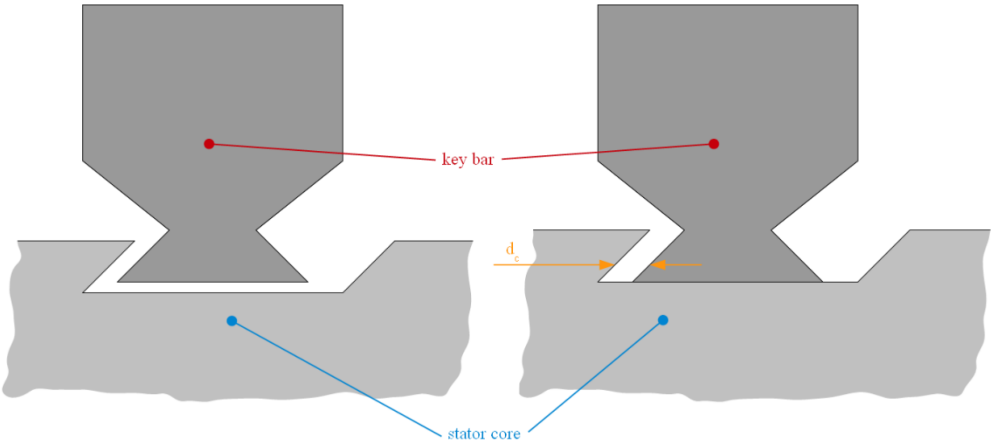

Figure 6-63: Core-to-frame connection in cold condition (left) and warm condition (right)

It is desired that the core can expand radially without any resistance as far as possible, not to have to high stress in the core. When the core gets in contact with the key bar, most of the thermal expansion process is finished. This causes also a relative low radial pressure on the dovetail bar's front. Consequently is also the tangential friction force between core and dovetail bar is relative low; it is much lower than the operational torque. This means that the gap is closed on one side all the time – even during usual operation.

Summarized, the assumptions / simplifications for the calculation model are:

- The tangential friction force is negligible small compared to the operational and faulty torque. So it is disregarded in all calculations.
- During usual operation the gap is closed on one side. The calculation model assumes that the initial position of the key bar is in the center of the key bar slot.

The assumptions / simplifications are illustrated in Figure 6-64.

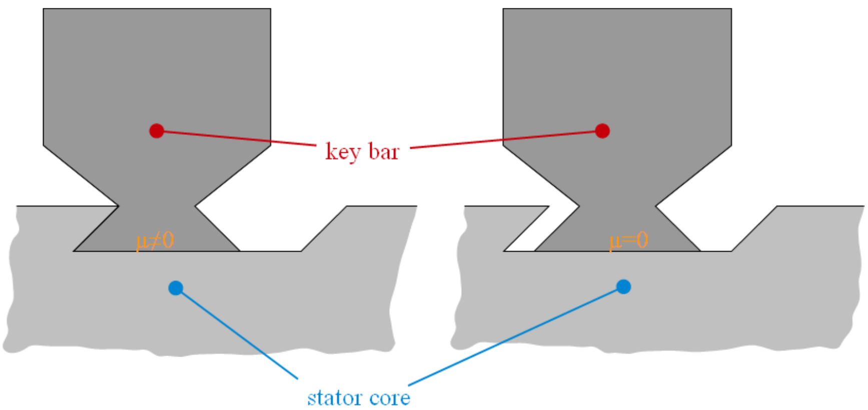

Figure 6-64: Comparison: real (left) and assumed (right) initial position / conditions

6.7.2 Representative Modeling of the Gap

The model for the FE calculation is the same as used for the previous calculations. The only modification is the nodal connection between core and frame. At the original simplified model, the core-to-frame connection was realized by “shared” nodes between core and frame. Now core and frame have independent, but coincident nodes. These nodes are connected by the COMBIN40 element of ANSYS (Figure 6-65).

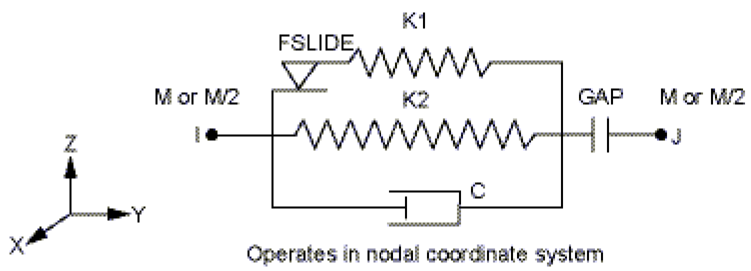

Figure 6-65: COMBIN40 element of ANSYS

The mechanic properties are defined by real constants.

FSLIDE, C and K2 are set to zero, what will remove these capabilities from the element (resp. replaces it by a rigid connection in case of FSLIDE). K1 becomes a high stiffness (1E12 N/m) assigned. For GAP the value 0.7 mm is used.

The gap property depends on the moving direction, like it is shown in the figure above. It just closes if both nodes move towards each other. To ensure that the gap gets also closed when both nodes are moving away from each other (which is necessary, since the excitation force is alternating)[11], a second COMBIN40 element is attached inverted (nodes I and J are exchanged).

6.7.3 Calculation results

Initially the core is not in contact with the key bar; the gap is 0.7 mm on both sides of each dovetail bar. There is also no initial velocity. According Figure 6-49, the effect on the final results is expected to be low.

[11] Due to the shape of the punching’s clearance for the dovetail bars, the gap actually closes just on one side of each dovetail bar. But as the dovetail shape is alternating, it is assumed that every gap closes on both sides. (Because the dovetail bars are relative close together, the strain is expected to be insignificant low.)

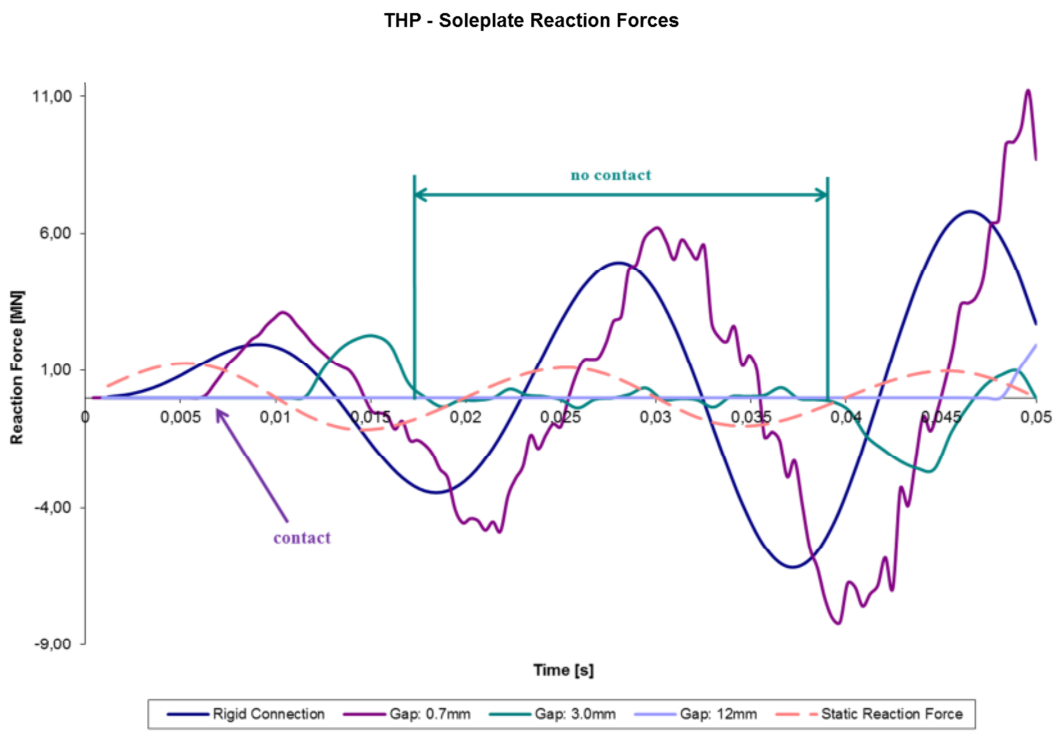

Figure 6-66: "THP" Soleplate Reaction Forces with various key bar clearances

The deep purple line in Figure 6-66 shows the soleplate reaction force (of one single soleplate), regarding the common 0.7 mm clearance between the core and the flange of the dovetail bar. The peak value is even higher compared to this one having a rigid connection (dark blue line).

At the time the gap closes (deep purple arrow), the excitation force (related to the dashed, coral colored line) is already decreasing but sill acting in the same direction that the core moves. So the core hits the frame and the whole energy is transferred to the soleplates. Additionally the excitation torque is still acting in the same direction, which also increases the reaction force at the soleplate.

One possibility to reduce the reaction force at the soleplates is to enlarge the gap to a distance, where the excitation force inverts its direction before the core hits the key bar. The negative excitation force would help to decelerate the core and relieve load from the frame. For instance, for a 50 Hz frequency the gap must not close before 0.01 s which leads to a gap of approximately 3 mm for "THP" (green line). It can be seen that the core seems not to be in contact with the frame between t~0.018 s and t~ 0.04 s. Within this time range, the frame seems to oscillate with its natural frequencies until the core hits the frame again on the other side of the key bar.

If the gap is enlarged further, to a distance so that the excitation force is able to decelerate the core before it gets in contact with the key bar at any time, no forces will be transferred to the soleplates at all (bright blue line). In a case of a 12 mm gap, the core hits the frame not before the 3rd cycle. But this case is just due to the assumed simplifications possible (see Chapter 6.7.1). In reality this situation will never occur, since the core is tangentially always in contact with the key bar.

Summarized it can be said that an enlargement of the gap by a factor of 4 and above will improve the dynamic situation in a case of failure. But designing a clearance of 3 mm in reality is not practicable. It would not be possible to position the single laminations when stacking the core. And even if the core is stacked properly, the core might deform abnormally when it's loaded by torque and there will be a significant tangential hit of the core to the key bars after every time the generator is powered-on.

The initial expectations were that there might be a natural force reduction in a case of failure. But as seen, the natural frequencies are not low enough and also the non-stiff core-to-frame connection has no positive effect in terms of force reduction either. So the most promising way to reduce soleplate forces will be to support the stator on springs.

7 Soleplate Force Reduction

A commonly used method to reduce foundation forces, caused by the dynamic of a machine, is to support the machine on springs. Springs reduce the stiffness of the machine connection to the ground and lower the natural frequency. If the first natural frequency is lower than the main excitation frequency, a reaction force reduction can be achieved. This force reduction is caused by the phase shift between excitation and reaction force. This effect can be explained by having a look at equation (2.22). Is the excitation frequency below the first natural frequency ($\eta = \Omega/\omega < 1$) the term $1/\left|1-\eta^2\right|$ becomes bigger than 1. The term becomes infinite in the case of $\eta = 1$ (resonance). But is the excitation frequency higher than the natural frequency ($\eta > 1$), this term becomes smaller and smaller and reduces the total displacement (resp. force) again. Remember that damping is not regarded ($D = 0$) and that there is no speeding up of the excitation frequency. So the first mode will never be gone through.

This chapter has a look at the required order of magnitude of the spring stiffness for stators with the help of the previously chosen reference projects and discusses potential designable solutions.

7.1 Initial estimation of the Spring Stiffness

First, an estimation of the required spring stiffness is required. A fine adjustment of the spring is done later. However, the estimation is based on the natural torque frequencies and an additional (fictive) torque spring is representing the spring mounted support. For this rough, first estimation the transfer matrices method and the 1-D model from Chapter 5.1.1 can be used. But in this case the stiffness of the **whole stator** (core + frame) must be regarded.

7.1.1 Determining the Stator Stiffness

The torsional stiffness of the whole stator is determined with the help of the simplified FE model, by applying torque on the inner radius of the stator core and measuring the displacement. As there are more nodes on the stator core inside than it is convenient for the TMM, average values are built. At first, an average value of the tangential displacements is calculated for each row of nodes (illustrated in Figure 7-67 by the quarter cycle, representing the inner radius of the core, and the orange dots, representing 3 displacement measuring points of one axial node level; the grey arrows represent the averaging). All remaining axial nodes (red dots in Figure 7-67) are grouped again into 4 to 8 groups (3 groups in Figure 7-67). An average displacement value built among each group is representing the group (blue dots in Figure 7-67). These few (~7) average displacement values are now manageable by the TMM.

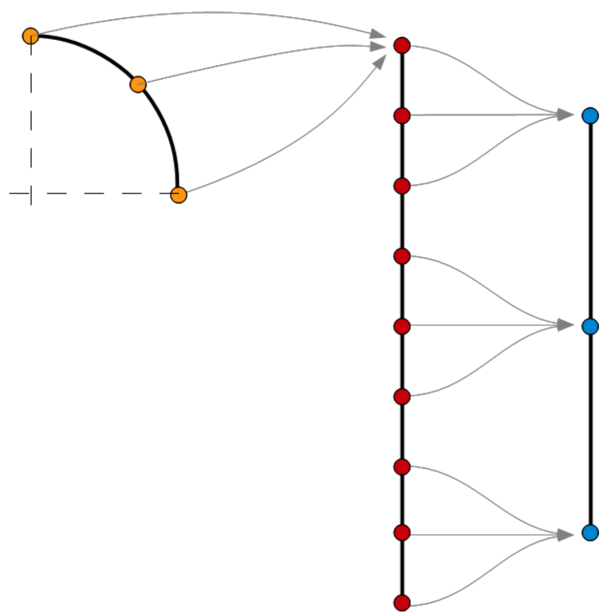

Figure 7-67: Illustration of the displacement averaging

Now the average displacements on several axial locations are known as well as the applied forces. Equation 7.37 can be used to achieve the stator stiffness values at each of these locations.

$$c_{\varphi\_i} = \frac{\sum_{k=1}^{i} T_k}{\varphi_i - \varphi_{i+i}} \tag{7.37}$$

This approach is tested for its accuracy by using the values of project "Mica", which has a first natural frequency of 59.0 Hz (simplified model). The inner area of the core has 324 nodes in tangential direction and 49 in axial direction (15,876 nodes in total). Like in Chapter 5.1.1, again the stator is abstracted into a reduced amount of rotary masses and torsional springs. But in this case 7 rotary masses and 7 torsional springs are used (to increase the accuracy). Furthermore the equivalent model differs slightly to the one used in Chapter 5.1.1, as the stator is now connected to the ground (compare Figure 7-68). Now to calculate the spring stiffness for each of the 7 torsional springs, all the inner core nodes are grouped into 7 groups of 7 nodes (like illustrated in Figure 7-67). The resulting average torsion of each group of nodes is:

$$\varphi_1 = 3.4296 \cdot 10^{-6}\, rad$$
$$\varphi_2 = 3.3789 \cdot 10^{-6}\, rad$$
$$\varphi_3 = 3.2001 \cdot 10^{-6}\, rad$$
$$\varphi_4 = 2.9566 \cdot 10^{-6}\, rad$$
$$\varphi_5 = 2.6520 \cdot 10^{-6}\, rad$$
$$\varphi_6 = 2.2745 \cdot 10^{-6}\, rad$$
$$\varphi_7 = 1.6399 \cdot 10^{-6}\, rad$$

Regarding the applied torque (resp. forces) as earlier described, the stiffness of each node group is:

$$c_{\varphi\_1} = 1.77355 \cdot 10^{13}\, \frac{Nm}{rad}$$
$$c_{\varphi\_2} = 1.0464 \cdot 10^{13}\, \frac{Nm}{rad}$$
$$c_{\varphi\_3} = 1.16626 \cdot 10^{13}\, \frac{Nm}{rad}$$
$$c_{\varphi\_4} = 1.25060 \cdot 10^{13}\, \frac{Nm}{rad}$$
$$c_{\varphi\_5} = 1.26612 \cdot 10^{13}\, \frac{Nm}{rad}$$
$$c_{\varphi\_6} = 9.06010 \cdot 10^{12}\, \frac{Nm}{rad}$$
$$c_{\varphi\_7} = 4.05523 \cdot 10^{12}\, \frac{Nm}{rad}$$

The mass inertias of these 7 rotary masses are:

$$\Theta_{Frame} = m_{Frame} \cdot \left(r_{Co} + \frac{r_{Fo} - r_{Co}}{2} \right)^2 = 3.79035 \cdot 10^6\, kg$$

$$\Theta_{Core} = m_{Core} \cdot \left(r_{Ci} + \frac{r_{Co} - r_{Ci}}{2} \right)^2 = 1.38657 \cdot 10^7\, kg$$

$$\Theta = \Theta_{Frame} + \Theta_{Core} = 1.76561 \cdot 10^7\,kg$$

$$\Theta_{Top} = \Theta_{Bottom} = \frac{\Theta}{12}$$

$$\Theta_{Middle} = \frac{\Theta}{6}$$

Verification of the calculated values

To verify the accuracy of these previously calculated stiffness and mass values, they are used for a 1-D calculation in ANSYS. Therefore these 7 rotary masses and 7 torsional springs are connected to represent this system according Figure 7-68. The result of a modal analysis shows a first natural frequency at 55.2 Hz, which is a good comparison compared to the natural frequency of the simplified model, which is at 59.0 Hz. The transfer matrices method with this model delivers 56.5 Hz.

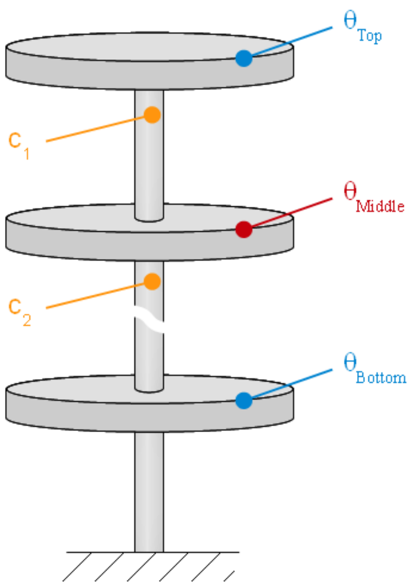

Figure 7-68: Equivalent model for the transfer matrices method and the 1-D ANSYS verification

Now with this model (Figure 7-68) and the (verified) spring stiffness and rotary mass values, the additional spring stiffness, which is required to reduce the natural frequency to a desired value, can be calculated.

7.1.2 Determining the additional spring's stiffness

To achieve the reduction of the natural frequency, the stiffness of the stator is reduced by applying springs at the soleplate. This means for the equivalent model used for the transfer matrices method (Figure 7-68), that an additional spring must be applied. This is done by adding fictively a spring in series (stiffness: c_{add}) to the last spring on the bottom. For the calculation there will be no additional spring applied, but a new, reduced spring stiffness of the very bottom spring (c_{7_comb}) is calculated. By the help of c_{7_comb} and the original stiffness of the very bottom spring (c_7), the stiffness of an additional spring can be calculated with the help of Equation 7.38.

However, the stiffness can be calculated by the transfer matrices method, since the frequency is known. (The frequency now is the desired first natural frequency.) An example is shown below, again with the values of “Mica”:

The original stiffness of “Mica’s” most bottom spring is $c_7 = 4.05523 \cdot 10^{12}\ Nm/rad$. This stiffness is set to unknown so that the first row φ of the last transfer matrix is:

$$
\begin{aligned}
&-2.7\cdot10^{-13}\Theta\omega^2 + 1.2\cdot10^{-26}\Theta^2\omega^4 - 1.7\cdot10^{-40}\Theta^3\omega^6 + 1.1\cdot10^{-54}\Theta^4\omega^8 - 3.3\cdot10^{-69}\Theta^5\omega^{10} + \\
&3.5\cdot10^{-84}\Theta^6\omega^{12} - \frac{\Theta\omega^2 - 8.6\cdot10^{-14}\Theta^2\omega^4 + 2.1\cdot10^{-27}\Theta^3\omega^6 - 2.3\cdot10^{-41}\Theta^4\omega^8}{c7} - \\
&\frac{1.2\cdot10^{-55}\Theta^5\omega^{10} - 3.0\cdot10^{-70}\Theta^6\omega^{12} + 2.9\cdot10^{-85}\Theta^7\omega^{14}}{c7} + 1 = 0 = \varphi
\end{aligned}
$$

Using the value $c_7 = 4.05523 \cdot 10^{12}\ Nm$ will lead to the first natural frequency of 56.5 Hz again. As it is desirable to lower the first natural frequency to i.e. 20 Hz, ω is set to $\omega = 125.664\ rad/s$. Solving the equation will lead to a new spring stiffness of $c_{7\_comb} = 2.942 \cdot 10^{11}\ Nm/rad$.

To check this new stiffness value, a modal analysis of the equivalent model with this new spring stiffness (c_{7_comb} instead of c_7) has been performed in ANSYS. The calculation delivers a natural frequency of 18.6 Hz, which fits to the desired value of 20 Hz very well.

But as mentioned, this is the **combined** value of the original stator spring stiffness and the serially connected additional spring. So the value of an **additional** applied spring still must be calculated:

$$\frac{1}{c_{7\_comb}} = \frac{1}{c_7} + \frac{1}{c_{add}} \tag{7.38}$$

c_{add} now is the total additional torsional spring stiffness.

In the case of “Mica”, this means:

$$\frac{1}{2.942\cdot 10^{11}} = \frac{1}{4.05523\cdot 10^{12}} + \frac{1}{c_{add}}$$

$$\Rightarrow c_{add} = 3.172\cdot 10^{11}\ \frac{Nm}{rad}$$

But this additional spring is still a torsional spring, and a torsional spring can not be designed for a generator in reality. Required are linear springs, which are attached to the soleplates – in reality as well as for the calculation. Remember, in the simplified FE model the soleplates are represented by fixing a certain number of nodes tangentially (soleplate nodes, see Figure 3-33). Now to be able to perform calculations with the simplified model, the linear spring stiffness value for each soleplate node (c_{SPN_i}) is required. It depends on the number of soleplates, the number of soleplate nodes and the radial location of the soleplate nodes.

$$c_{\varphi\_SPN} = \frac{c_{\varphi}}{n_{SP}\cdot n_{SPN}}$$

$$c_{SPN\_i} = \frac{c_{\varphi\_SPN}}{r_{SPN\_i}^{2}}$$

Performing a modal analysis with the FE model of the whole stator and using the previously calculated soleplate spring stiffness delivers a first mode frequency of 20 Hz. This procedure has been performed with every other project. The resulting spring stiffness were also verified by an modal analysis, as it is described in the next chapter.

7.2 Frequency Response Analysis

To determine how accurate the previously estimated spring stiffness values are, modal analyses have been performed for each machine with its appropriate foundation springs. If the reduction of the first mode frequency was high enough, a frequency response analysis has been performed to see the amount of the force reduction. Figure 7-69 below shows the plotted result of the frequency response analysis of “Mica”.

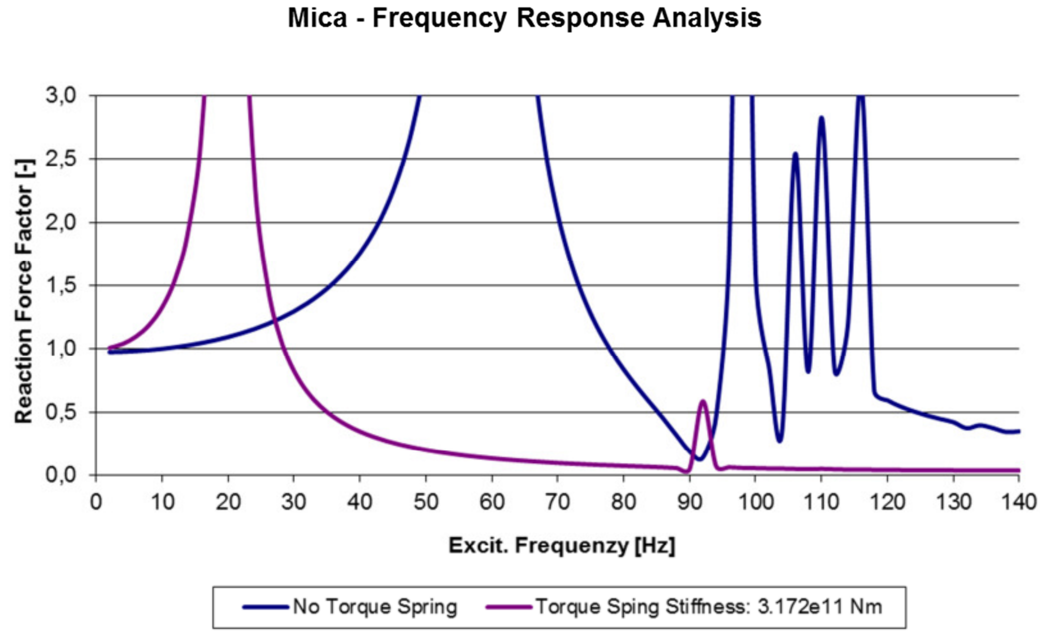

Figure 7-69: Frequency Response Analysis of one single Soleplate of "Mica" (blue: without soleplate spring; red: with soleplate spring)

On the ordinate, the so called reaction force factor η is plotted ($\eta = F_{SP\_dyn} / F_{SP\_stat}$). The reaction force factor is the harmonic reaction force amplitude for each excitation frequency divided by the static reaction force with the same excitation force value. Both plots in Figure 7-69 have a reaction force factor close to 1 in case of a low excitation frequency, which is comparable to a static excitation.

The blue line is the frequency response analysis of "Mica" without springs applied. The reaction force factor rises up close to infinite at approximately 60 Hz.

The deep purple line is the result of "Mica" with applied soleplate springs (total torque spring stiffness: 3.172E11 Nm). To achieve a force reduction, the excitation frequency must be above approximately 29 Hz. At 60 Hz the soleplate reaction force is just 13% of the static reaction (η=0.1332).

The next chart shows reaction force factors η at 60 Hz of all reference projects, to be able to estimate the linear spring stiffness of *one single soleplate*. Note that the following values are based on a harmonic analysis and might be different to results of transient analysis. In general there is no point in comparing harmonic and transient analysis in any way. Especially in the beginning of an oscillating excitation on a body in its state of rest, the transient effects are significant – even in case of a harmonic-like excitation force. (The excitation force is assumed to be harmonic-like, as the amplitude for the double-frequency part is relative low.) For further calculations, this way allows creating these helpful curves with a minimum amount of time effort.

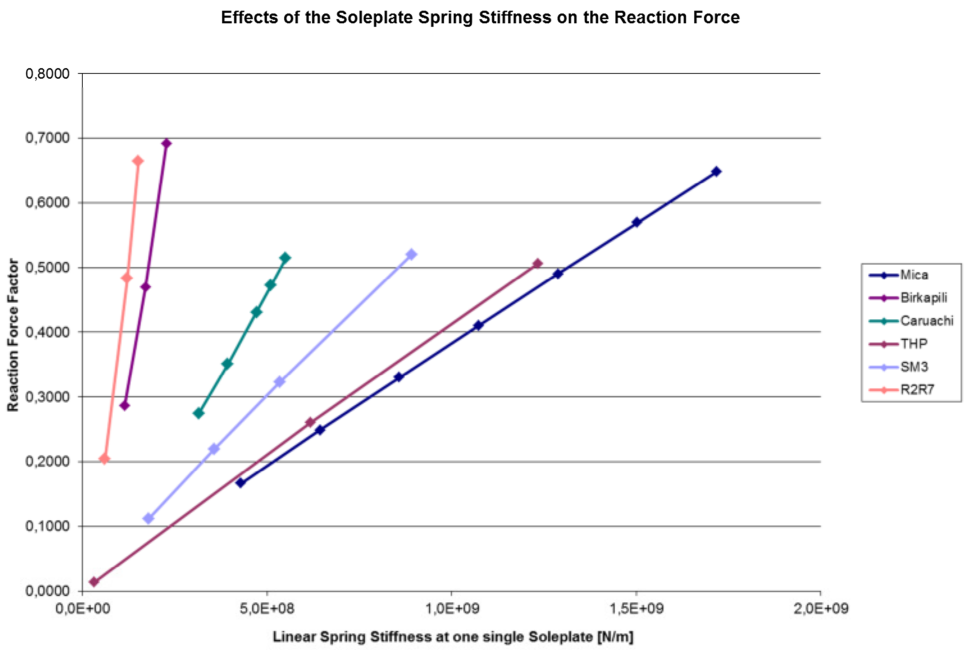

Figure 7-70: Reaction force factor at 60 Hz for different spring stiffness values

The curves in Figure 7-70 have all a linear trend. The table below shows the line function to be able to calculate the linear spring stiffness (required at one single soleplate) for a desired reaction force factor η.

Table 7-13: Soleplate spring stiffness functions

Project	c(η) [N/m]	c(η=0.25) [N/m]
Mica	$c(\eta) = 4.2935e8 + 2.6745e9 \cdot (\eta - 0.1666)$	6.52407E8
Birkapili	$c(\eta) = 1.14093e8 + 2.81225e8 \cdot (\eta - 0.2862)$	1.03913E8
Caruachi	$c(\eta) = 3.14301e8 + 9.80146e8 \cdot (\eta - 0.2743)$	2.90483E8
THP	$c(\eta) = 6.17128e8 + 2.50355e9 \cdot (\eta - 0.26)$	5.92093E8
SM3	$c(\eta) = 1.78379e8 + 1.74454e9 \cdot (\eta - 0.1116)$	4.19823E8
R2/R7	$c(\eta) = 6.02998e7 + 1.96417e8 \cdot (\eta - 0.2043)$	6.92761E7

7.3 Transient Soleplate Reaction

With the spring stiffness values from Table 7-13 (η=0.25) a transient analysis is performed in this chapter, the same way as in Chapter 6.

Table 7-14 shows the peak values of the soleplate reaction. The values "F_{static}" and "$F_{dynamic}$ without spring" originate from the original calculation without springs (Chapter 6, Table 6-11).

Table 7-14: Peak reaction values of one single soleplate in case of a 3-phase short circuit, soleplate spring attached

Project	F_{static} [MN]	$F_{dynamic}$ [MN] with spring	$F_{dynamic}$ [MN] without spring	F_{dyn}/F_{stat}	Spring stiffness per SP [MN/m]	Spring stiffness total [Nm/rad]
Mica	1.661	1.190	9.114	0.716	652.4	568.9E9
SM3	1.519	0.738	7.378	0.486	419.8	147.9E9
THP	1.244	1.193	6.795	0.959	592.1	60.3E9
R2/R7	0.223	0.144	0.579	0.646	69.3	7.2E9
Caruachi	0.986	0.637	4.530	0.646	290.5	227.4E9
Birkapili	0.349	0.305	0.815	0.883	103.9	3.5E9

Looking at the values "F_{dyn}/F_{stat}", it can be seen that the transient effects (and probably also the influence of the double-frequency) are very high. The used force reaction factor of η=0.25, on which the spring stiffness estimation is based, can not be reached within the first few cycles.

The charts on the following pages (Figure 7-71 to Figure 7-76) plot the dynamic reaction force by the excitation force. It can be seen that in there is no build-up of the reaction force in any case. All the 60 Hz machines ("Mica", "Caruachi" and "SM3") and the 50 Hz machine "R2R7" show a similar reaction force curve, with a peak in the first excitation cycle already, followed by an almost constant reaction force until the third excitation cycle occurs. "Birkapili" and "THP" also have the peak value within the first excitation cycle. But in contrast to the other machines, where after the first peak an almost reaction force occurs, the first peak for these machines is followed by a second peak value, which acts in the other direction but the amplitude is nearly the same.

The questions arising now are: How is it basically possible to implement a spring to the soleplate? How has the design to be? And is it possible at all, to design a spring which is elastic enough to reduce the natural frequency in this extent whereas the spring's yield stress must not exceed? These questions are discussed in its basics in the next chapter.

Charts of the Reaction Force in Case of a 3-Phase Short Circuit with soleplate springs attached

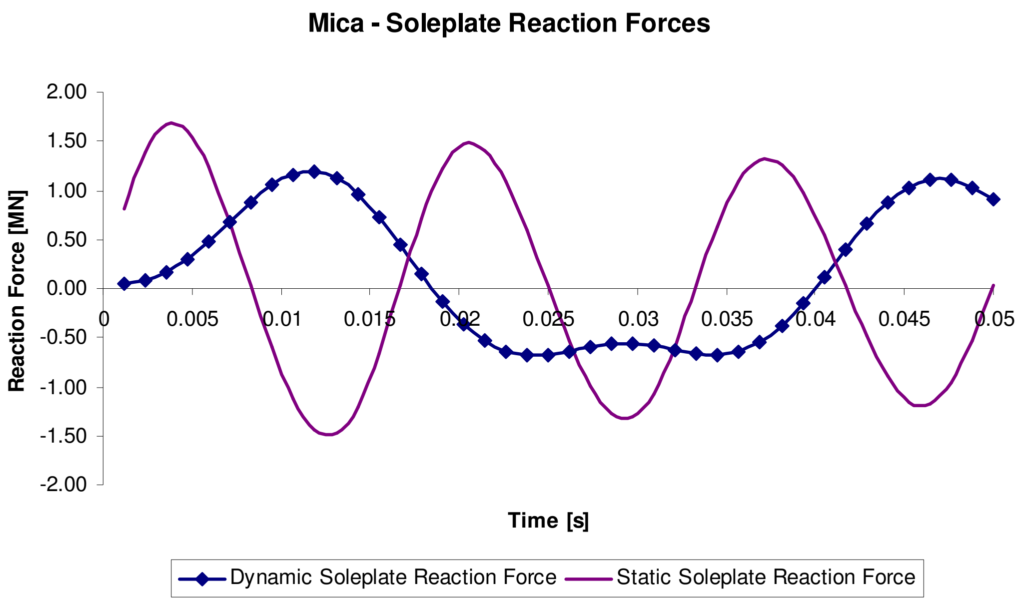

Figure 7-71: Soleplate reaction force of "Mica" with spring support in case of a 3-phase short circuit

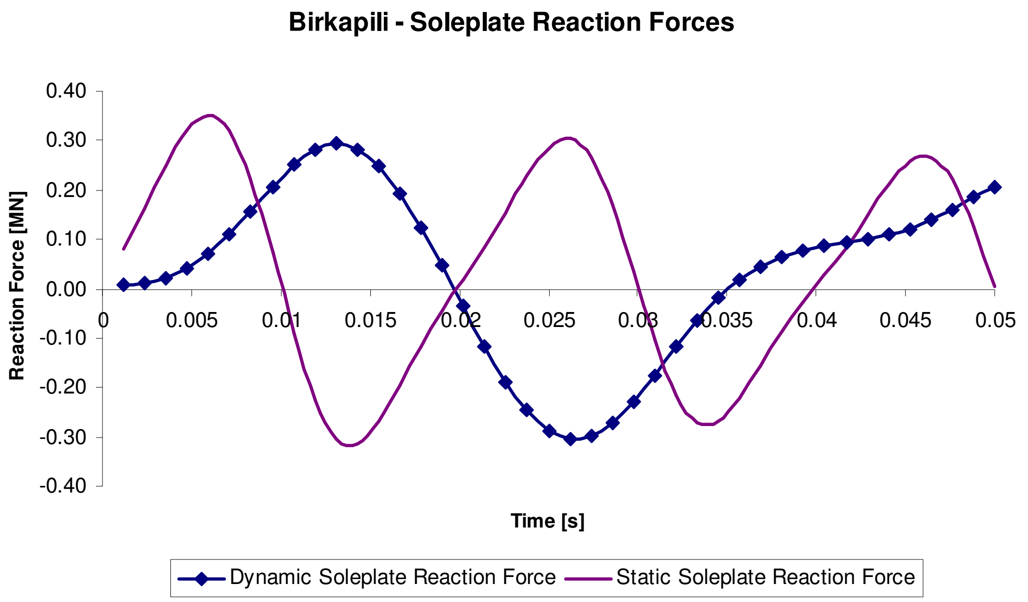

Figure 7-72: Soleplate reaction force of "Birkapili" with spring support in case of a 3-phase short circuit

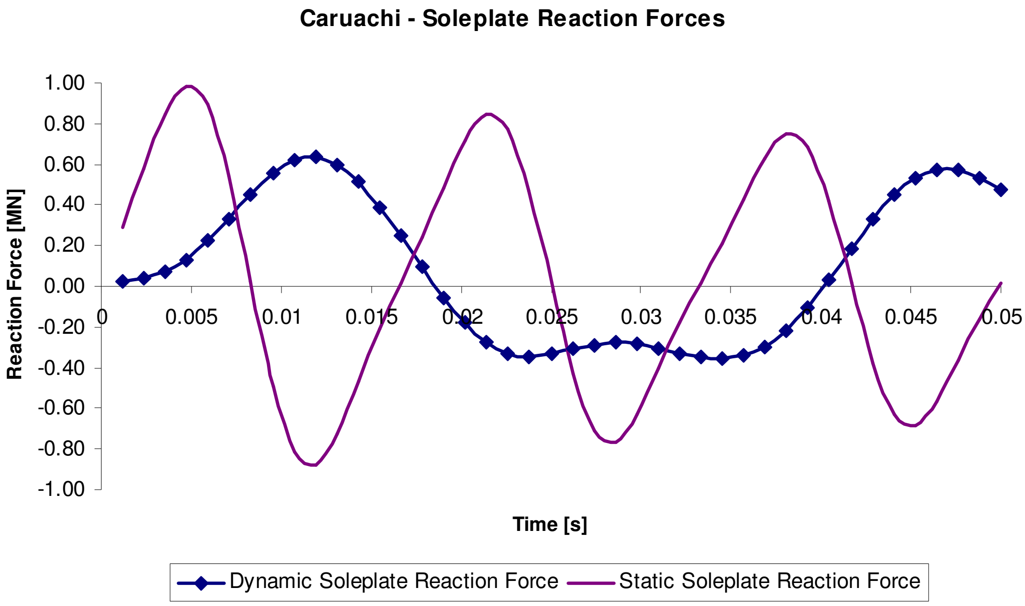

Figure 7-73: Soleplate reaction force of "Caruachi" with spring support in case of a 3-phase short circuit

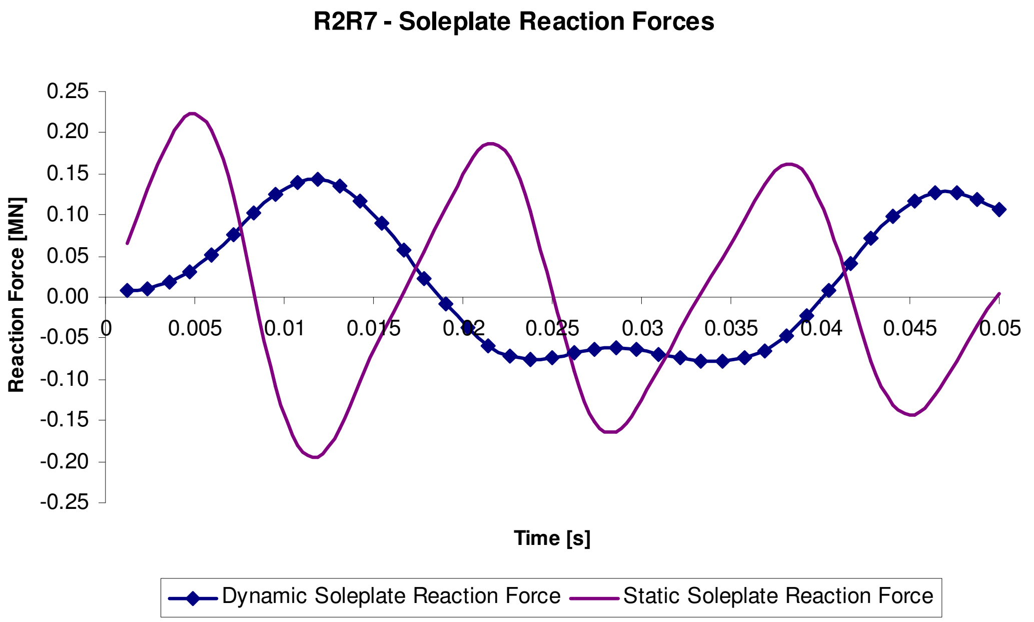

Figure 7-74: Soleplate reaction force of "R2R7" with spring support in case of a 3-phase short circuit

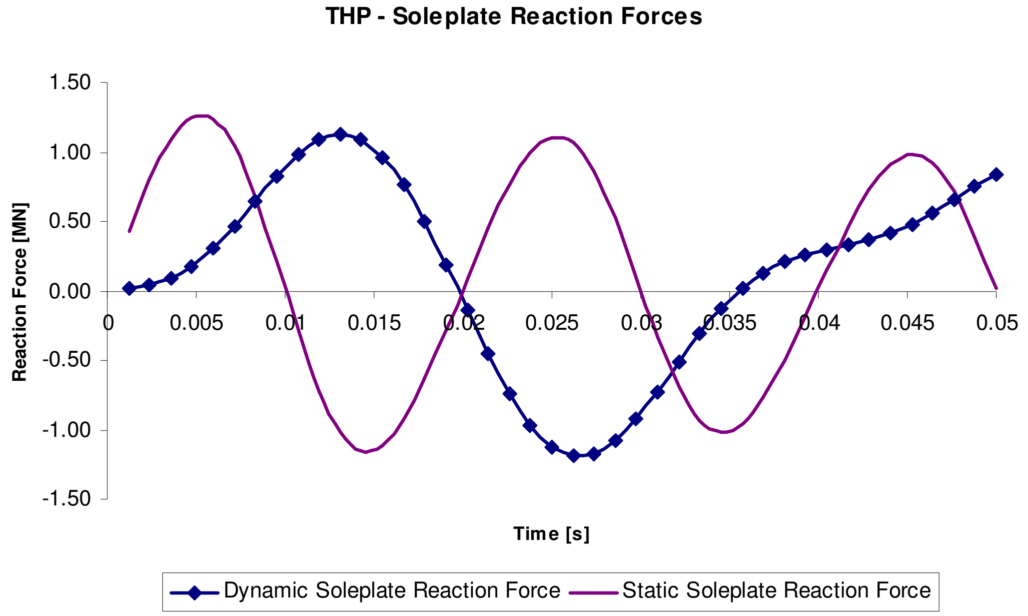

Figure 7-75: Soleplate reaction force of "THP" with spring support in case of a 3-phase short circuit

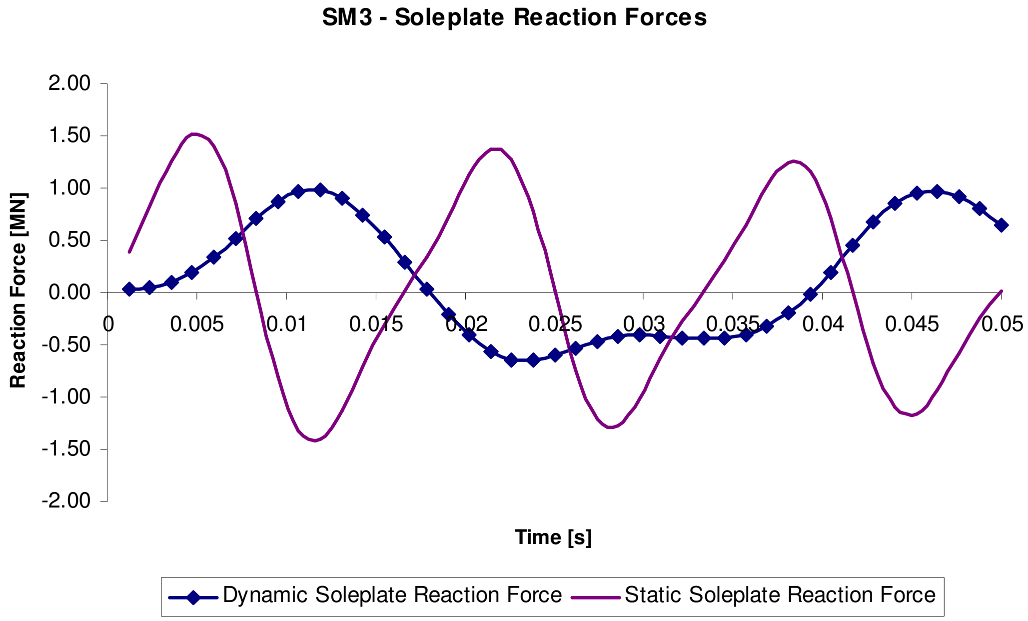

Figure 7-76: Soleplate reaction force of "SM3" with spring support in case of a 3-phase short circuit

7.4 Possible Implementation of a Soleplate Spring

7.4.1 Basic Soleplate Design

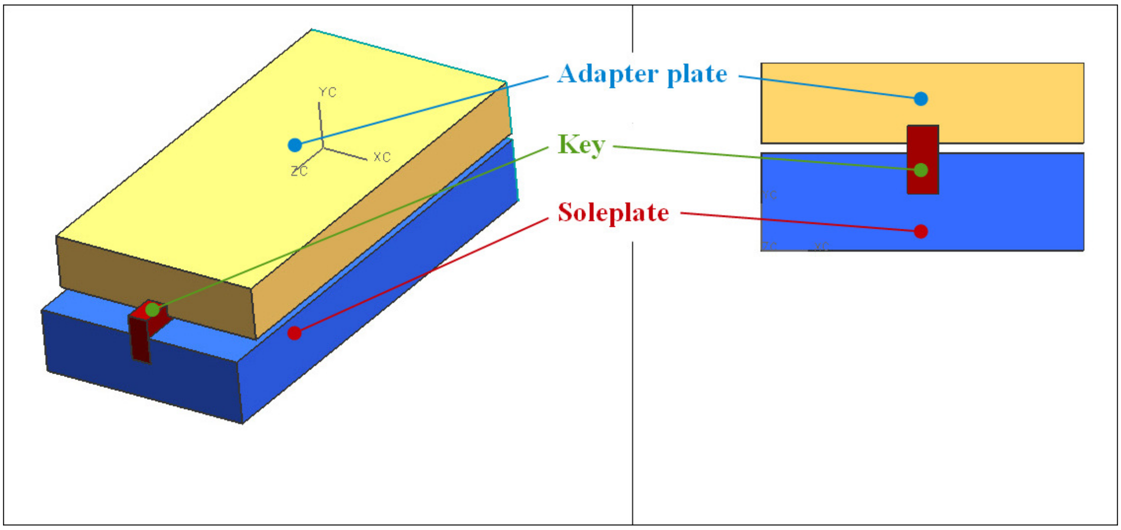

Figure 7-77: Scheme of the soleplate assembly group in 3-D and front view

Referring to Figure 7-77, the soleplate of the stator is built up from three parts. The adapter plate (yellow) is attached to the very bottom shelf of the stator. It transmits all torque forces over the key (red) to the actual soleplate (blue), which is embedded into the concrete. (The shorter length of the adapter plate is only sketched for illustration reasons. So is the gap between adapter plate and soleplate.) The advantage of this system is that the stator can expand easily in the radial direction. As mentioned, this is necessary to reduce buckling stresses in the core. To reduce friction on the slide surface (contact surface between the key and the adapter plate), the low-friction polymer PTFE is applied onto it.

All calculation values in this chapter are based on the machine “Mica”, if not explicit differently noted.

7.4.2 Torque Wave Keys

The so called torque wave keys are originally used as a part of the rotor. Due to the design of the soleplate it is possible to use this kind of spring design without major changes, just by replacing the common key with the torque wave key. Figure 7-78 illustrates the function and implementation.

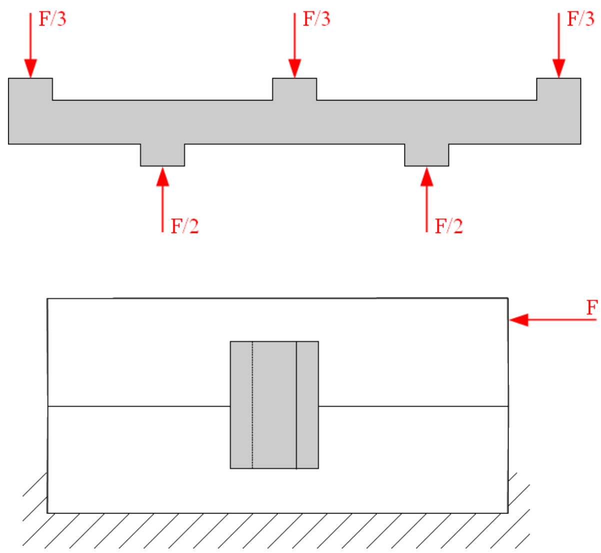

Figure 7-78: Top view of wave key (top) and frontal view (bottom) of assembled soleplate with wave key in the center

When designing the torque wave key, it must be ensured that the tooth offset is large enough. If the offset is too small, the wave key might get in contact with the soleplate at the opposite site of the tooth. This would result in a sudden significant increase of the stiffness. To avoid this case, it must be ensured that the maximal value of bending does not exceed the offset value. For a rough estimation, the tangential displacement of the free stator is calculated:

Using equation (6.36) from Mica and the time of half an excitation period ($t = 1/(2 \cdot 60) = 0.0083s$) lead to an approximate displacement of $\varphi(t = 0.0083) = 0.000305$.

Not regarded in this estimation is the mass of the frame ($m_{Frame} = 66701kg$ and $\Theta_{Frame} = 3.9254 \cdot 10^6 \, kg \cdot m^2$) and the tangential contact.

With the outer frame diameter of $D_F = 15.66m$ (which is approximately the average centerline distance of the soleplate), the tangential displacement of the stator is

$$s = 0.000305 \cdot \frac{15.66}{2} = 2.39mm .$$

Regarding also the stator mass, the values are:

$$\varphi(t = 0.0083) = 0.000238$$

$$s = 0.000238 \cdot \frac{15.66}{2} = 1.86mm \, .$$

An already existing Mathcad sheet allows calculating the spring stiffness of the torque wave key. Using the original key geometries of "Mica" (radial length: 830 mm, axial height: 98 mm, thickness without teeth: 38.1 mm), a tooth offset of 2 mm, a tooth width of 40 mm and a tooth amount of 5 (2 + 3) delivers a stiffness of 4.664E8 N/m. The maximal bending stress[12] according this Mathcad sheet is 0.9209E9 N/m^2, which is above the yield point of commonly used steel.

These values are tried to be confirmed by an FE calculation. Therefore, the spring is modeled (using the APDL of ANSYS again) and meshed. It is useful to use cartesian coordinate systems for this geometry. Therefore, the x-axis is along the key's (radial) length, the y-axis along its (tangential) width and the z-axis along its (axial) height. Boundary conditions are applied according to Figure 7-79. For these key calculations, the dead weight of the stator is not regarded. To avoid the key of spinning around its length axis, the key's bottom nodes are fixed in z-direction. They are also fixed in x-direction to keep it numerical stable. These boundary conditions (u_z=0 at location z=0 and u_x=0 at location z=[key length]/2) are not displayed in Figure 7-79.

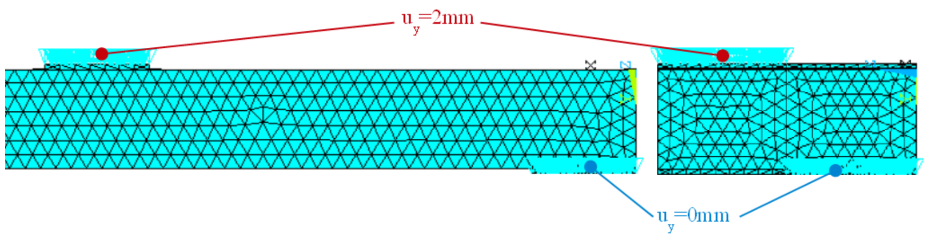

Figure 7-79: Top (left) and frontal view (right) of a part of the torque wave key with BC

Summing up the reaction forces on the contact surfaces show that a displacement of 2 mm is equal to an average force of 532785 N per tooth. Further calculations are based on this force value.

[12] The maximal bending stress is calculated by assuming the maximal possible bending, which is the tooth offset of 2mm.

Following images show different occurring stresses in the key. The key is cross sectioned at the second tooth.

Figure 7-80 shows the stress values in x-direction. The maximal stress values at the cross section (deep red oval) range from 0.853E9 N/m^2 to 0.162E10 N/m^2 (yellow-green contour area), which confirms the bending stress value from the Mathcad sheet (σ_{xx} = 0.9209E9 N/m^2). The neutral axis, where the bending stress changes its sign, can be seen well in the center (color turns from bright green into blue-green).

Figure 7-81 shows the shear stress τ_{zy} which mainly occurs due to the different z-locations of force application and reaction. The force from the stator is introduced at the two teeth on the right side, reaching from the center line (dark red) to the top. The force is transferred over to the key teeth on the left side, where the force is introduced into the soleplate. The contact between the key and the soleplate on the left side reaches from the center line to the bottom. This is why the shear stress has its maximum at the center (dark red line). Its peak value is approximately 0.2E9 N/m^2.

τ_{zy} has just a minor effect on the von Mises stresses in the cross section area (Figure 7-82). Just by having a look at the contour colors, it seems to be mainly influenced by bending stresses. The von Mises stress has its peak value at approximately 0.9E9N/m^2 at the outer edges of the cross section area. A summary of the stress values can be found in Table 7-15 of the next chapter.

Anyhow, the highest global stress values occur at the inner edges of the first and last tooth. This is a result of the bending shape. Whereas the inner teeth are pressed parallel against the soleplate, the outer teeth touch the soleplate within an angle. This value is far above the yield point and can be reduced by rounding the tooth.

One possibility to reduce the stress of this design is to increase the width or the height of the key. As this will also end up in an increasing of the stiffness, the radial length of key can be enlarged (while keeping amount of teeth constant) to reduce the stiffness again. But the radial length of the key is limited by overall dimensions. Furthermore the outer end of the soleplate should be as close as possible to the stator frame wrapper to avoid excessive eccentric force transmission.

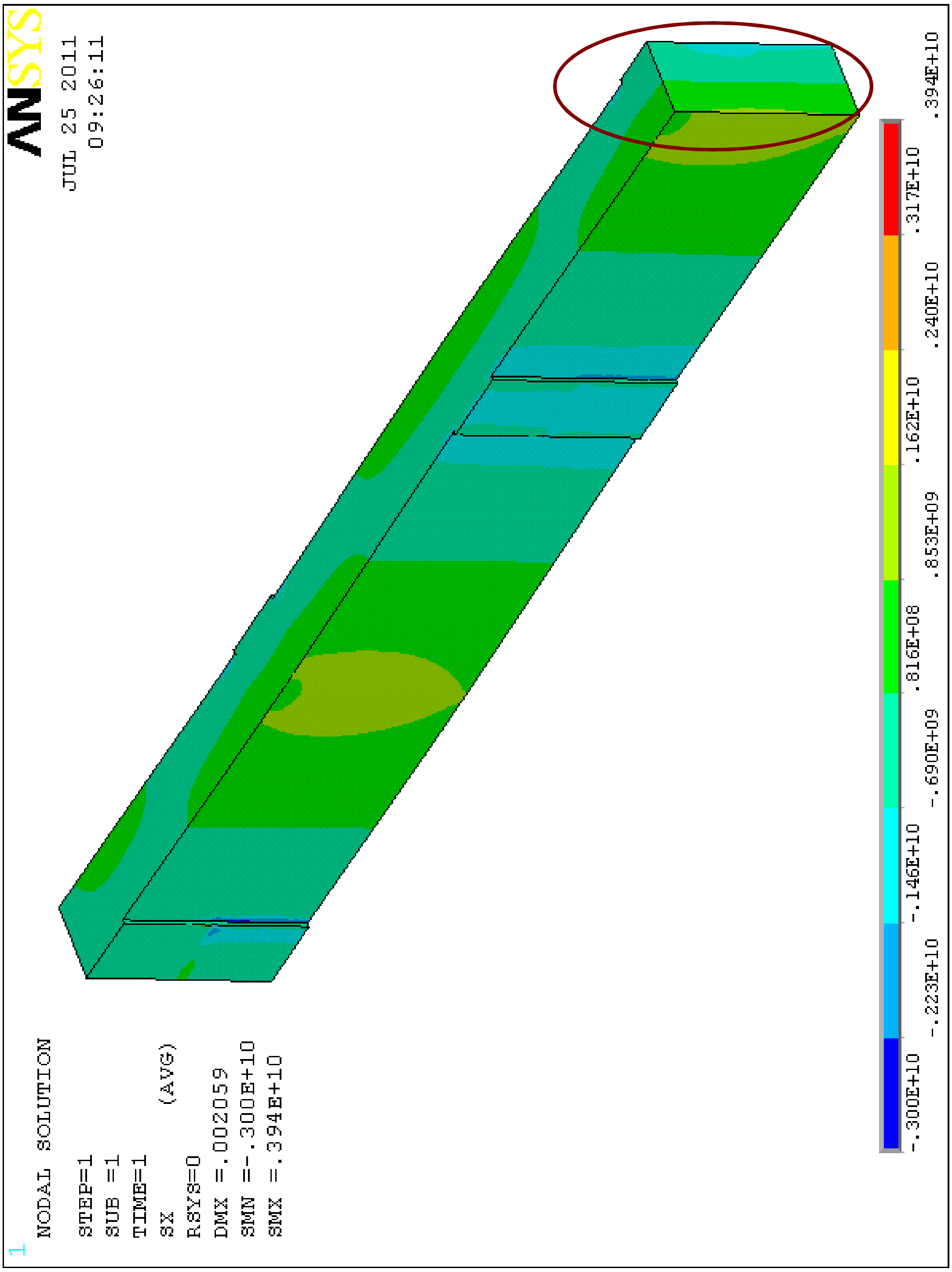

Figure 7-80: Wave key bending stress (σ_{xx})

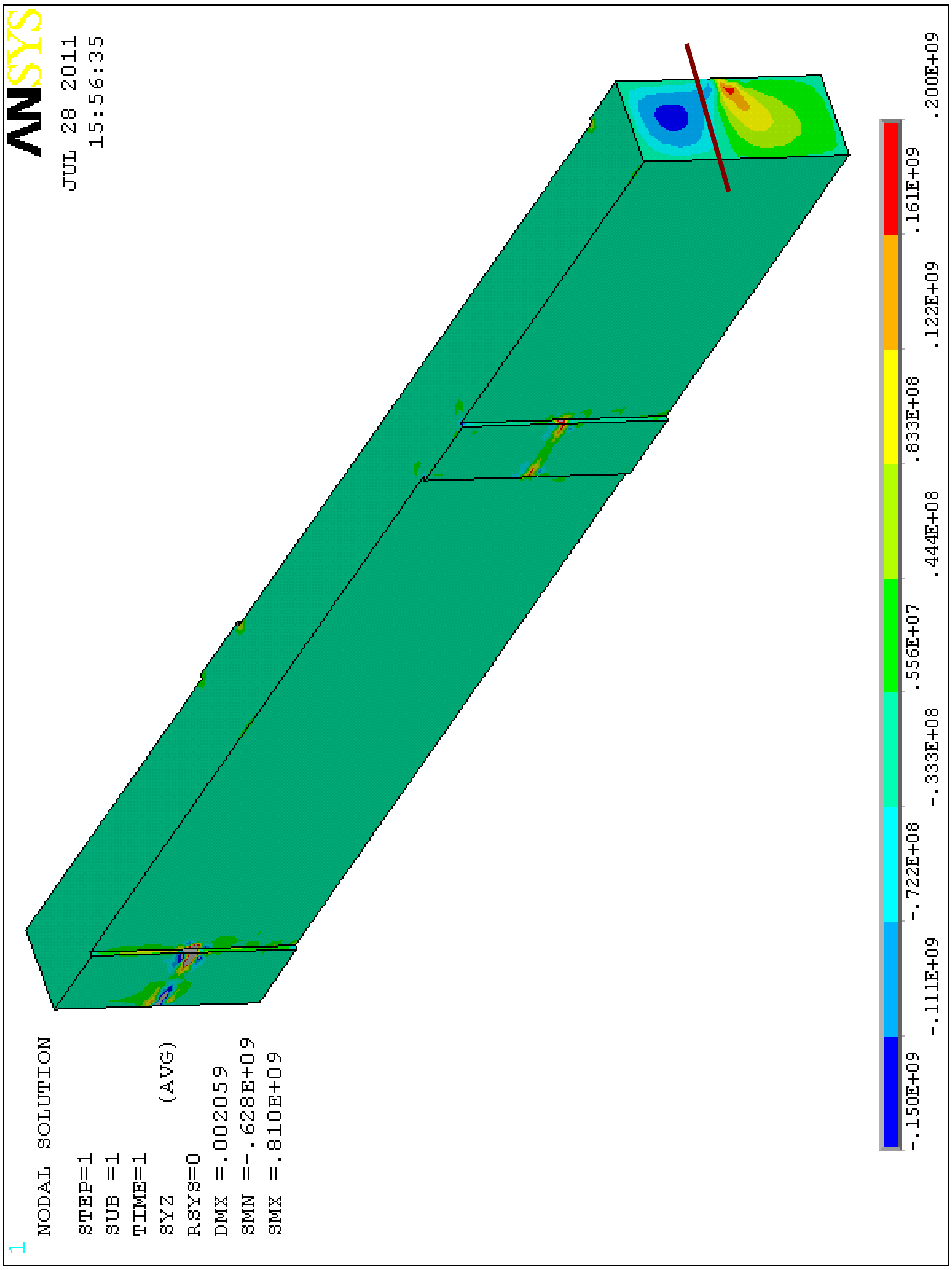

Figure 7-81: Wave key shear stress (τ_{zy})

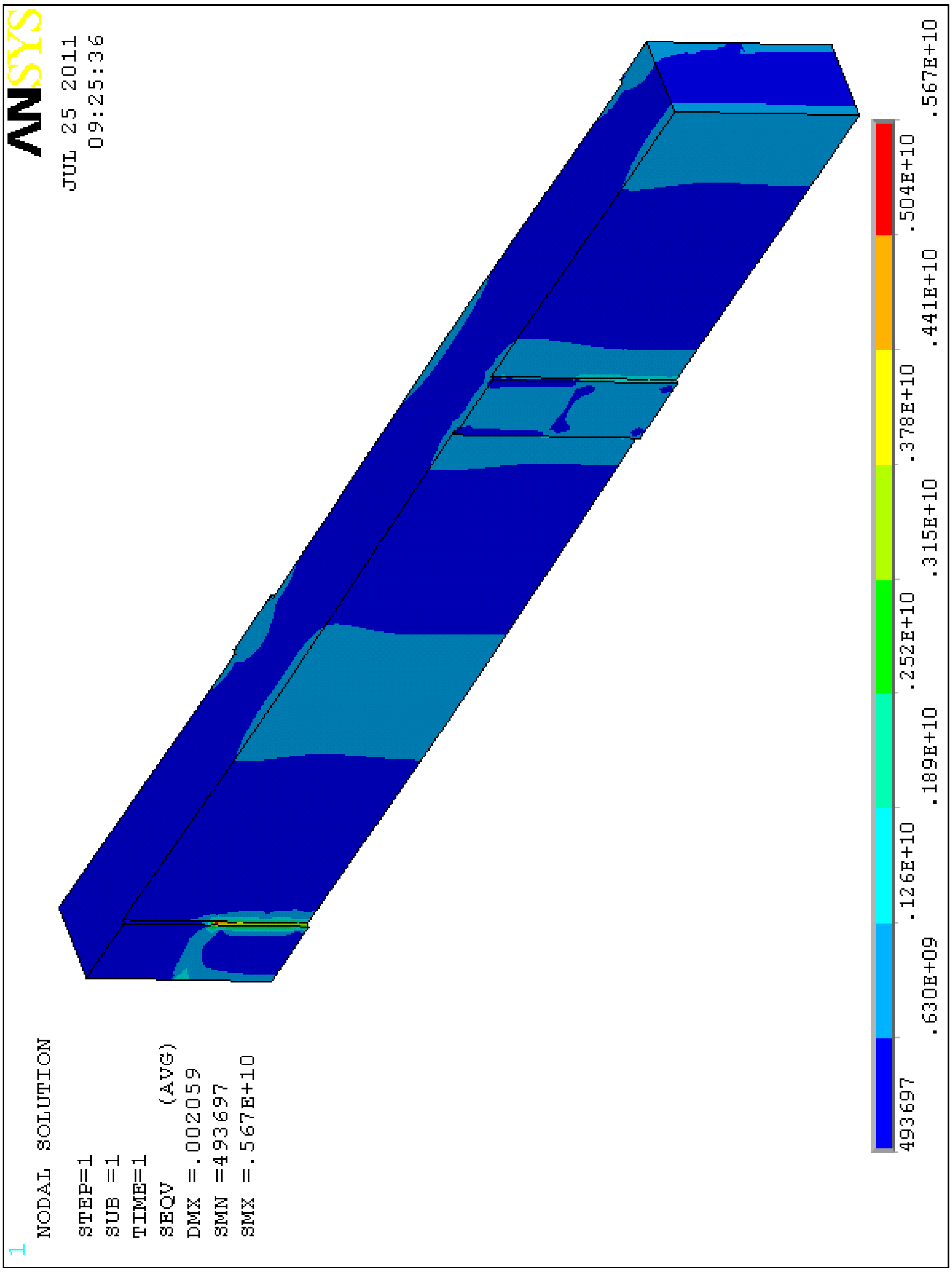

Figure 7-82: Wave key von Mises stress

7.4.3 Torque Wave Keys (Redesign)

Another possibility to reduce stress is by using a slightly different soleplate design, with two torque wave keys in separate notches.

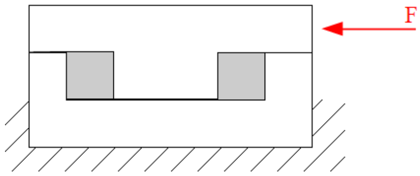

Figure 7-83: Soleplate redesign to reduce shear forces in wave keys

The benefit of this design is that the force is introduces along the whole area of each tooth. So large shear stress can be avoided what has a positive effect on the von Mises stress.
To make results comparable, not the displacement is applied, but the forces which caused the displacement of 2 mm of the previous model (= 532785 N per tooth). This force is applied as pressure:

$$p = \frac{F}{A} = \frac{532785}{40 \cdot 98} = 135.915 \frac{N}{mm^2} = 1.35915e8 \frac{N}{m^2}$$

Boundary conditions are applied according Figure 7-84. Not displayed in Figure 7-79 are again the boundary conditions in z- and x-direction at the bottom of the key.

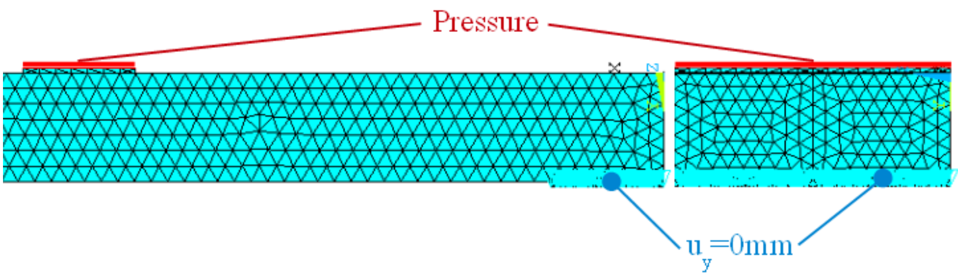

Figure 7-84: Top (left) and frontal view (right) of a part of the torque wave key with FE boundary conditions

The following images (Figure 7-85 to Figure 7-87) show different stress in the key. The key is cross sectioned at the second tooth.
Figure 7-86 shows that the shear stresses τ_{zy} could be reduced significantly with this design. The slightly asymmetric behavior of the shear stress in the cross section area

results from the boundary condition on the bottom area of the key. The final effect on the von Mises stress is very small as it can be seen in Figure 7-87. Also the spring stiffness increased to 5.9149e8 N/m. The major influencing stress is σ_{xx} (Figure 7-85), caused by bending. To reduce bending stress, the idea of applying two wave keys next to each other is researched in Chapter 7.4.4.

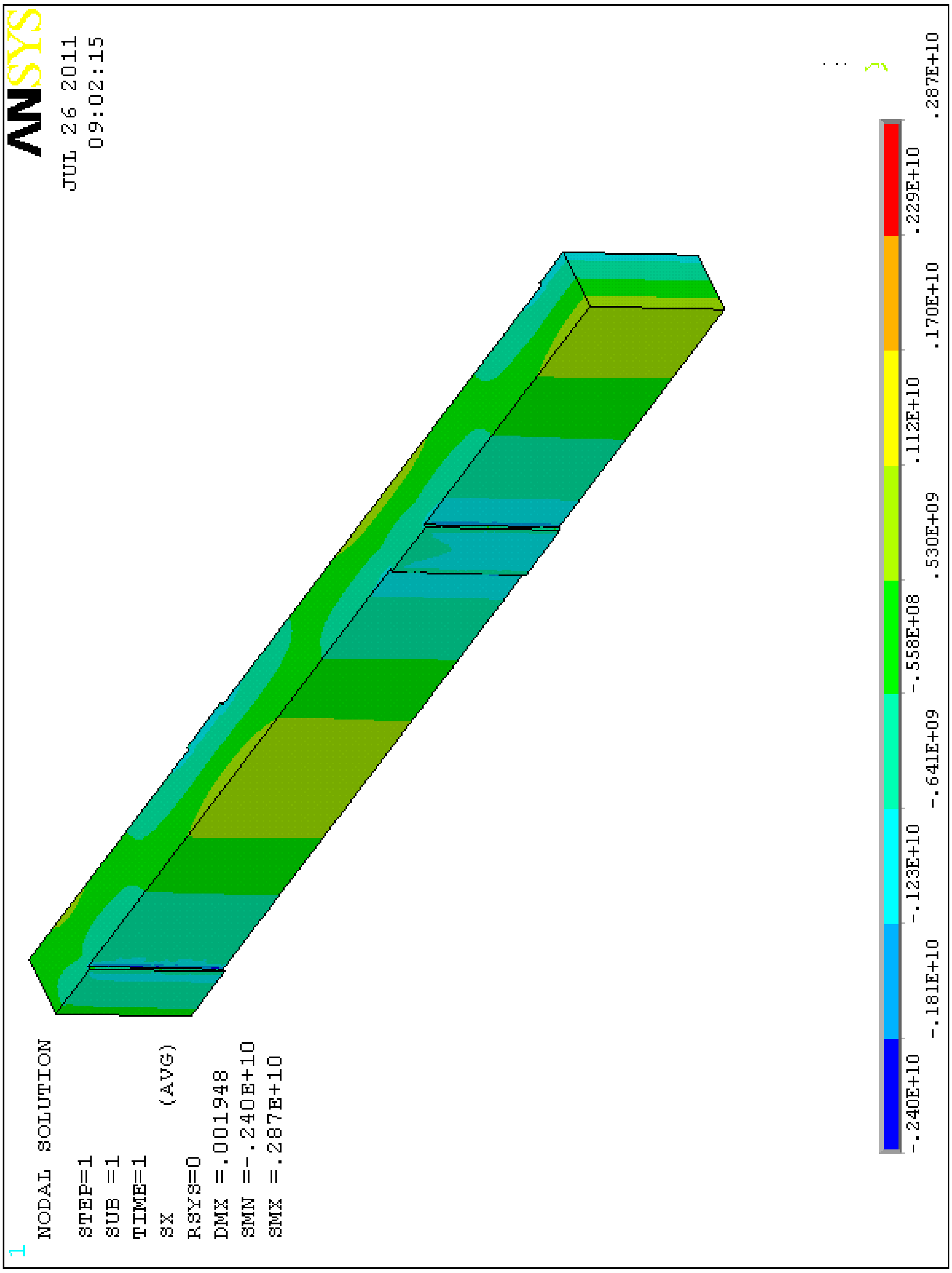

Figure 7-85: New wave key bending stress (σ_{xx})

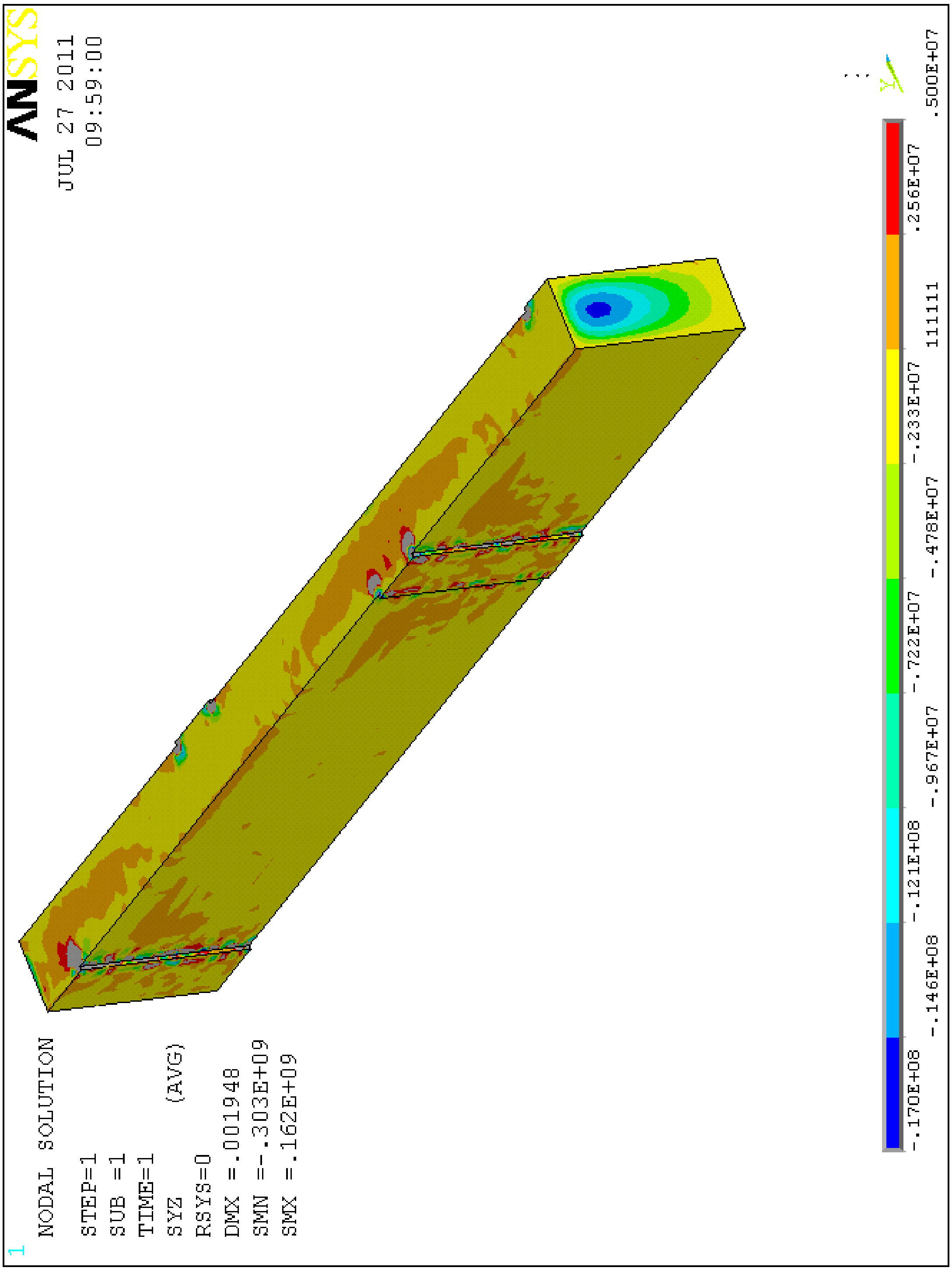

Figure 7-86: New wave key shear stress (τ_{zy})

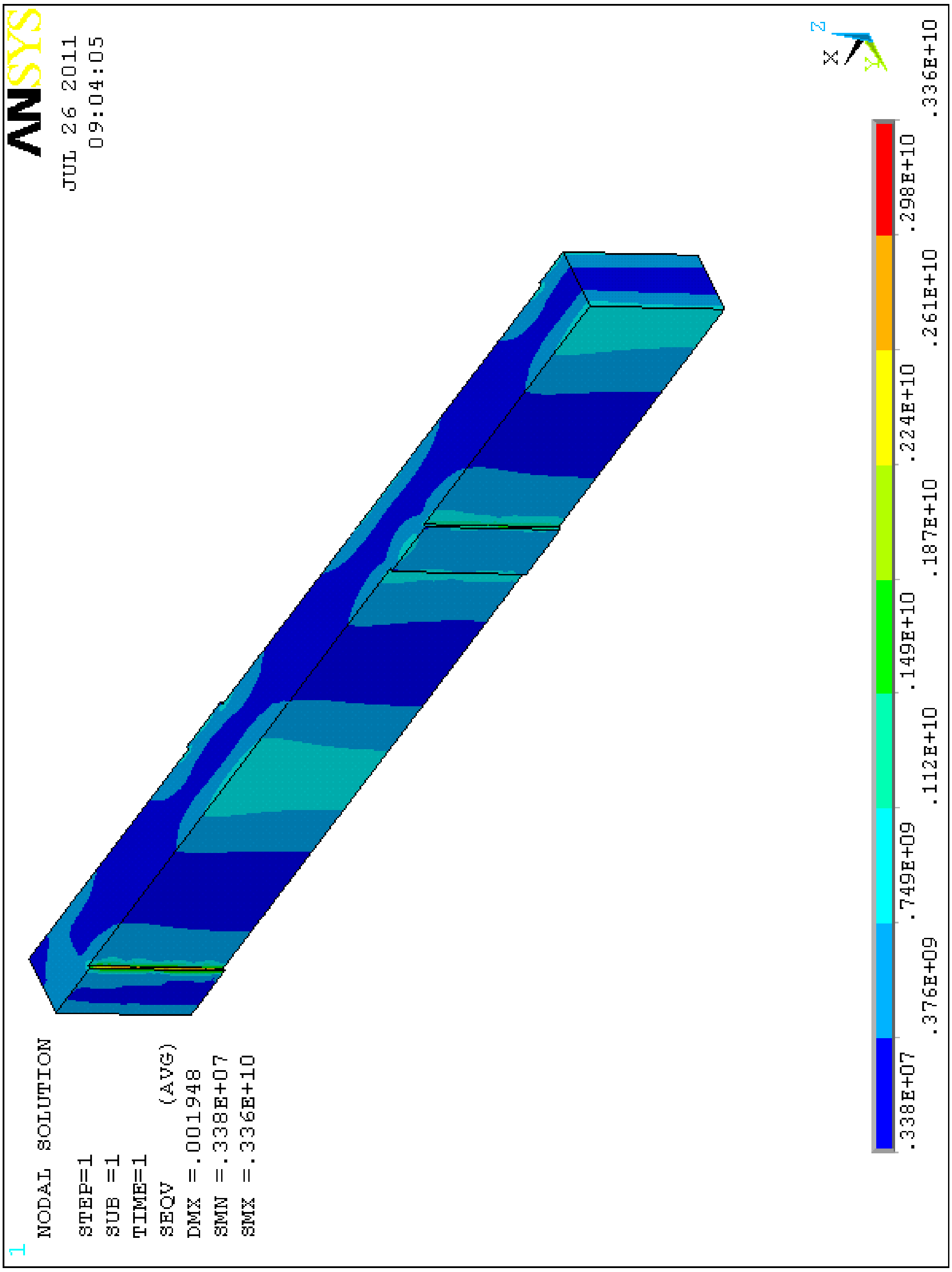

Figure 7-87: New wave key von Mises stress

Table 7-15 compares the two designs in terms of the stress and stiffness.

Table 7-15: Comparison of absolute peak stress values at cross section and stiffness values

Stress Type	Stress common design	Stress revised design
σ_{xx}	< 1.62E9 N/m^2	< 1.12E9 N/m^2
τ_{zy}	< 0.20E9 N/m^2	< 0.17E8 N/m^2
τ_{xy}*	< 0.20E9 N/m^2	< 0.20E9 N/m^2
von Mises	< 1.26E9 N/m^2	< 1.12E9 N/m^2
Stiffness (Mathcad)	4.664E8 N/m	--
Stiffness (FE)	5.3279E8 N/m	5.9149E8 N/m
Bending at tooth	2 mm (boundary condition)	1.802 mm (average)

*) The peak value of τ_{xy} does not appear in the yz-plane cross section of the tooth, but in the middle between two teeth.

All stress values in Table 7-15 are retrieved visually with the help of contour colors. FE stiffness values are calculated by applying a displacement at the appropriate locations and evaluating the resulting reaction forces.

Notes concerning the calculation of the values in Table 7-15

The stiffness, used for the commonly designed wave key, is calculated as follows:

The displacement is given with 2 mm. To achieve these 2 mm, an average force of 532785 N per tooth is required, as already mentioned. So the stiffness for one tooth is:

$$c_{tooth} = \frac{532785}{2 \cdot 10^{-3}} = 2.66393 \cdot 10^{8} \, \frac{N}{m}$$

As there is the second tooth acting as spring parallel to this one tooth, the total spring stiffness is:

$$c_{total} = 2 \cdot 2.66393 \cdot 10^{8} = 5.3279 \cdot 10^{8} \, \frac{N}{m}$$

The spring stiffness of the redesigned soleplate wave key is calculated by the applied force of 532785 N and the average displacement of the teeth:

$$\bar{u}_{y1} = 0.001799 m$$

$$\bar{u}_{y2} = 0.001804 m$$

$$\Rightarrow \bar{u}_y = \frac{0.001799 + 0.001804}{2} = 0.001802m$$

$$c_{tooth\_1} = \frac{532785}{0.001799} = 2.96156 \cdot 10^8 \frac{N}{m}$$

$$c_{tooth\_2} = \frac{532785}{0.001804} = 2.95335 \cdot 10^8 \frac{N}{m}$$

$$c_{total} = 2.96156 \cdot 10^8 + 2.95335 \cdot 10^8 = 5.91492 \cdot 10^8 \frac{N}{m}$$

$\bar{u}_{y1,2}$........................	Average displacement of tooth 1, 2 [m]
$\bar{u}_y$...........................	Total average displacement [m]

7.4.4 Paired Torque Wave Keys

By placing two wave keys next to each other, it is possible to increase the key's thickness (what will reduce the bending stresses σ_{xx}) while keeping the total spring stiffness constant (serial connection of springs, like illustrated in Figure 7-88).

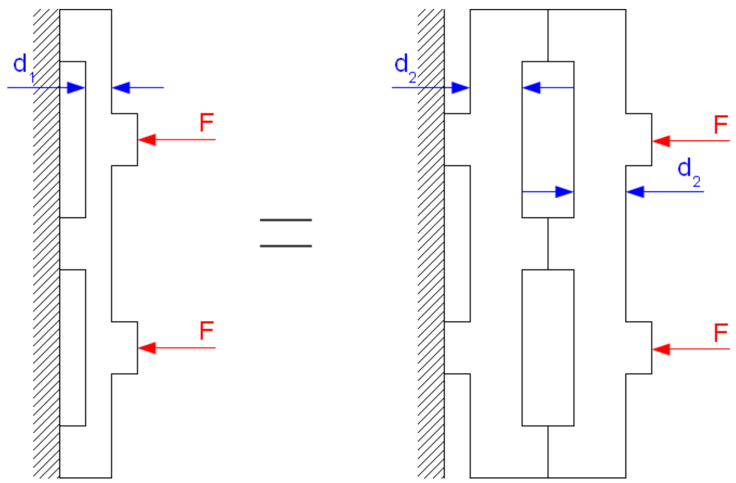

Figure 7-88: Scheme of paired torque wave keys

The total spring stiffness, which should be targeted for exemplification, is the key stiffness from the previous chapter (5.9149e8 N/m). Therefore one single wave key, among the combination of two, must have twice the stiffness: 1.1830E9 N/m.

The easiest way to get the necessary thickness value to reach this stiffness is to use the Mathcad sheet for the torque wave key again. It delivers a thickness of approximately 54 mm (instead of the original 38.1 mm). The stress outputted by the Mathcad sheet is not correct in this case. (The Mathcad sheet assumes that the wave key is bent the whole 2 mm (tooth offset) when calculating the stiffness. In the case of two serially connected wave keys and the same force, one single the key is not bent the whole 2 mm. This is also the reason why not the displacement is applied as BC the FE stress calculation, but again the force of 532785 N per tooth.)

Figure 7-89 to Figure 7-91 show the stress situation of one of the paired torque wave keys. This design improves the stress situation a lot. As it can be seen in Figure 7-89 to Figure 7-91, σ_{xx} and consequently von Mises stress reduce to approximately 50% of their values of the revised design.

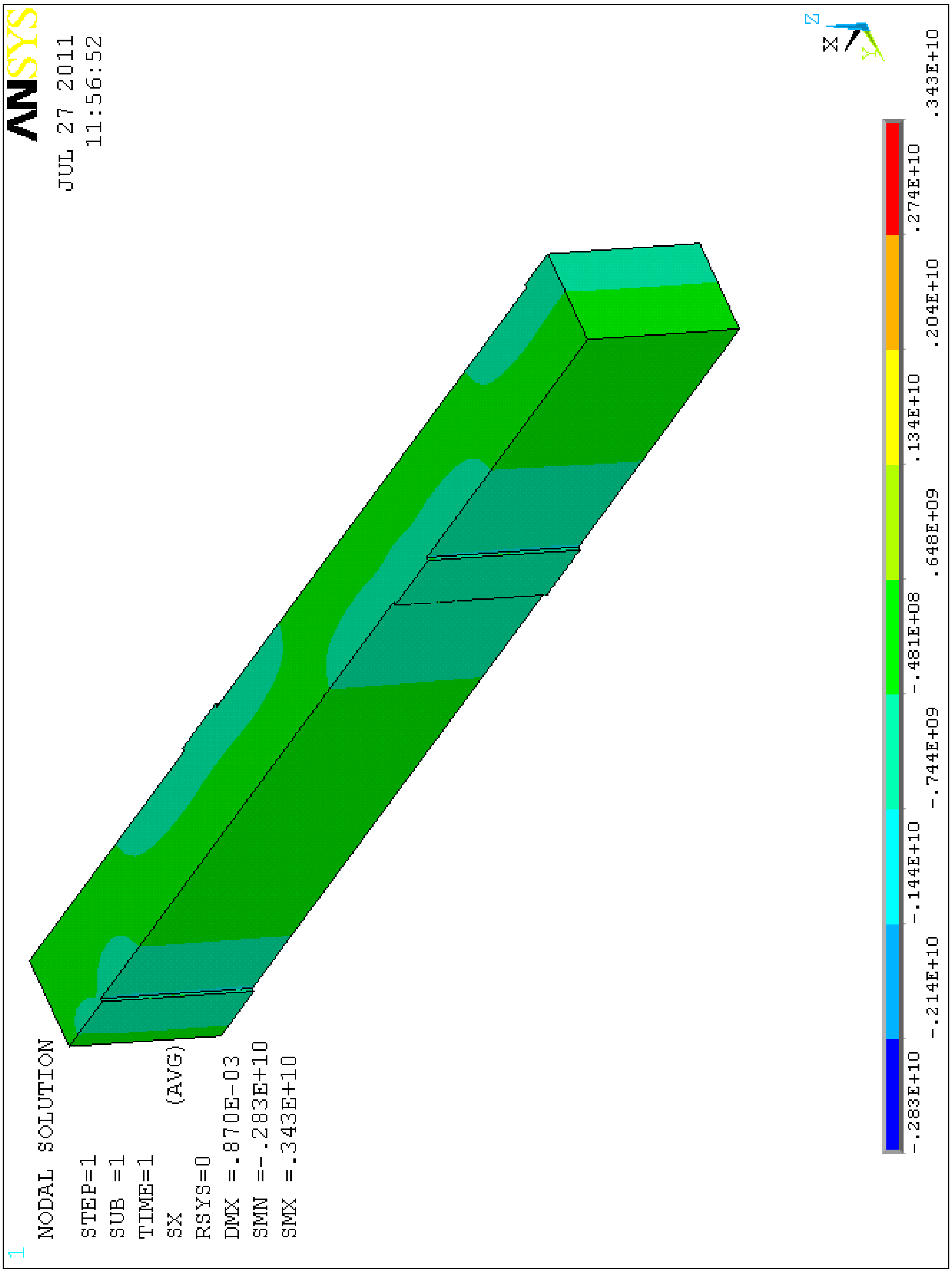

Figure 7-89: One of two paired wave keys bending stress (σ_{xx})

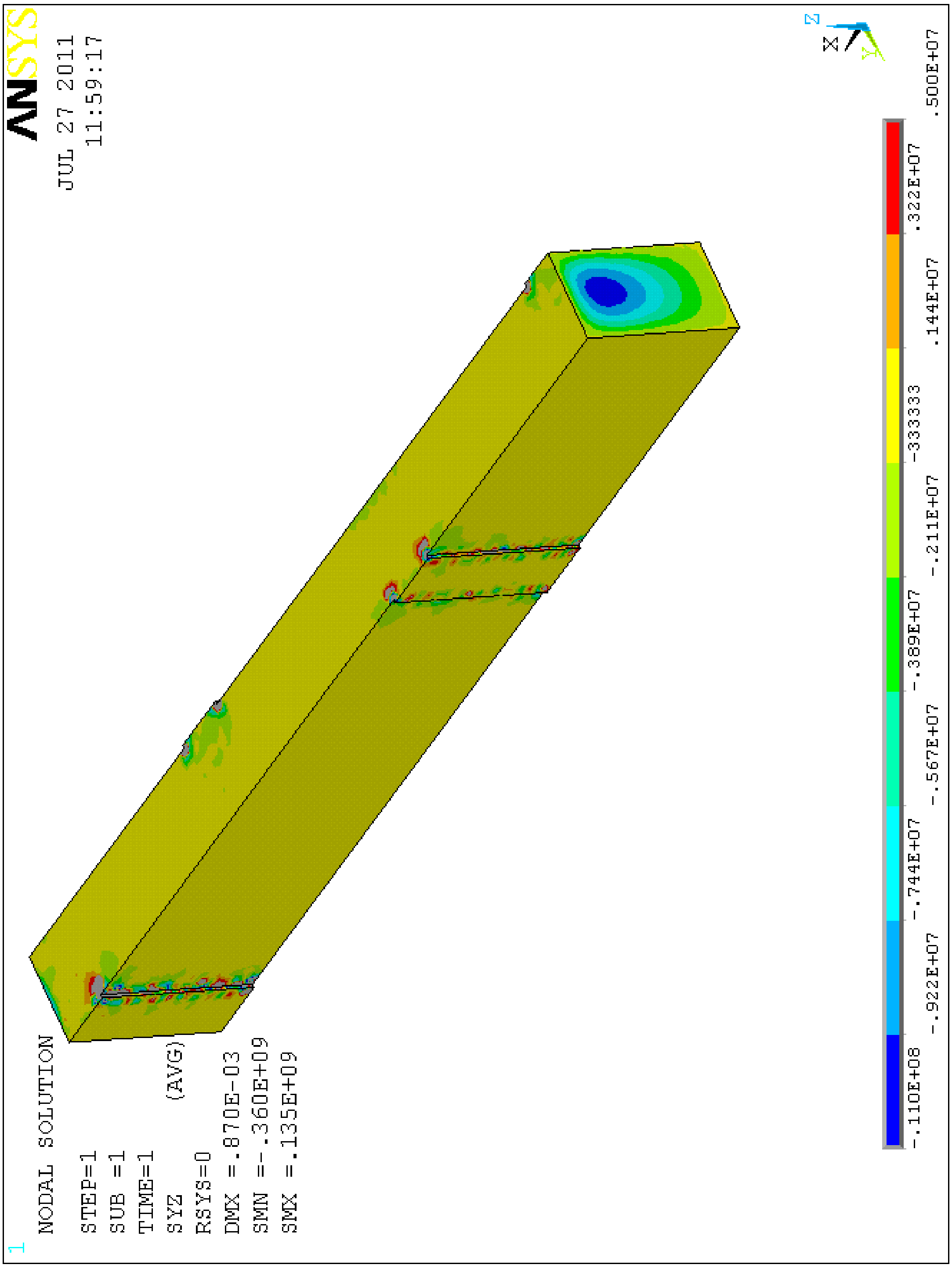

Figure 7-90: One of two paired wave keys shear stress (τ_{zy})

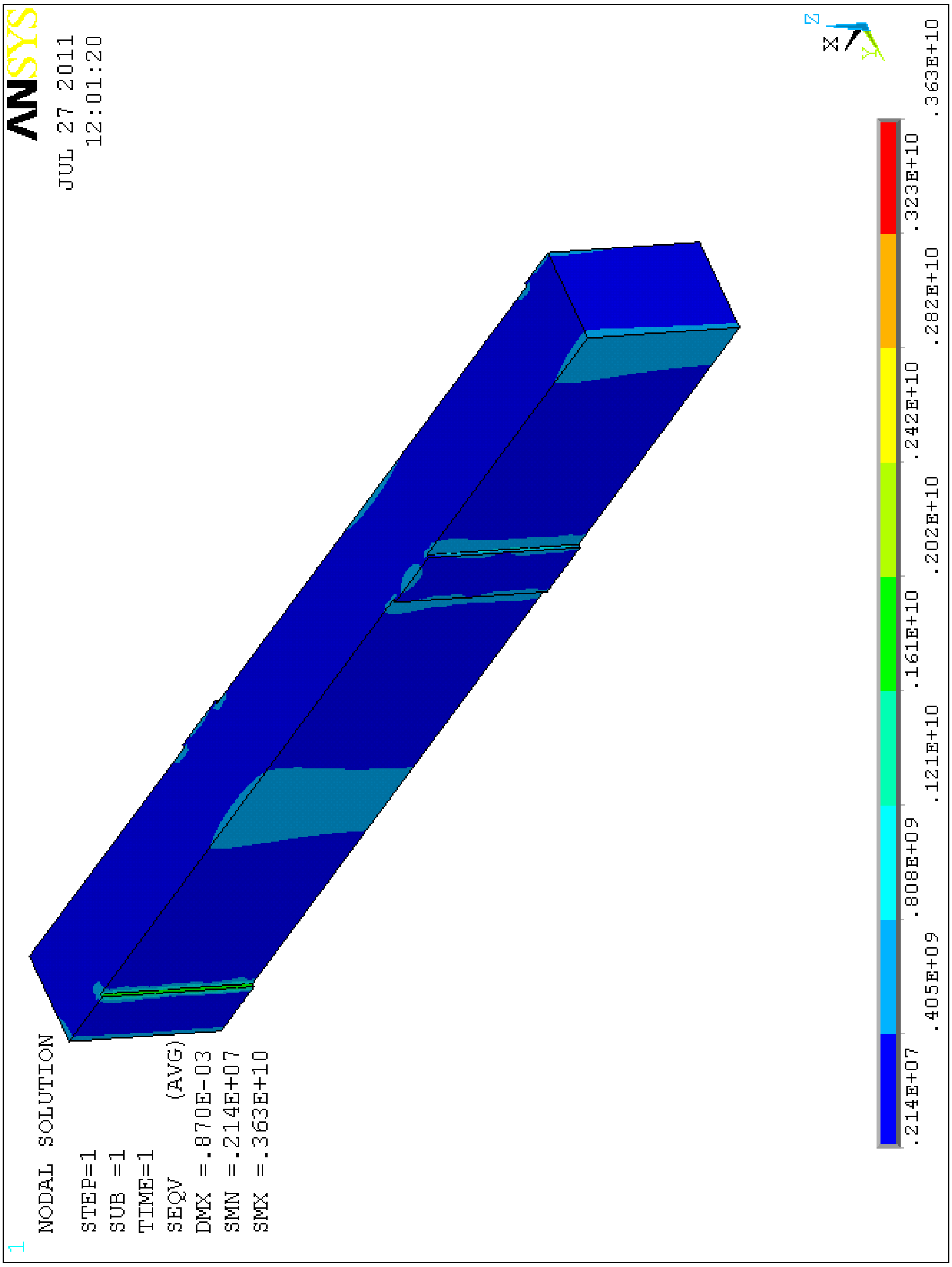

Figure 7-91: One of two paired wave keys von Mises stress

Table 7-16 compares the stress and stiffness values of the three torque wave key implementation designs again.

Table 7-16: Comparison of absolute peak stress values at cross section and stiffness values

Mechanical Property	Common design	Revised design	Paired key design
σ_{xx}	< 1.62e9 N/m^2	< 1.12e9 N/m^2	< 0.744e9 N/m^2
τ_{zy}	< 0.17e9 N/m^2	< 0.17e8 N/m^2	< 0.11e8 N/m^2
τ_{xy}*	< 0.20e9 N/m^2	< 0.20e9 N/m^2	< 0.13e9 N/m^2
von Mises	< 1.26e9 N/m^2	< 1.12e9 N/m^2	< 0.55e9 N/m^2
Stiffness (Mathcad)	4.664e8 N/m	--	--
Stiffness (FE)	5.3279e8 N/m	5.9149e8 N/m	1.3320e9 N/m
Bending at tooth	2 mm (bound. cond.)	1.802 mm	0.800 mm

Note: The spring stiffness (1.3320E9 N/m) is not exactly half of the value of the "revised design" (5.9149E8 N/m), which is caused by the coarse thickness estimation by using the Mathcad sheet.

Conclusion of torque wave keys

Even though von Mises stress is still above the yield point, the "paired key design" would be applicable. The flow chart in Figure 7-92 indicates again how the stresses were determined.

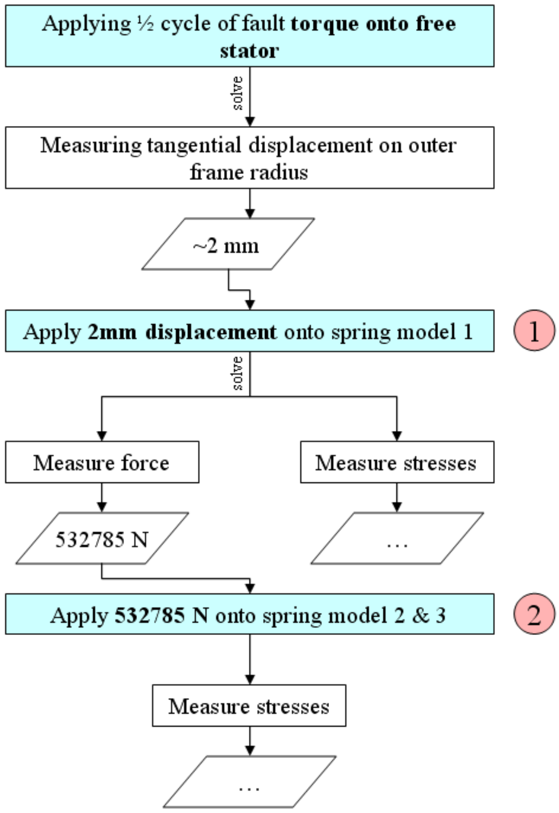

Figure 7-92: Flow chart of force application procedure

The steps marked with a red patterned circle contain uncertainties towards lower forces and consequently lower stresses (viz. calculated stress values are higher than in reality):

Circle 1: The 2 mm displacement occurs within the first half excitation cycle when the stator moves free. In reality the stator is attached over the spring to the concrete. Caused by the *higher* stiffness, the 2 mm displacement will never occur. So the decreased displacement will also decrease the force and consequently the stress of all posterior calculated springs.

Circle 2: If the stiffness is *low* enough, the force acting on the spring (and consequently on the soleplate) is much lower in reality than initially assumed, what is again a positive effect on the force and stress values in the wave keys. (Assumed is that the key geometry has not been changed. If the wave key is designed less stiff, the stress might increase – depending on the degree force reduction relative to the degree of downscaling).

With currently available calculation methods (available FE models and Mathcad sheet for the wave key), an iterative process is required to find an appropriate spring. The scheme is shown in Figure 7-93 and explained in the paragraph afterwards.

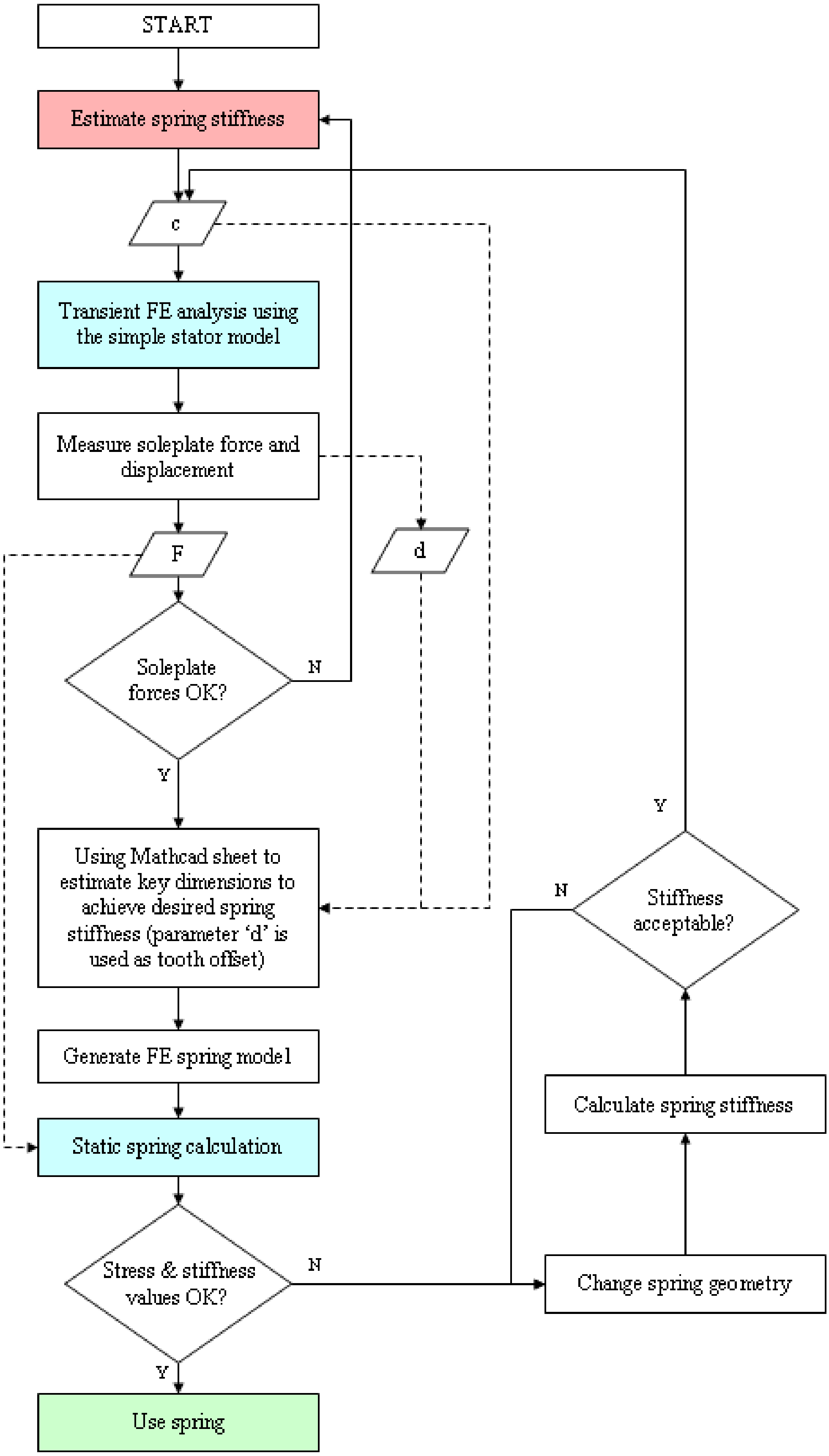

Figure 7-93: Iterative finding of appropriate spring geometry (solid lines: follow path, dashed lines: generate / use value)

The first rough estimation of the required spring stiffness can be achieved by using the chart of Figure 7-70 or the equations in Table 7-13. This spring stiffness is applied to the simple model, used for most of the previous FE calculations. So the soleplate reaction forces can be calculated in a transient calculation. If they are low enough, the Mathcad sheet can be used to find a wave key with an appropriate stiffness. For the tooth offset the maximal displacement of the FE model at the outer frame radius must be used. The now retrieved geometric values from the Mathcad sheet can be used to generate an FE model of the key. Applying the sole plate reaction force onto the key's teeth should lead approximately to the same deformation as in the previous FE calculation with the simple model with spring elements. (Differences are to be expected as the calculation in the Mathcad sheet is based on a simple beam). If the stress and actual stiffness values are acceptable, the spring can be used.

If the stress value i.e. is too high at the end, new spring dimensions must be found and its stiffness calculated. A new transient calculation must be performed to achieve the soleplate reaction forces which have changed due to the new stiffness.

This scheme might end up in an infinite loop, depending in which degree the stress reduction is influenced by the force reduction (weaker, thinner key) on the one hand and by the up scaling of key dimensions (higher stiffness and forces) on the other hand.

7.4.5 Slot Key

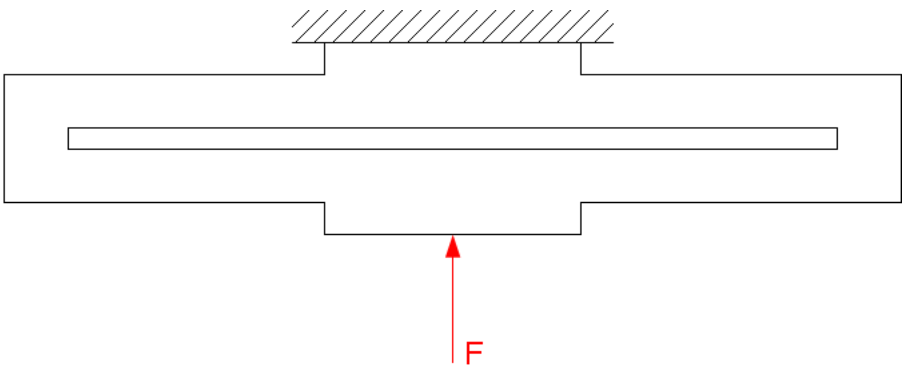

Figure 7-94: Scheme of a slotted soleplate key (top view)

This design is also easy applicable to the current soleplate design. A lower stiffness, compared to a wave key with the same outline geometries, can be achieved.

The critical points for this design are the stresses at the side edges of the slot and the bending of the contact surface (for the sake of convenience also named "tooth"). To reduce former, the edges of the slots are rounded.

Symmetry issues

Due to limited computer resources this FE model is calculated by making use of one its symmetric axes. Even though this spring has two geometric symmetry axes, only the vertical one can be used as the displacement is not symmetric. Figure 7-95 shows in its middle image the wireframe of the deformed spring (thick line). The thinner line in this image is the spring in its original state. It can be seen that the deformation (illustrated by the blue arrows) is not symmetric. This is why the horizontal symmetry axis can not be used.

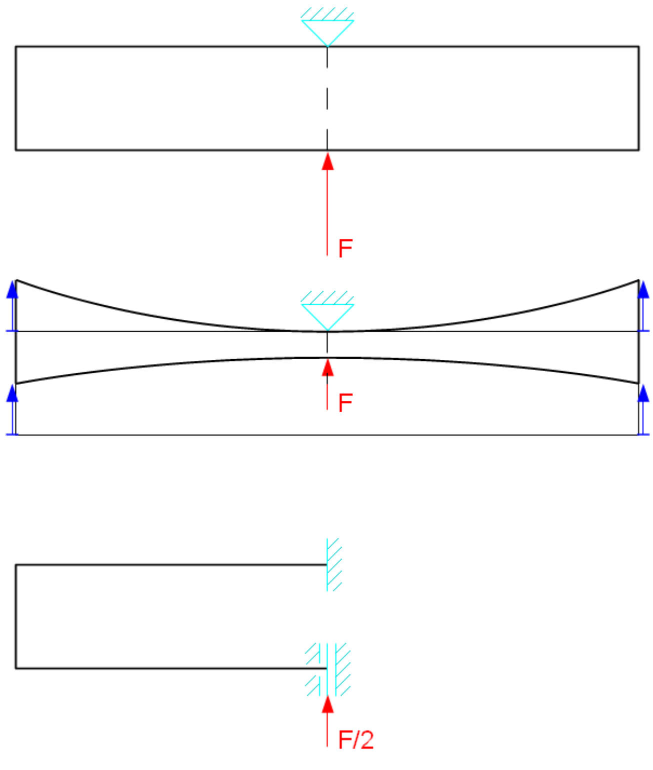

Figure 7-95: Wireframe models of slot spring: original state (top), deformed state (middle), boundary conditions for used symmetry (bottom)

The amount of deformation and the stress values are the same, but when calculating the stiffness, the total force value must be used ($c = (2 \cdot F/2)/s$).

Type of boundary condition: force or displacement

In the previous chapters, the maximal expected displacement was applied and the resulting reaction forces were used for subsequent calculations. This was possible because the teeth had a relative small width.

In this case this is just possible to a limited degree. The tooth for the slot key is much broader. If a displacement is applied, the nodal reaction forces would not spread homogenously over the surface but have a certain profile. If the summed value of reaction forces was applied homogenously (as pressure, like before in case of the torque wave keys) onto the tooth later on, it would result in a significant deviation of stress and stiffness values.

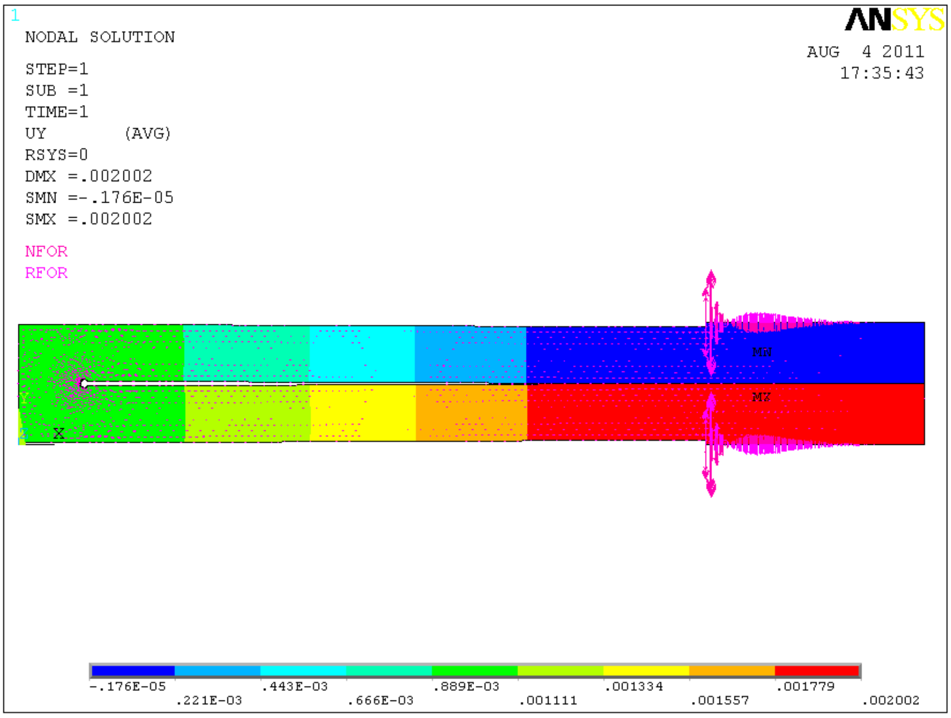

Figure 7-96: Force profile at tooth (purple arrows) if the BC are applied as displacement

The real behavior is predicted best by applying the same amount of displacement along the tooth. Again, 2 mm is used. The stiffer the spring is, the more inaccurate are the stress values (because the less likely 2 mm of displacement is approached). To be able to compare results, again the reaction force at the tooth in case of a 2 mm displacement of a reference spring is measured. This reaction force is applied homogenously onto the tooth surface of the following spring models, like it was done for the torque wave keys. This way stress values are good comparable, but stiffness values differ from the real situation.

The problem considering the dynamic behavior (reaction force increases if the stiffness increases) also exists like for the wave key. (Figure 7-93 in its basic form is also valid for this kind of spring).

Results and summary

Figure 7-97 shows the mesh of the FE model. It has been refined at those locations where high stress gradients were expected. The common element size is 6 mm – and in the area of the rounding, it's 0.5 mm.

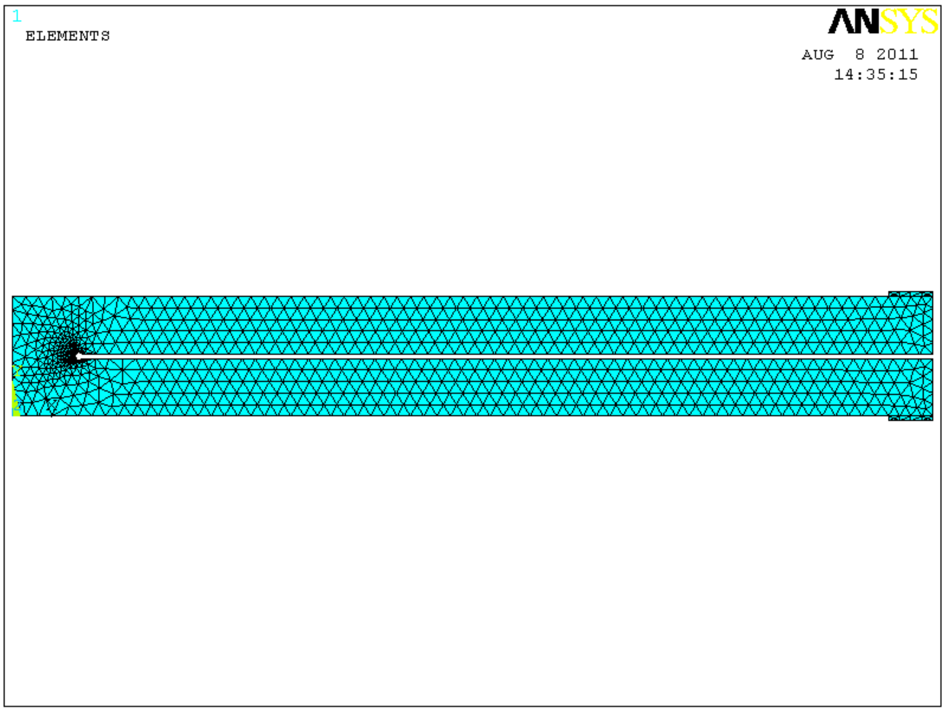

Figure 7-97: FE mesh of slot key (#10 in Table 7-17)

Table 7-17 shows the results of some parameter variations. The outline geometries are the same for all calculations (L=830 mm, W=54 mm, H=98 mm – symbols are explained in Figure 7-98).

This type of spring could be used for stators with a very high first natural frequency, as a relative low spring stiffness can be achieved with a large slot. Decreasing the slot increases the stiffness but declines the maximal von Mises stress (#2 and #3 in Table 7-17). von Mises stress in the slot rounding can be decreased by increasing the rounding radius (#4). But increasing the radius of the rounding has also a major effect on the stiffness.

A comparison of geometry #0 with #1 shows the major difference between applying force and displacement. The main reason is, as mentioned, the big width of the tooth, which causes a big force gradient over the whole tooth length (compare Figure 7-96). Like geometry #9 and #10 shows, this effect can be reduced by designing a tooth which is smaller in its width. As the force from the stator will not occur centric, a certain soleplate design must prevent the key of twisting.

Not only is the tooth width essential for the difference between applied displacement and force as boundary condition, but also the width of the gap. If the gap is too small, which means the stiffness at the location of the tooth is pretty high, the difference between applying force or displacement is high again (compare geometry #7 and #8).

Table 7-17: Parameter variation of slot key

#	T [mm]	O SW [mm]	SL [mm]	rad. [mm]	max. displmnt. [m]	maximal Stress [N/m^2]	Total force on tooth [N]	Stiffness [N/m]
0	200	2	770	2	2.00E-03 *	4.16E+08	1.17E+04	1.17E+07
1	200	2	770	2	2.74E-03	4.99E+08	1.17E+04 *	8.51E+06
2	200	2	700	2	1.97E-03	4.19E+08	1.17E+04 *	1.19E+07
3	200	2	400	2	3.18E-04	2.25E+08	1.17E+04 *	7.33E+07
4	200	2	400	4	3.44E-04	1.91E+08	1.17E+04 *	6.78E+07
5	200	2	200	4	3.56E-04	7.18E+07	1.17E+04 *	6.55E+07
6	40	2	200	4	1.03E-04	1.19E+08	1.17E+04 *	2.26E+08
7	40	2	48	4	5.41E-06	4.07E+07	1.17E+04 *	4.31E+09
8	40	2	48	4	5.41E-06 *	5.10E+07	1.37E+04	5.06E+09
9	40	2	770	2	2.00E-03 *	2.78E+08	6.10E+03	6.10E+06
10	40	2	770	2	2.00E-03	2.75E+08	6.10E+03 *	6.10E+06

*) Applied boundary condition

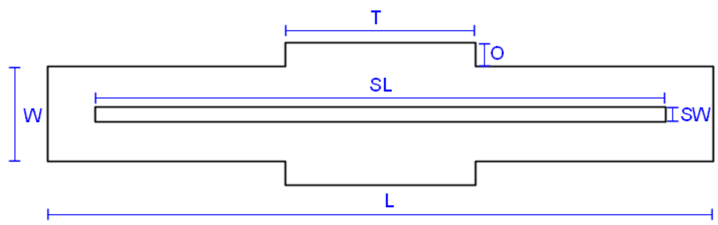

Figure 7-98: Parameter explanation for Table 7-17

Figure 7-99 shows von Mises stress of the reference spring (#0 in Table 7-17). The stress reaches its peak value at the gap rounding.

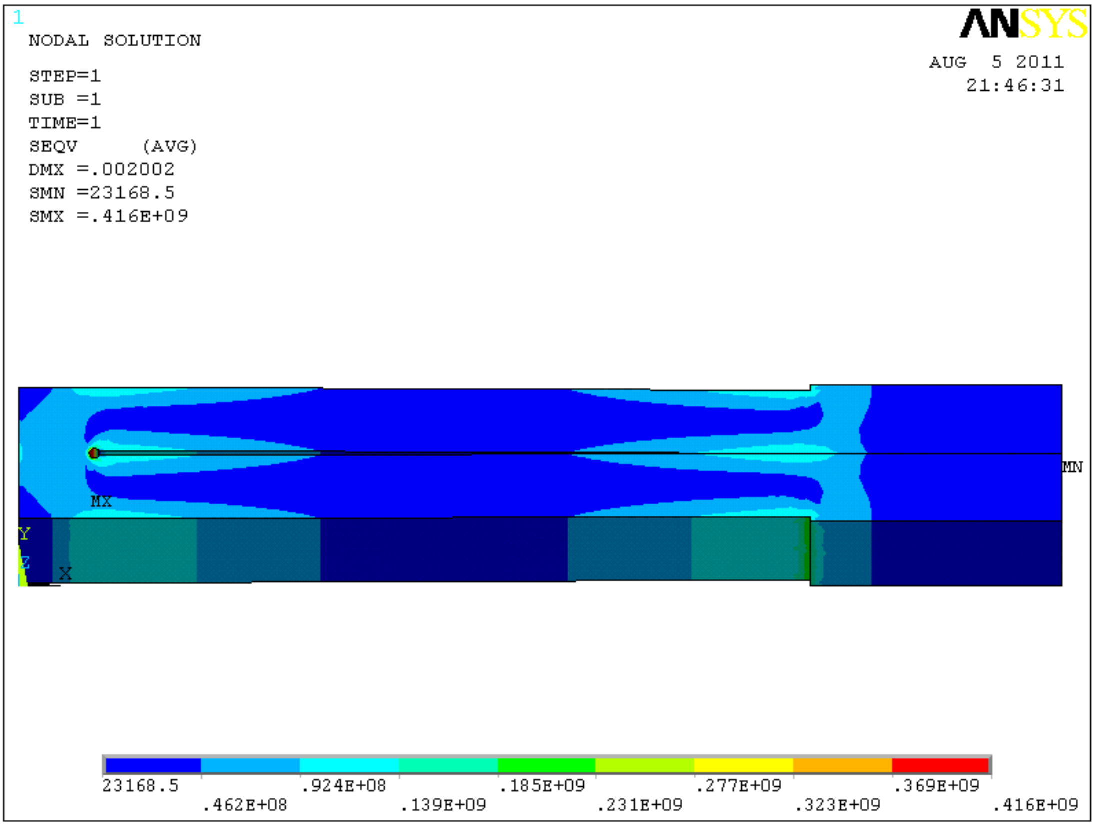

Figure 7-99: van Mises stress of the reference spring with 2mm displacement as boundary condition (#0)

7.4.6 Tangential Spring Plates

This spring concept is not based on the commonly used soleplate design.

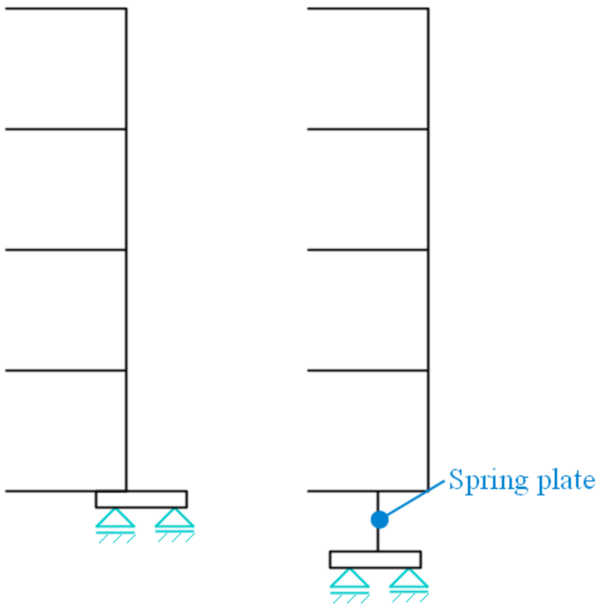

Figure 7-100: Commonly used soleplate scheme (left) and spring plate scheme (right)

This concept is based on a metal plate, applied between the adapter plate and the bottom shelf, like illustrated in Figure 7-100. Figure 7-101 shows a possible spring plate design. All dimensions (width, height, thickness, slot dimensions and slot amount) are variable for subsequent calculations.

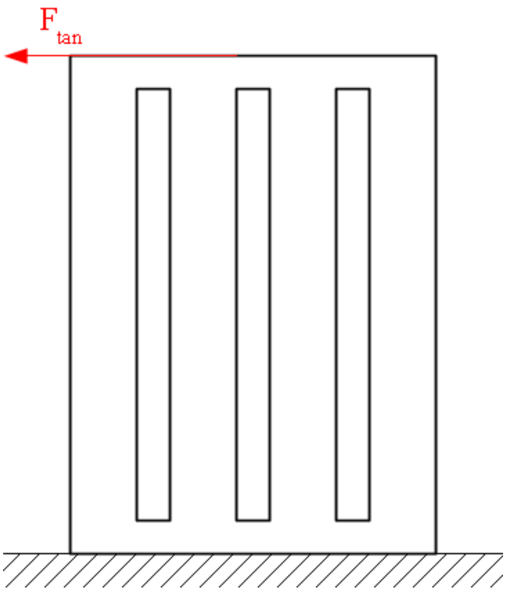

Figure 7-101: Possible spring plate design

The procedure to describe the mechanic behavior is as follows:

At first the tangential stiffness of the spring plate is calculated in a separate static FE calculation. Once the spring stiffness, which reduces the natural frequency to a desired value, is found, the spring plate is implemented into the simplified stator model. Again the values of Table 7-13 are used for this first stiffness estimation.

The FE model of the spring plate

The lateral spring stiffness of the plate is done by a 2-D FE calculation. For this calculation a cartesian coordinate system is used again, with the x-axis along the (tangential) length of the plate and the y-axis along its (axial) height. The spring plate is fixed on the lower end and the force of 1E6 N (in total) is applied on the other end. The displacement of the nodes where the force is applied is measured and an average value built. The average element size is 4 mm.

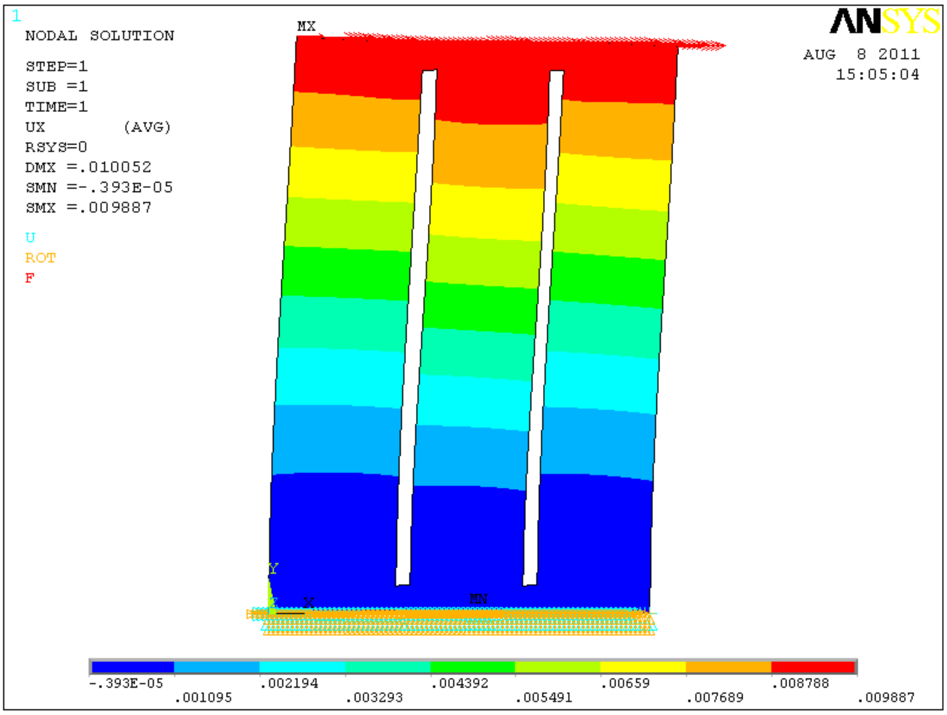

Figure 7-102: Displacement in x-direction (horizontal) due to applied force (#5 in Table 7-18)

As the applied force is actually a torque force, a small amount of force will act in z-direction (based on Figure 7-102). This causes a twist of the plate about its vertical axis. This effect becomes the more influential the smaller the assemble radius and the longer the plate is. Figure 7-103 illustrates this effect by means of a sketch. Figure 7-104 shows the FE model with the boundary conditions applied. (The applied force in this image is split in its cartesian components, whereas the force vectors in y-direction are enlarged for illustration reasons. Every 3rd node is plotted only.) The final effect can be seen in the contour plot of the FE calculation in Figure 7-105.

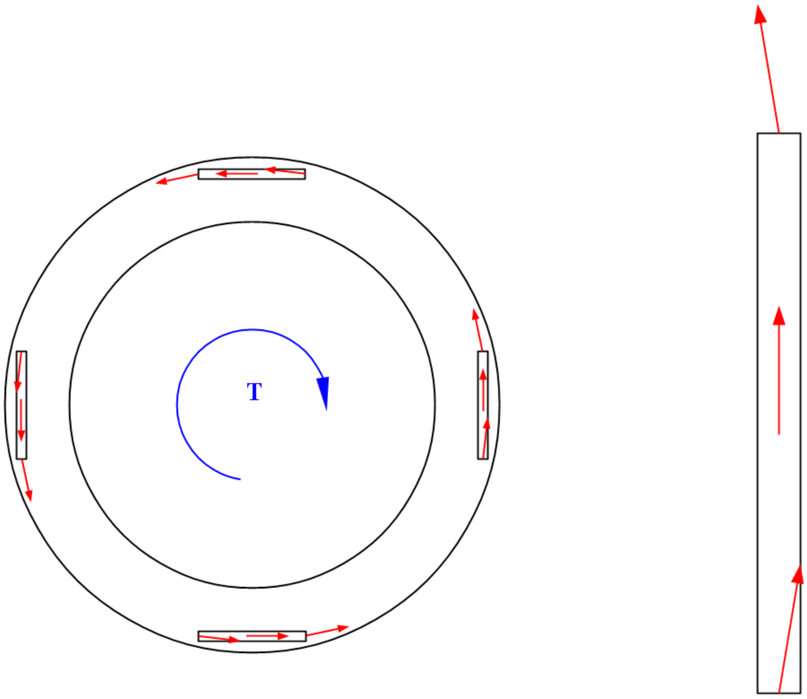

Figure 7-103: Left: bottom view of lower shelf with spring platens, torque (blue) and reaction force (red); Right: detailed bottom view of spring plate and reaction forces

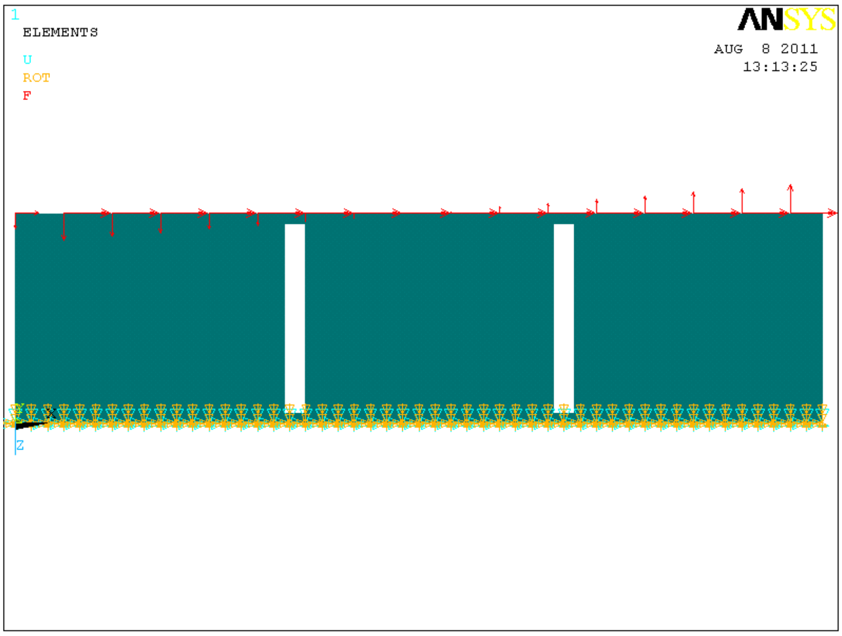

Figure 7-104: Boundary conditions for the case of force in y-direction is regarded

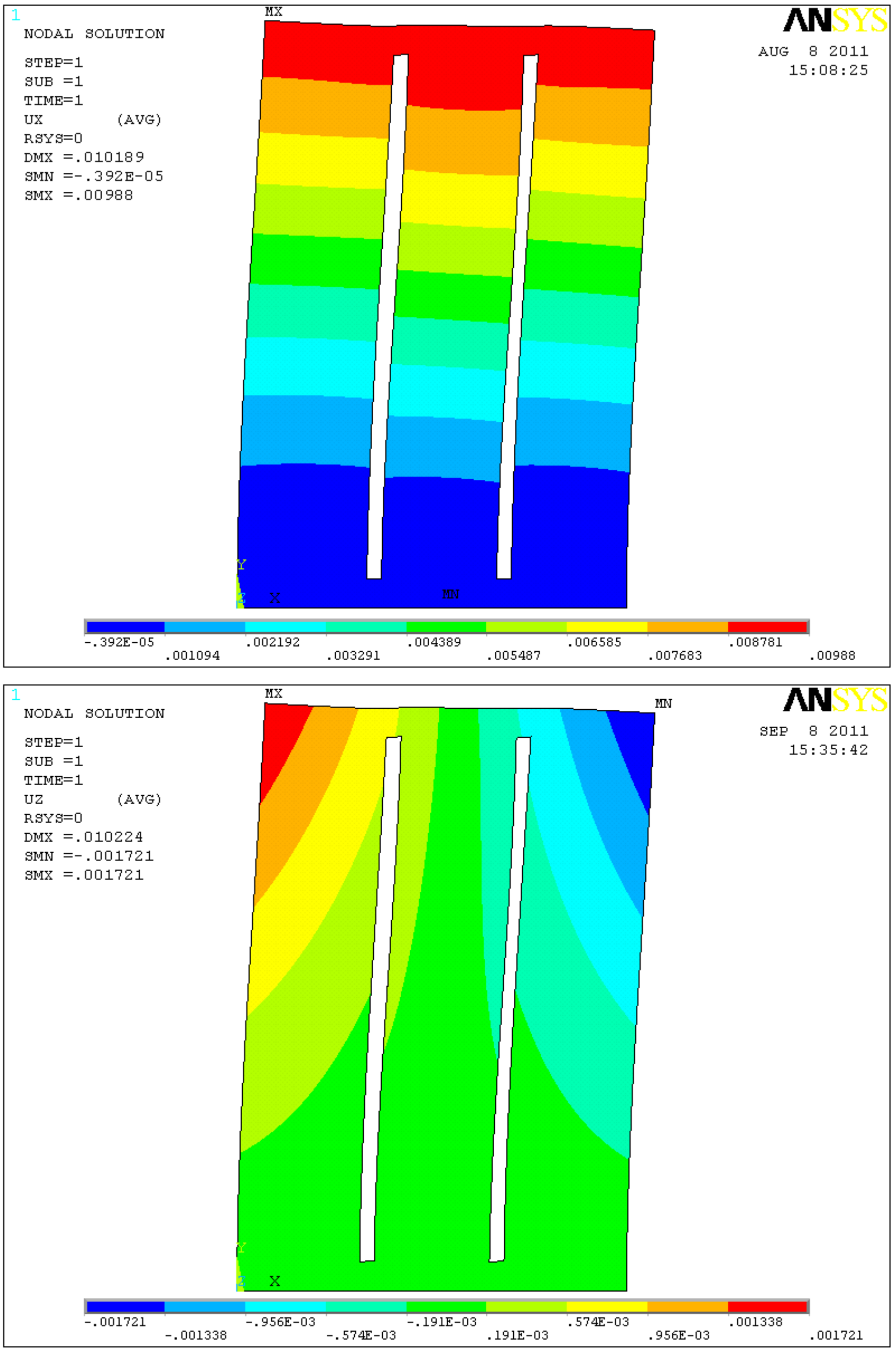

Figure 7-105: Displacement in x- and z-direction when regarding radial force component

The displacement in z-direction (shown in Figure 7-105) is less than 1/10 of the displacement in x-direction. This is also due to the much weaker stiffness in z-direction. The force relation on the very outside nodes of this particular soleplate is $Fx/Fz = 6236/416$ (based on an assumed radial spring plate location at 3 m). Even compared to Figure 7-102, the displacement in x-direction does not change significantly. These facts allow neglecting the force in z-direction, if the stiffness in x-direction is of note.

The spring plates with the appropriate stiffness are now attached to the stator as it is shown in Figure 7-103 and Figure 7-106. The radial location is defined to be exactly in the middle between the inner frame diameter and the wrapper (where the first soleplate node of the simplified model was; see also Figure 6-48).

In this particular case it is not possible to lock the axial and radial degree of freedom of the stator, as the spring plate is not cylindrical shaped and bending. The spring plate is fixed on its very bottom node row in x- and y-direction (according the cartesian coordinate system used for the static calculation before).

Example project: "Birkapili"

"Birkapili" was chosen as reference project because it is a relatively small generator, what minimizes the calculation time. The simplified stator model of "Birkapili" has its first natural frequency at 93.2 Hz. According to the equation in Table 7-13 the spring stiffness, to achieve a soleplate force reduction to 25% of the static reaction, is about 1.03913E8 N/m.

Table 7-18 lists different spring plate geometries with its appropriate stiffness. Geometric changes, related to the plate geometry listed one row before, are patterned grey.

Table 7-18: Parameter variation of spring plate geometry and resulting stiffness

#	Height [mm]	Width [mm]	Thickness [mm]	# of slots [-]	Slot height [mm]	Slot width [mm]	Stiffness [N/m]
1	600	400	30	3	540	10	7.29054E7
2	600	400	30	2	540	10	1.13430E8
3	600	400	20	2	540	10	7.56202E7
4	600	400	20	0	540	10	2.33421E8
5	600	400	30	2	540	15	1.03375E8

Geometry #5 of Table 7-18 is used for a modal analysis to see in what extend the natural frequency has been influenced. The analysis shows that the natural frequency drops to 27.1 Hz. The result of the modal analysis is shown in Figure 7-106, which shows a cross section of the deformed stator. The contour colors show the tangential displacement, which is relatively constant for the stator (→ 1st tangential mode shape). Numerical values not meaningful in this image, as it results from a modal analysis.

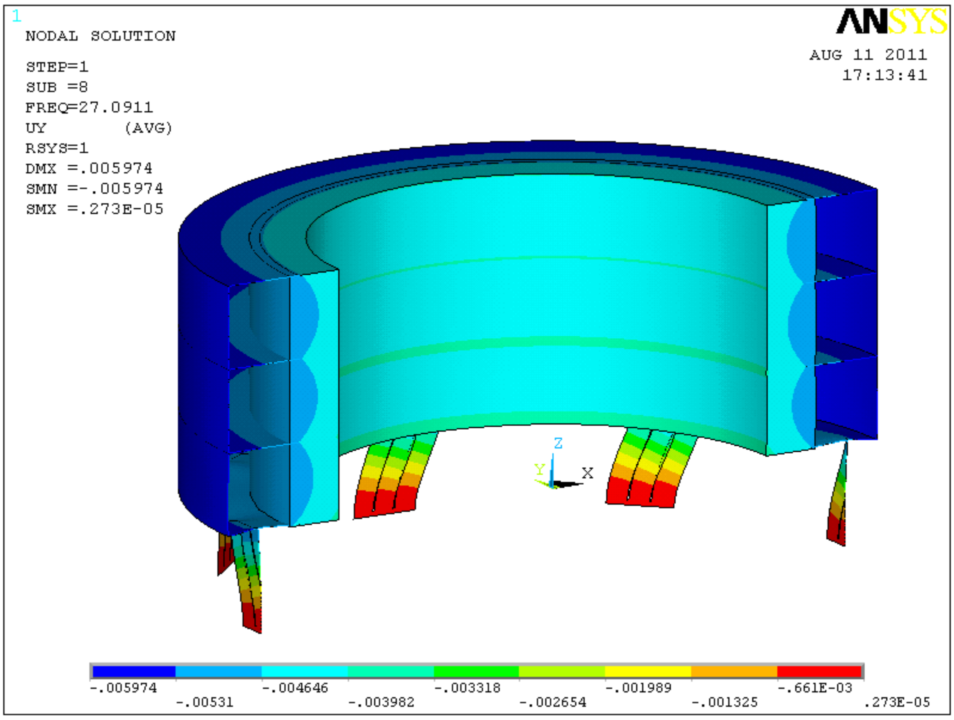

Figure 7-106: 1st torque mode of "Birkapili" with spring plates

Figure 7-107 and Figure 7-108 are the results of the transient calculation with the real faulty torque applied.

Figure 7-107 shows the nodal reaction force profile on the bottom of one single spring plate at a constant time of t=0.00119 s. On the abscissa the location of each node is plotted (0 is the center of the spring plate); on the ordinate is the force is plotted. It can be seen that most of the force is led into the concrete where the spring plate has its gaps.

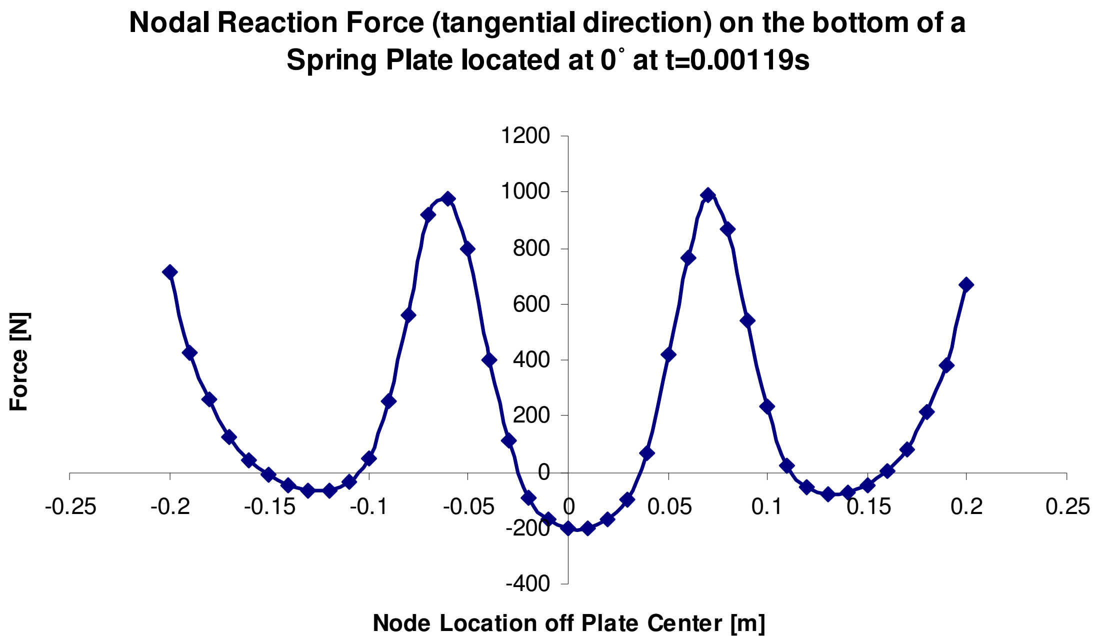

Figure 7-107: Force distribution at the bottom of one spring plate

Figure 7-108 plots the soleplate reaction force. Compared to the results of Chapter 7.3 (Table 7-14 on page 96 and charts on page 97ff.), which have also the same spring stiffness, results are slightly different. These differences are mainly caused by

- the different radial spring location,
- a slightly different spring stiffness and
- the 3-dimensional behavior of the spring plate.

To simulate the spring for the calculations in Chapter 7.3, FE spring elements were applied on the soleplate nodes, which have different radial locations (compare Figure 6-48). In this case the spring radius is constant (disregarding that the spring is straight and not bent).

The stiffness value, used for the calculation in Chapter 7.3, is exactly the value calculated by the equations of Table 7-13, whereas the value used here is just approached by the spring plate.

The spring elements of the calculation in Chapter 7.3 are just acting in the radial direction. But the spring plate in this case is able to move and bend in every direction. Furthermore, the stiffness calculation in this chapter was also based just on a 2-D FE calculation.

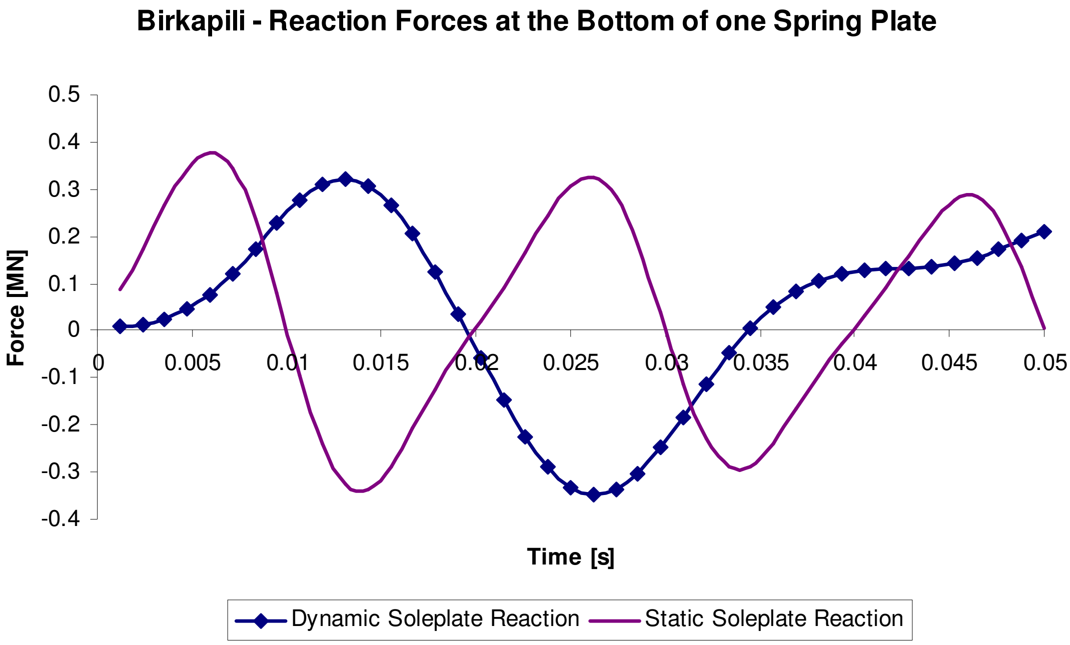

Figure 7-108: Tangential soleplate reaction force

It can be seen in the dynamic reaction forces in Figure 7-108, that the used spring stiffness is marginal. The transient peak forces are very close to the static ones.

The next figure shows the stress in the spring plate at the time when the peak force occurs (at t=0.013095 s).

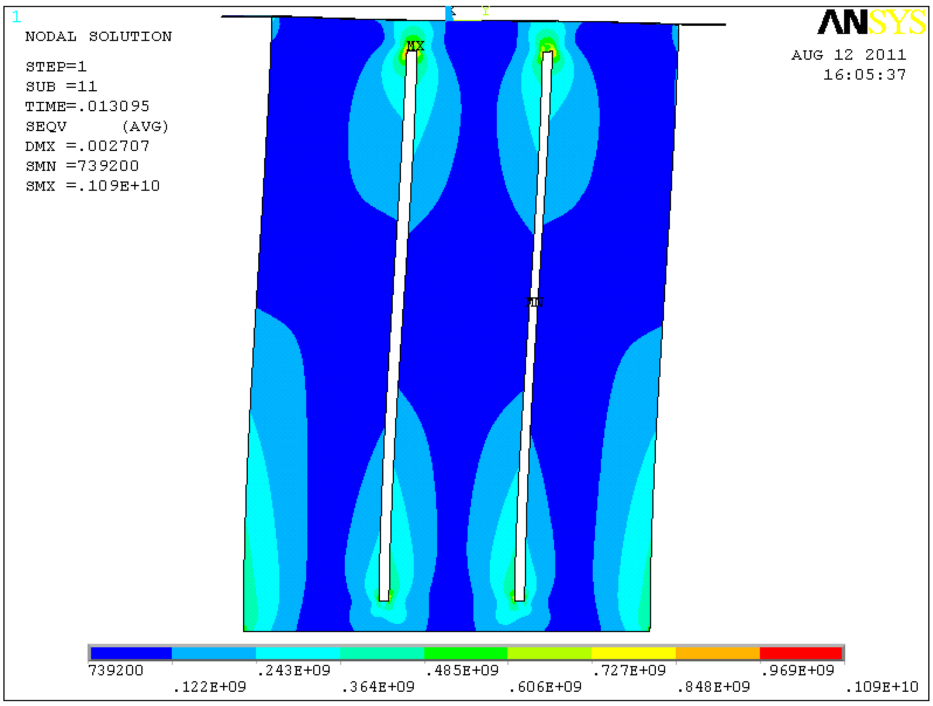

Figure 7-109: Von Mises stress of one spring plate at t=0.013095s

The stress values, shown in Figure 7-109, are above the yield point. Not regarded in this calculation is the additional axial stress due to the stators dead weight. But the gravity force is not very crucial; its value is relatively low compared to the faulty torques (see Figure 7-110). Regarding gravity even lowers the peak stress values in the gaps, but increases the overall stress situation slightly.

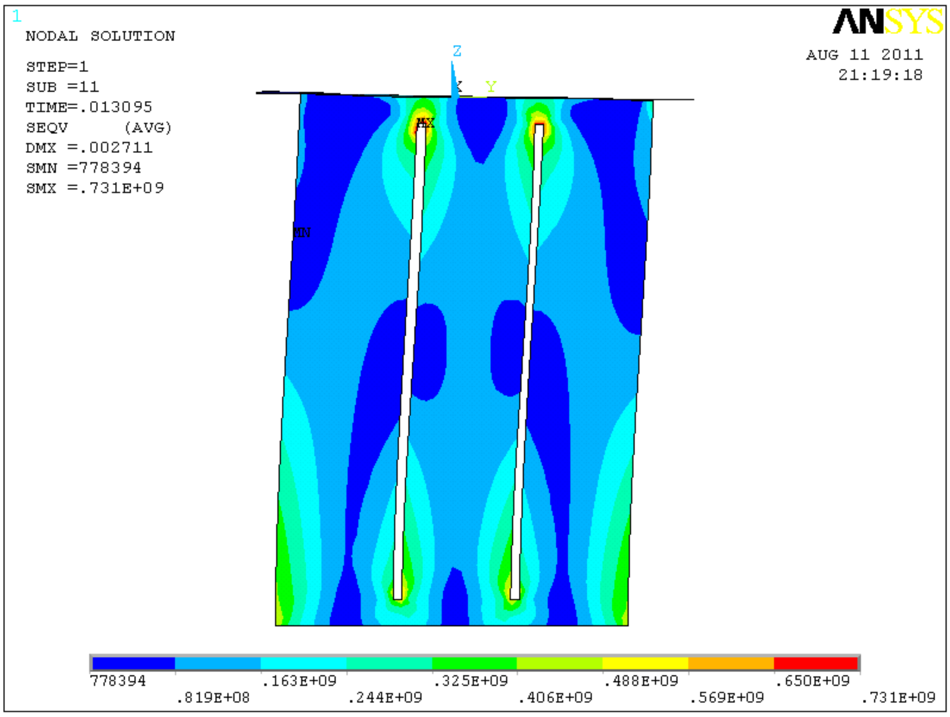

Figure 7-110: Von Mises stress of one spring plate at t=0.013095s, regarding gravity

To improve the structure, some more static calculations are done. Therefore the peak force (324,506 N) is applied on the top of the spring for the static calculations. It is important that the stiffness must not change significantly, as this force value would not be valid any more.

The following two images, resulting from the static FE calculation, have a closer look to the stress situation in the spring plate. The main occurring stresses are σ_{xx} and τ_{yx}. There are also some negligible forces in z-direction, resulting from the deformation.

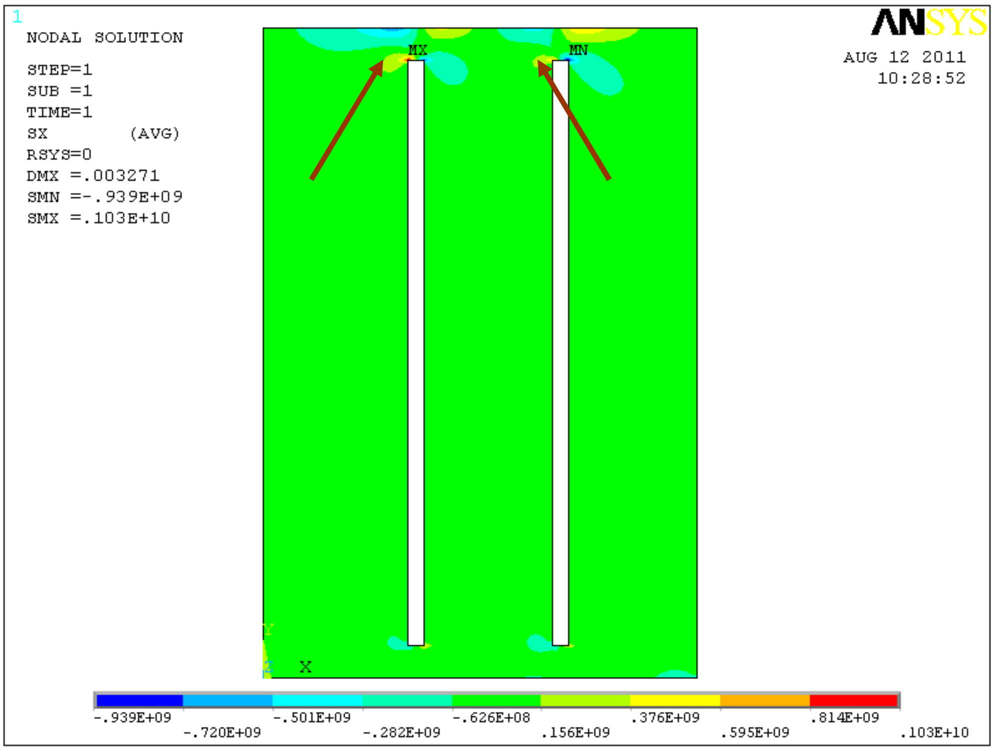

Figure 7-111: Tensile stress profile (σ_{xx}) of spring plate

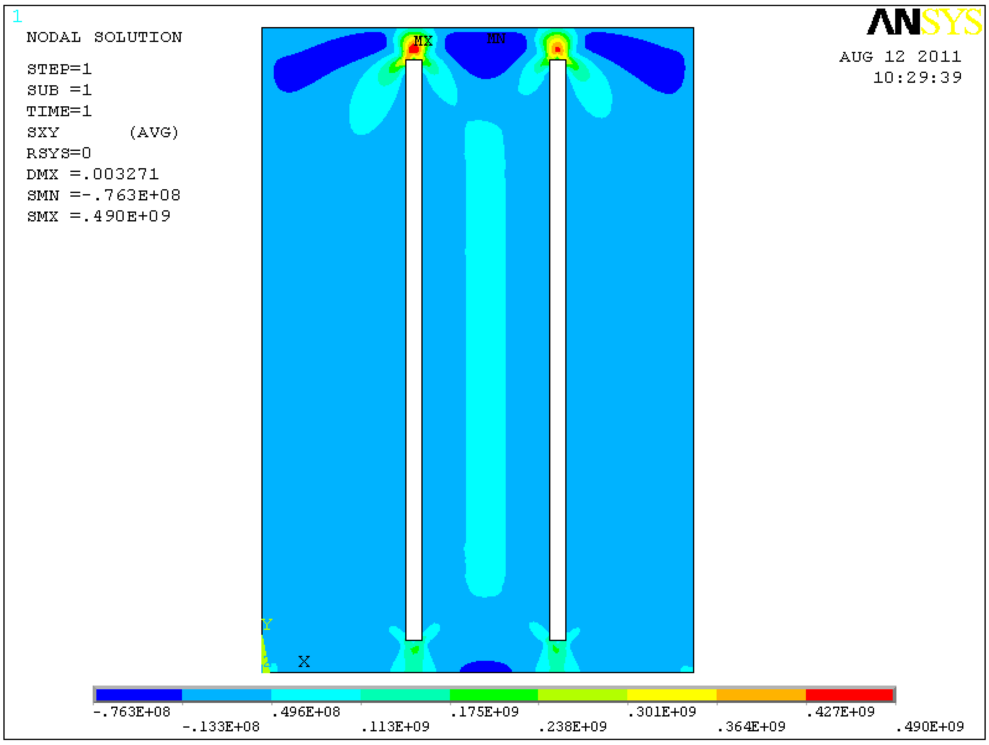

Figure 7-112: Shear stress profile (τ_{yx}) of spring plate

Tensile stress distributes relative all over the soleplate. There are stress peaks in the area of the top end of the slot (brown arrows), which can be reduced by rounding the gap ends. The peak value of the shear stress occurs also on the top end of each slot.

Stress can be reduced by:

- Increasing the sheet plate thickness
- Decreasing the slot height
- Increasing the plate width
- Decreasing the amount of slots

All of these mentioned ways to reduce stress unfortunately cause an increase of stiffness. The only way to decrease the stiffness without increasing stresses is to increase the height of the plate. For this particular case a height of 1300 mm and a thickness of 50 mm are required to achieve an acceptable stress situation without changing the stiffness properties significantly (see #1 in Table 7-19). Furthermore, low stress areas have been cut off to achieve this low spring stiffness. Anyway, these large dimensions are not desirable.

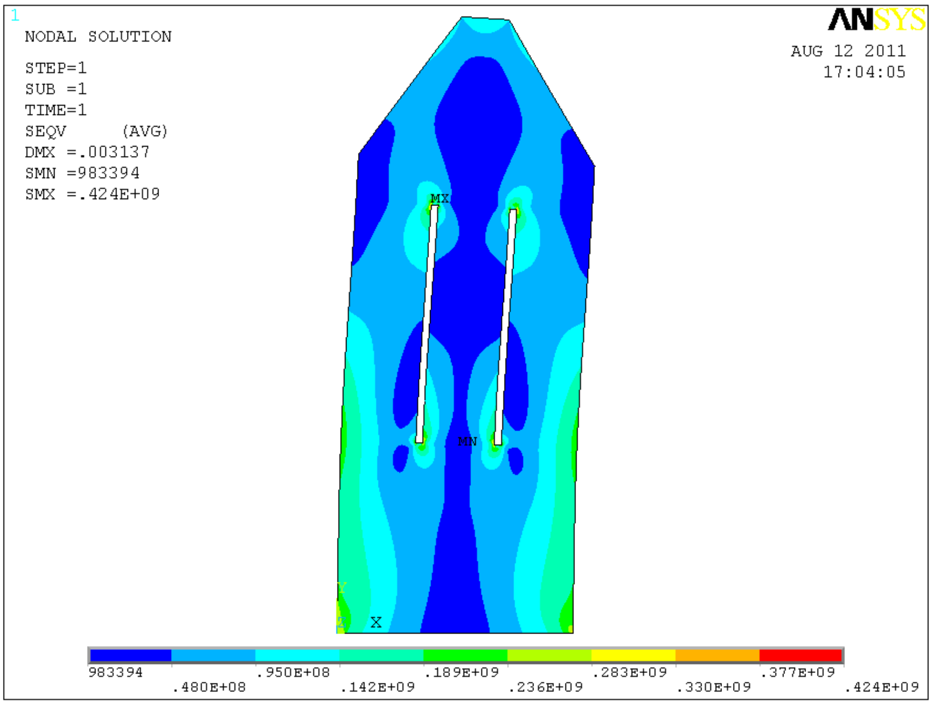

Figure 7-113: Von Mises stress for chamfered spring plate (#1 in Table 7-19)

Is it – under the space point of view – possible to increase the width of the spring plate, the design shown in Figure 7-114 would have very good stress and stiffness properties (#2 in Table 7-19). The long width allows distributing the force over a long distance, what results in stress reduction. The big amount of slots reduces the stiffness significantly. There are even more slots possible than shown in Figure 7-114, because the stress between the two gaps is very low.

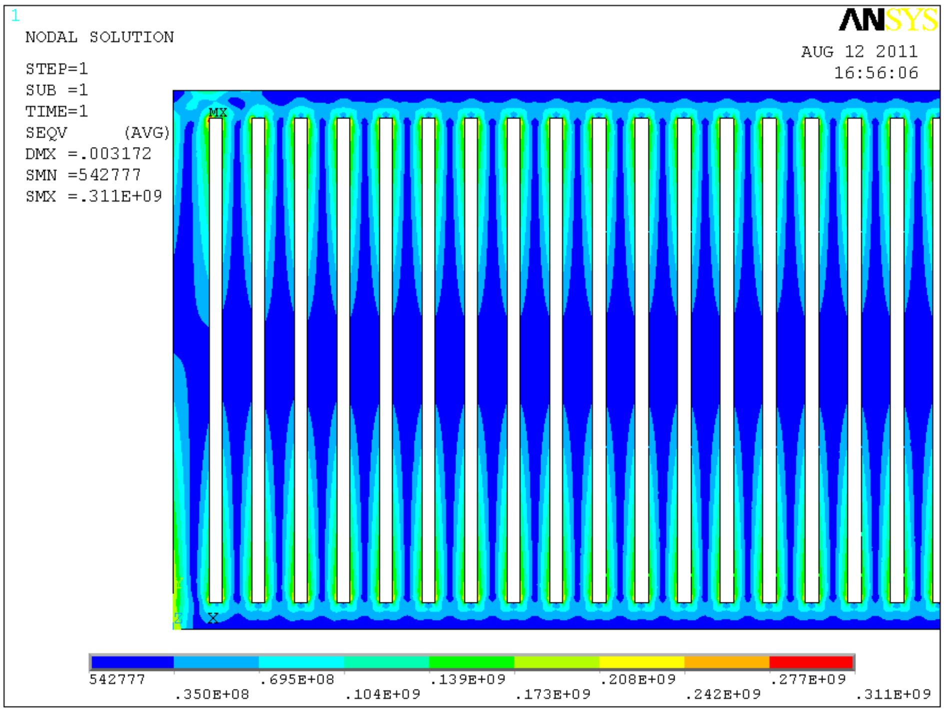

Figure 7-114: Von Mises stress for spring plate dimensions #2 in Table 7-19

Table 7-19: Possible spring plate dimensions for "Birkapili"

#	Height [mm]	Width [mm]	Thickness [mm]	# of slots [-]	Sl. height [mm]	Sl. width [mm]	Stiffness [N/m]
1*	1300	500	50	2	500	15	1.03701E8
2	590	2000	60	42	530	15	1.03542E8

*) Additionally chamfered top edges

Alternative design concepts

In this chapter it was assumed that the spring plate is attached to a radially guided soleplate. It is also possible to fix the spring plate directly to the concrete. This would solve one of the problems with the currently used, radially guided soleplates: When it comes to thermal expansion, the stator doesn't expand equally around its whole circumference. This results in an uneven air gap between the poles and the stator core, resulting in additional dynamic forces being applied to the rotor and stator structure. The radial stiffness of the spring plates would support the stator to keep its centric position.

Another design alternative would be to align the spring plate under a certain angle, instead of tangentially to the stator. This will cause lower spring stiffness in tangential direction, what allows designing the plate thicker and reducing the stress.

To solve the stress problem it is also possible to extend the lower shelf radially to attach the spring plate at a more outer radial location.

To save axial space it is also possible to align the spring plate horizontally, like shown in Figure 7-116. The axial load could be carried by a support, which is fixed to the lower shelf and has a low friction contact to the soleplate.

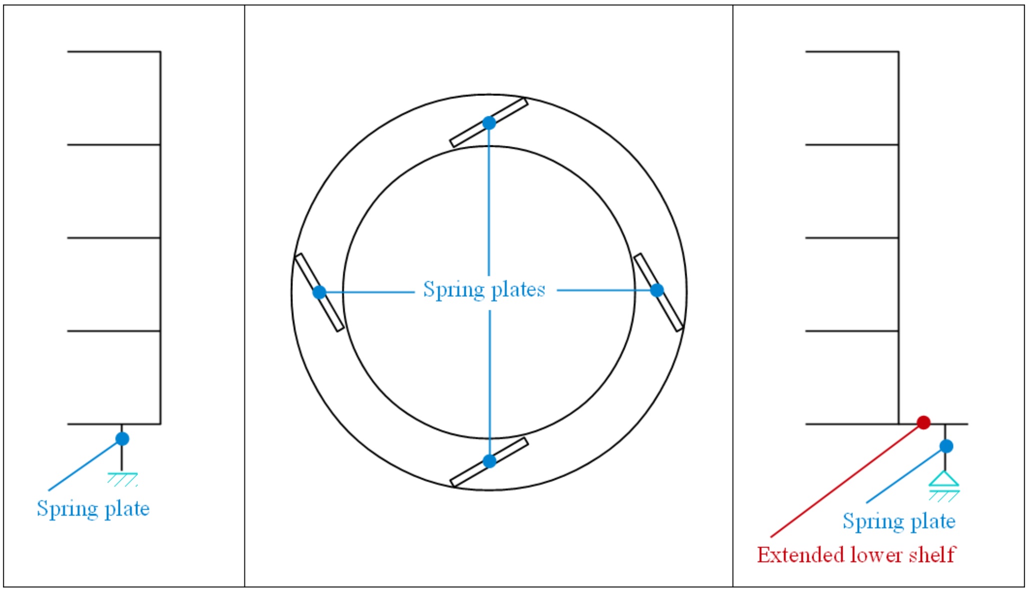

Figure 7-115: Alternative concepts: fixed plate (left), angled plate (middle), extended shelf (right)

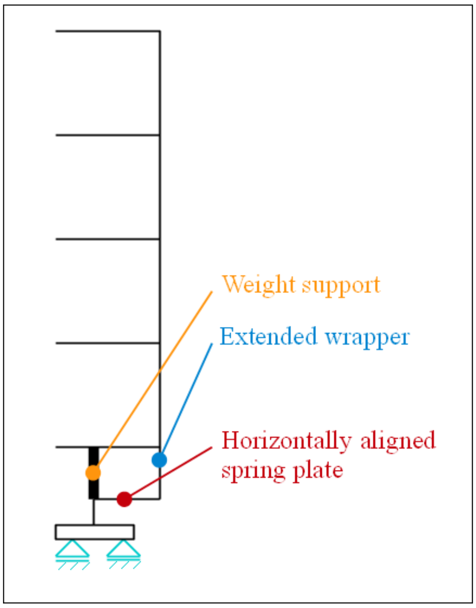

Figure 7-116: Alternative concepts: horizontal plate

8 Summary and Outlook

The initial modal analyses of the stator core and stator frame of all reference projects have already shown that the first mode frequencies are not low enough to achieve a significant force reduction. The first natural frequency of some reference projects is even very close to the dominating excitation frequency. Now the question arising was: How quickly will the reaction force build up in a case of failure? The dynamic faulty torque acts on the stator core for less than 0.05 seconds. Is this period of time enough to overcome all initial transient effects of the stator? Yes, it is: The following transient FE calculations have shown that within the first excitation cycle the reaction force on the soleplate is already higher than a static calculation, like it was performed so far, delivers. Though all these calculations were performed by the means of a simplified FE model, a modal and transient analysis of a solid CAD model have shown a very similar behavior. So the original expectation, that the soleplate reaction forces are lower when dynamic effects are regarded, could not be proved. An element of uncertainty not regarded in previous calculations is the connection between core and frame. For all hitherto calculations the core is rigidly connected to the frame. But in fact there is a small tangential gap at this connection. Regarding this gap worsens the situation even a little bit more. Calculations have shown that the gap is not wide enough to archive a force reduction. But as there is a gap, the frame can oscillate with its natural frequencies for a small period of time (when the core is not in contact with the frame), which consequently worsens the situation a little bit.

So the initial target (soleplate size and concrete force reduction) is only achievable by reducing the natural torque frequencies of the whole stator. The natural frequency can be slightly influenced by the amount of shelves, as the initially performed modal analyses have shown. But the better controllable way is to spring support the stator at the sole plates by using tangentially acting springs. The analyses of five possible spring designs, superficially looked at in this thesis, show that it is a tightrope walk to find an appropriate spring with a low spring constant which is still capable to bear the forces. Detailed analyses of these and other possible spring designs would be beyond the scope of this thesis. So a next step would be having a closer look on the spring designs. Depending on how much the natural frequency must be decreased, some of the analyzed springs have potential to be used (i.e. the paired torque wave key or the tangential spring plate angled aligned). Building up an FE model with the real spring geometry (like it has been done for the tangential spring plates) might be helpful to investigate the behavior of the spring designs based on the soleplate key. An automated, iterative process is also conceivable for the spring behavior investigation, where between the already existing simplified stator model and the static spring model is toggled.

Besides that it would be useful for further researches on this topic, if test results in tangential direction (acceleration / displacement of the stator core) of a short circuit test were available. Also researches on the real behavior of the core-to-frame connection could be helpful to retrieve meaningful results from future FE calculations.

9 List of Figures

10 Reference List

[1] Fink and Beaty, Standard Handbook for Electrical Engineers, 11 ed., McGrow-Hill, 1978.

[2] B. Schlegl, Konzeptstudie eines neuen Rotordesigns bei Hydrogeneratoren, Institut fuer Thermische Turbomaschinen und Maschinendynamik, TU Graz, 2010.

[3] R. Ingruber, Elektrotechnik M, WM, VT - Vorlesungsskript, Institut fuer elektrische Antriebstechnik und Maschinen, TU Graz, 2007.

[4] M. Schrittwieser, Numerische Untersuchung des Waermeuebergangs und der Stroemung von Statorschlitzmodellen, Institut fuer Thermische Turbomaschinen und Maschinendynamik, TU Graz, 2011.

[5] F. Schönleitner, Faserverbundwerkstoffe in Wickelköpfen, Graz: Institut für Leichtbau, TU Graz, 2010.

[6] C. Concordia, Synchronous Machines Theory and Performance, John Wiley & Sons, 1951.

[7] H. S. Kirschbaum, "Transient Electrical Torques," no. 64, February 1945.

[8] H. Dresig and F. Holzweissig, Maschinendynamik, vol. 9, Springer, 2009.

[9] [Online]. Available: http://home.arcor.de/maschinendynamik1/Skript/04.%20Freie%20Schwingungen%20-%20linear.pdf. [Accessed May 2011].

[10] Gross, Hauger, Schnell and Schroeder, Technische Mechanik 3, 8 ed., Springer, 2004.

[11] "Nyquist–Shannon sampling theorem - Wikipedia, the free encyclopedia," [Online]. Available: http://en.wikipedia.org/wiki/Nyquist-Shannon. [Accessed January 2012].

[12] "Nyquist-Shannon-Abtasttheorem – Wikipedia," [Online]. Available: http://de.wikipedia.org/wiki/Nyquist-Shannon-Abtasttheorem. [Accessed January 2012].

[13] A. Marn, Rotordynamik - Skriptum zur Vorlesung, 1 ed., Institut fuer Thermische Turbomaschinen und Maschinendynamik, TU Graz, 2010.

[14] C. C. Celigoj, Festigkeitslehre, Institut fuer Festigkeitslehre, TU Graz, 2004.

[15] M. Kaintz, "NGO Core Material Derivation," Andritz Hydro - Internal Report, 2007.

[16] F. Neumayer, "Bestimmung des Schubmoduls von Blechpaketen," Andritz Hydro - Internal Report, 2005.

Appendix A: Mathcad Calculation Sheet for Torque Wave Keys

SHRINK & TORQUE WAVE KEYS

CASTELLATED / WAVE KEY STIFFNESS

Contract: Mica $\qquad mm2in := 0.0393700787$

$L := \frac{830}{4} \cdot mm2in$ length of key between centerline of opposite nodes (inches)

$A := 40 \cdot mm2in$ length of node (inches)

$Wk := 98 \cdot mm2in$ key width (inches)

$Tn := 38.1 \cdot mm2in$ key thickness at node (inches)

$step := 2 \cdot mm2in$ key step (between nodes) (inches)

$Nn := 2$ Total number of nodes on side opposite side with end nodes

$E := 29000000$ Young's modulus of key material (psi)

$G := 12500000$ shear modulus of steel (psi)

$P := 1$ arbitrary load on node (lbs)

$a := .5 \cdot A \qquad b := .5 \cdot a \qquad tbn := Tn - step$

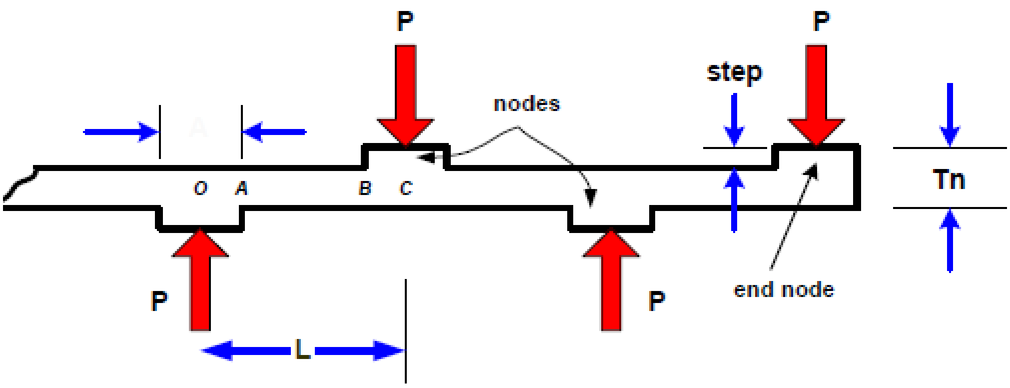

$I1 := \frac{1}{12} \cdot Wk \cdot Tn^3 = 1.085 \qquad I2 := \frac{1}{12} \cdot Wk \cdot tbn^3$

$y1 := \frac{P \cdot a^3}{3 \cdot E \cdot I1}$ section OA due to P

$$y2 := \frac{1}{2} \cdot \frac{P \cdot (L - a) \cdot a^2}{E \cdot I1}$$ section OA due to moment P(L-a)

$$\alpha A := \frac{P}{E \cdot I1} \cdot \left[\frac{1}{2} \cdot a^2 + (L - a) \cdot a \right]$$ rotation of sect OA due to load P and moment P(L-a)

$$y3 := \alpha A \cdot (L - a)$$ deflection at C due to rotation αA

$$y4 := \frac{P \cdot (L - a - b)^3}{3 \cdot E \cdot I2}$$ deflection at B due to P for section A-B

$$y5 := \frac{1}{2} \cdot \frac{P \cdot b \cdot (L - a - b)^2}{E \cdot I2}$$ deflection at B due to moment Pb

$$\alpha B := \frac{P}{E \cdot I2} \cdot \left[\frac{1}{2} \cdot (L - a - b)^2 + b \cdot (L - a - b) \right]$$ rotation at B due to P and moment Pb

$$y6 := \alpha B \cdot b$$ deflection at C due to rotation αB

$$y7 := \frac{P \cdot b^3}{3 \cdot E \cdot I1}$$ deflection of BC due to P

$$y := y1 + y2 + y3 + y4 + y5 + y6 + y7$$ total bending deflection

$$y = 6.522984 \times 10^{-6}$$

$$\alpha C := \alpha A + \alpha B + \frac{1}{2} \cdot \frac{P \cdot b^2}{E \cdot I1}$$ total end C rotation due to P

$$Km0A := \frac{E \cdot I1}{a}$$ rotational stiffness of beam section OA due to moment at A

$$KmAB := \frac{E \cdot I2}{L - a - b}$$ rotational stiffness of beam section AB due to moment at B

$$KmBC := \frac{E \cdot I1}{b}$$ rotational stiffness of beam section BC due to moment at C

$$Kmeq := \frac{1}{\frac{1}{Km0A} + \frac{1}{KmAB} + \frac{1}{KmBC}}$$ equivalent stiffness of beam due to moment at end C

$$Mo := \alpha C \cdot Kmeq$$ moment required at point C to cause rotation of beam end = αC

$$yA := \frac{1}{2} \cdot \frac{Mo \cdot a^2}{E \cdot I1} + \frac{Mo \cdot a \cdot (L - a)}{E \cdot I1}$$ deflection of OA due to counter-moment Mo

$$yB := \frac{1}{2} \cdot \frac{Mo \cdot (L - a - b)^2}{E \cdot I2} + \frac{Mo \cdot (L - a - b) \cdot b}{E \cdot I2}$$ deflection of AB due to countermoment

$$yC := \frac{1}{2} \cdot \frac{Mo}{E \cdot I1} \cdot b^2$$ deflection of BC due to counter-moment Mo

$$ys := \frac{6}{5} \cdot \frac{P}{G} \cdot \frac{1}{Wk} \cdot \left(\frac{a}{Tn} + \frac{L - a - b}{tbn} + \frac{b}{Tn} \right)$$ shear deflection of beam

$$ytotal := y - yA - yB - yC + ys$$ total beam deflection

****

*** TOTAL KEY STIFFNESS (FULL LENGTH OF KEY)

$K := 2Nn \cdot \frac{P}{ytotal}$ $K = 2291394$ lbs/inch

$K\_metric := K \cdot 17.8579673 \cdot 9.81 = 4.014 \times 10^{8}$ N/m

*** Force to deflect key wave = step (F)

$F := step \cdot K$ $F = 2 \times 10^{5}$ lbs

$Fo := \frac{F}{Nn}$ $Fo = 90212.4$ lbs

*** KEY STRESS

The Key Stress calculation assumes that the deflection of the key between nodes is equal to the dimension "step"

*** Stress in key at center of node (σ0)

$\sigma 0 := \frac{1}{8} \cdot (Fo \cdot 2 \cdot L) \cdot \frac{Tn}{2} \cdot \frac{1}{I1}$ $\sigma 0 = 127341$ psi

$\sigma 0\_metric := 6894.75729 \cdot \sigma 0 = 8.78 \times 10^{8}$ N/m^2

max ca. 0.2e9 N/m^2

*** Stress in key at end of node (σ0)

$M := \frac{1}{8} \cdot Fo \cdot (-4 \cdot a + 2 \cdot L)$ $M = 148726$

$\sigma A := M \cdot \frac{tbn}{2} \cdot \frac{1}{I2}$ $\sigma A = 114498$ psi

****

Appendix B: Structure and Description of used APDL Files

The FE calculation files (APDL text files with the file ending .inp) used for this thesis, might be helpful for further development at Andritz Hydro. This appendix explains the structure and usage. Basic APDL knowledge is required.

Root directory

The root directory contains the following folders:

- ANSYS
- Project_Data
- Shear_modulus_Core
- Spring_Stiffness
- Thesis
- Torque_Calculation

The folder ANSYS contains all APDL files and some archived ANSYS result files. The content of this folder is treated in this appendix. Besides this folder, some other folders are located in the root directory, briefly explained in the next few lines:

Project_Data contains geometric data from "Mica". Geometric data from every other project were retrieved from the printed E120 sheets.

In Shear_modulus_Core files, which contain information about core properties, can be found.

Spring_Stiffness contains the Mathcad file for the torque wave key stiffness.

The folder Thesis contains a digital version of this diploma thesis.

Torque_Calculation contains Mathcad sheets to calculate faulty torque equations.

/ANSYS/

As mentioned before, the folder ANSYS is the folder where all FE calculation files are stored. It contains following the subdirectories:

- Full_Model
- Simplified_Model
- Simplified_Quarter_Model
- Soleplate_Spring_FE

All of these subfolders contain APDL files and further subdirectories, like wkdir, transient_forces and geometries. Some of these folders contain also subfolders named archive and evaluation_files.

The following pages describe all major directories and files, with the main focus on the Simplified_Model directory.

/ANSYS/*/wkdir/

The working directory of ANSYS must be set to this folder. Otherwise relative file paths in the APDL files might be wrong.

/ANSYS/*/archive/

This folder contains saved .db and .rst files of some calculations.

/ANSYS/*/Evaluation_Files/

The major content of this folder are Excel files with calculation results and charts. Their filename should be representative for their content.

/ANSYS/*/transient_forces/

This folder contains the faulty torque equations (originally generated by the Mathcad files in the directory /Torque_Calculation/), readable for ANSYS. Each project has its own file. At the beginning of each FE calculation the torque equation file of the appropriate project is copied and renamed to Current_Job.inp.

/ANSYS/*/geometries/

The files in this folder contain the geometric dimensions of each project. Depending on which calculations were performed with which machine, some files may contain more or less parameters than others. Birkapili.inp, for example, also contains parameters for a soleplate spring.

These files also include the command to copy the appropriate faulty torque equation file to Current_Job.inp, mentioned before.

/ANSYS/Simplified_Model/START_*.inp

The file structure for the calculation is more or less a modular concept. Every calculation is started by a file whose filename starts with START_. These files load for the calculation

required files. As some procedures are the same or similar for every type of calculation (i.e. the building of the core or frame), this modular concept has its benefits.
To choose which machine is to be calculated, the appropriate line for the loaded geometry file must be uncommented in the START_*.inp file.
The general structure for most of these START_*.inp files is:

1. Set mathematical constants
2. Load geometric values
3. Calculate required geometric, mechanical and FE specific parameters
4. Build core
5. Build frame
6. Connect core and frame
7. Apply BC and start calculation
8. Post processing

This structure may vary, depending on the type of calculation. For instance, step 4-6 may be together in a separate file in some cases.
The following paragraphs describe the use of each *START_*.inp* file.

/ANSYS/Simplified_Model/START_CORE.inp

This file calculates the <u>modes of the stator core</u> or performs a <u>frequency response analysis</u>. By (un-)commenting line 21 (lock_frame_connection.inp) the modes of either the free core, or the core connected to an infinite stiff frame can be calculated. By (un-)commenting line 27 or 28 either a modal analysis or a frequency response analysis can be performed.
The post processing has to be done in the GUI.

/ANSYS/Simplified_Model/START_FRAME.inp

By the help of this file a <u>modal analysis of the frame</u> can be performed.

/ANSYS/Simplified_Model/START_CORE_MODAL_regards_frame_stiff.inp

This START file performs a <u>modal analysis where the frame's stiffness and mass is regarded</u> by springs and mass elements, applied on the outer radius of the core.
In a first step the frame is built and its stiffness calculated (get_frame_stiffness.inp). The stiffness values are saved and are applied onto the core (stator_spring_connection.inp) in a new calculation.

The post processing has to be done in the GUI.

/ANSYS/Simplified_Model/START_CORE_FREQRESP_regards_frame... .inp

Similar to START_CORE_MODAL_regards_frame_stiff.inp, this file performs a frequency response analysis of the core with the frame properties applied. The solution parameters for this analysis can be set in the file core_freqresp_regards_frame_stiff.inp. This calculation was never used in this thesis.

The results are written into a .csv file, saved in the working directory.

/ANSYS/Simplified_Model/START_MODAL_core_and_frame_connected.inp

This file is for calculating the modes of the whole stator, where the core and the frame are rigidly connected. The core and the frame, their connection and the soleplate nodes are generated in the build_frame_and_core.inp file. This file contains the parameter relConnectionOffset, which is necessary for the proper core-to-frame (solid-to-shell) connection. Its value indicates how far the shelves reach into the core.

Concerning the concrete connection (whether it is rigid or spring supported), both cases are possible. Either a rigid soleplate connection or a spring supported connection can be established by (un-)commenting line 31 (soleplate_spring.inp). The spring stiffness has to be set in the file soleplate_spring.inp. Generally, the required input stiffness value is the desired *global torque stiffness*, but this can easily be modified in this file.

The post processing has to be done in the GUI.

/ANSYS/Simplified_Model/START_FREQRESP_complete_stator.inp

Similar to START_MODAL_core_and_frame_connected.inp, this file calculates the frequency response of the whole stator. Again, by (un-)commenting line 24 soleplate springs can be regarded or disregarded. Solution parameters can be changed in freqresp_compl_stator.inp.

The results are written into a .csv file, saved in the working directory. This output file contains the following values, ordered by their column:

1. Soleplate node number in ANSYS
2. Radial location of the soleplate node
3. Tangential location of the soleplate node
4. Nodal reaction force amplitude
5. Frequency

6. Applied torque on the inner core radius

/ANSYS/Simplified_Model/START_STIFFNESS.inp

This file calculates the stiffness at the inner core radius of the whole stator (when core and frame are connected).

The results are written into a .csv file, saved in the working directory. This result file contains the tangential displacement, the applied force and the resulting stiffness for each node on the inner core radius.

/ANSYS/Simplified_Model/START_TRANSIENT.inp

A transient analysis of the whole stator can be performed by loading this file. In line 6, the parameter calcType can be set. If this parameter is set to 1, a transient analysis of the core (with an infinite stiff frame) can be performed. The results of this calculation are not significant for this thesis. So this calculation type has not been further developed or updated. So it can not be ensured that this calculation runs without any problems. There is the same situation when the parameter is set to 2, where the frame is just regarded by spring and mass elements. The transient calculation with the whole stator can be performed if the parameter is set to 3, which is the recommended setting for this parameter.

By (un-)commenting line 56 (soleplate_spring.inp) the soleplate support type (spring or rigid) can be changed.

The results are written into a .csv file, saved in the working directory. This output file contains the following values, ordered by their column:

1. Soleplate node number in ANSYS
2. Radial location of the soleplate node
3. Tangential location of the soleplate node
4. Nodal reaction force amplitude
5. Time
6. Applied force on the inner core radius

If line 58 (get_spring_stretching.inp) is not commented, the stretching of each soleplate node spring element is outputted in a separate .csv file in the working directory.

/ANSYS/Simplified_Model/START_TRANSIENT_GAP.inp

This transient calculation regards the tangential gap between the stator core and the key bar.

The format of the outputted .csv file is the same as for the normal transient calculation.

/ANSYS/Simplified_Model/START_MODAL_SPRING_PLATE.inp

This is the file for a modal analysis of the whole stator with the spring plates physically (not as spring elements) applied.
The post processing has to be done in the GUI.

/ANSYS/Simplified_Model/START_TRANSIENT_SPRING_PLATE.inp

This is the file for a transient analysis of the whole stator with the spring plates physically applied. By (un-)commenting the ACEL command in line 37, gravity force can be (dis-)regarded. The post processing file (transient_postproc_spring_plate.inp) contains two evaluation methods: one, where the global reaction force of each soleplate is evaluated, and a second one, where every single node (which is fixed to the concrete) of each soleplate is evaluated. The desired evaluation method can be chosen by placing it before / after the /eof command.

The results are written into a .csv file, saved in the working directory. This output file contains the following values, ordered by their column:

1. Node number of fixed node in ANSYS (can be Zero, depending on the evaluation method)
2. Relative (tangential*) location of the node, related to the soleplate center (can be Zero, depending on the evaluation method)
3. Tangential location of the spring plate
4. Tangential* reaction force amplitude
5. Time
6. Applied force on the inner core radius
7. Axial reaction force

*) As for the evaluation of the spring plate a cartesian coordinate system is used, the term "tangential" is not correct. It is just used to depict the location / direction, based on the cylindrical coordinate system in the center of the stator.

/ANSYS/Simplified_Model/START_VERY_SIMPLE_MODAL.inp

This file was used to verify the results of the TTM in this thesis. It performs a modal analysis with a stator core, modeled by 1-D rotary masses and torque spring elements.

/ANSYS/Simplified_Model/special_calculations/

This folder contains some calculations which are not directly related to the simplified model and the thesis. Most of them deal with ANSYS specific experiments (i.e. how to handle COMBIN40 elements, etc.).

/ANSYS/Full_Model/

This folder includes the calculation files for the solid "Mica" model. The UG model of "Mica", used for this calculation, is in the directory /Project_Data/Mica/models/ and was exported as Parasolid to the subfolder parasolids of this directory. The file START_static.inp is a static calculation and was primarily created to verify the correctness of the applied BC in the symmetry planes. START_MODAL_simple.inp and START_FREQURESP.inp are for performing a modal / frequency response analysis. START_transient.inp performs the transient analysis.

/ANSYS/Quarter_Model/

The calculation files in this folder are to verify the symmetry boundary conditions, applied to the solid UG model in the directory /ANSYS/Full_Model/, with the help of the simplified model, where results of a 360° model are already known.

/ANSYS/Soleplate_Springs_FE/

The files for all static spring calculations can be found in this folder.
The file torque_wave_key_original.inp is to calculate stress and displacements for the torque wave key. This file contains exchangeable paragraphs. Depending on which calculation is required, the appropriate paragraph (behind the /eof command) must be copied before the /solution command. Which paragraph applies which BC on which design is described by comments in the file itself. The post processing has to be done in the GUI.
The file slot_key.inp generates the half model of the slot key spring. Whether force or displacement is applied can be decided by (un-)commenting appropriate lines between line 62 and line 72. The post processing has to be done in the GUI.
spring_plates.inp does the static calculation of the spring plates. To regard forces normal to the plate, the appropriate paragraph after the /eof command has to be copied to the marked position in the file (line 99). The post processing has to be done in the GUI. The parameter stiffness is calculated during the run. It includes the plate's stiffness.